University of Southampton
Faculty of Physical Sciences and Engineering
Optoelectronics Research Centre

Novel Systems via Nonlinear Frequency Conversion of Fibre-Amplified Ultrafast Semiconductor Lasers

by

Ho Yin Chan

Thesis submitted in partial fulfilment of the requirements for
the degree of Doctor of Philosophy

May 2016

UNIVERSITY OF SOUTHAMPTON

ABSTRACT

FACULTY OF PHYSICAL SCIENCES AND ENGINEERING

Optoelectronics

Doctor of Philosophy

NOVEL SYSTEMS VIA NONLINEAR FREQUENCY CONVERSION OF FIBRE-AMPLIFIED ULTRAFAST SEMICONDUCTOR LASERS

by Ho Yin Chan

This thesis presents the development of novel, high-power and high-energy ultrashort-pulse sources by exploiting nonlinear frequency conversion of Yb^{3+}-doped-fibre (YDF)-amplified compact semiconductor lasers. Being highly efficient, compact and flexible, such topology offers tremendous opportunities across various industries and scientific communities such as electronics, photonics, manufacturing, healthcare, defence and fundamental physics. Here, tunable near- and mid-infrared (NIR and MIR) as well as supercontinuum sources with record-breaking and novel attributes are demonstrated.

Microjoule picosecond MIR pulse sources running at MHz repetition rates, particularly ones that are compact and economical, are highly sought after for resonant-infrared pulsed-laser deposition and ablation (RIR-PLD and RIR-PLA) in commercial facilities. A compact, stable, gain-switched-diode (GSD)-seeded picosecond master-oscillator power amplifier (MOPA), employing simple direct amplification via conventional YDFs in a nearly all-fiberised configuration, was developed to generate 18-μJ pulse energies and an average power up to 100 W at MHz repetition rates, with narrow spectral linewidth in a diffraction-limited and single-polarisation output beam. This flexible 1-μm source demonstrated the highest reported pulse energies from a GSD-seeded picosecond MOPA and enabled successful generation of microjoule MIR (and multi-microjoule NIR) picosecond pulses at 1 MHz via various periodically-poled-MgO:LiNbO3-based optical parametric devices in the regime of 2.5-4 μm, covering such vibrational resonances as the CH-stretch and OH-stretch. Moreover, the presented optical parametric oscillators (OPOs) showed the highest reported MIR and NIR pulse energies from a picosecond OPO.

GHz repetition rates are desirable for metrological applications of frequency combs. The first reported use of a fibre-amplified, mode-locked vertical-external-cavity surface-emitting laser as a pump source for supercontinuum generation is presented. The system consisted of a 1040-nm femtosecond MOPA generating average power up to 40 W at 3-GHz repetition frequency, a high-throughput transmission-grating compressor and a photonic crystal fibre (PCF). Firstly, supercontinuum with a 10-dB spectral bandwidth of 200 nm and a flatness of better than ±1.5 dB over a span of 150 nm was generated via an all-normal-dispersion PCF. Secondly, a PCF with zero-dispersion wavelength at 1040 nm was used to generate spectral components covering 750-1300 nm but with much higher spectral intensity variations. Finally, an improved power amplifier was designed and built to boost the slope efficiency by more than two-fold to 90%. Potential applications include power-scaling femtosecond oscillators to average power of > 100 W, as well as high-power self-referencing frequency-comb generation.

To my parents

and to the loving memory of my grandparents

Table of Contents

List of figures

List of tables

Declaration of Authorship

I, Ho Yin Chan, declare that this thesis entitled “Novel Systems via Nonlinear Frequency Conversion of Fibre-Amplified Ultrafast Semiconductor Lasers” and the work presented in it are my own and have been generated by me as the result of my own original research. I confirm that:

- this work was done wholly or mainly while in candidature for a research degree at this University;
- where any part of this thesis has previously been submitted for a degree or any other qualification at this University or any other institution, this has been clearly stated;
- where I have consulted the published work of others, this is always clearly attributed;
- where I have quoted from the work of others, the source is always given. With the exception of such quotations, this thesis is entirely my own work;
- I have acknowledged all main sources of help;
- where the thesis is based on work done by myself jointly with others, I have made clear exactly what was done by others and what I have contributed myself;
- Parts of this work have been published as:
  (Please refer to Appendices A.1, A.2 and A.3 on Page 139-140)

Signed: ....

Date:...

Acknowledgements

First of all, I would like to take this opportunity to express my sincere gratitude to my supervisor Professor David Shepherd for guiding me through this invaluable experience of PhD studies. I am very grateful to him for not only the insightful discussions on parametric nonlinearities, but also for his profound advice and highly efficient supervision on my research, as well as his patience, supports and encouragement in every aspect of this journey, especially at times of difficulties. Not to mention that his exceptionally fast proof-reading of my written work is appreciated. I am greatly thankful to have had the opportunity to work with him.

This great thankfulness has to be extended to my co-supervisor Dr. Shaif-ul Alam for the helpful discussions on technologies related to fibre amplifiers, in addition to his stimulating advice, affirmation of my analysis and solutions to problems, as well as encouragement throughout the course of my studies.

I would also like to express my sincere gratitude to my co-supervisor Professor David Richardson for his inspiration, and constructive feedback on my work. His encouraging comments have certainly given me extra energy to move forward. I am very grateful that I have had the opportunity to work with him.

Great thanks must also go to the following colleagues at the Optoelectronics Research Centre (ORC):

- Dr. Jonathan Price, for his guidance and the insightful discussions on the femtosecond work. It was a great pleasure to have co-worked with him in part of my studies.
- Dr. Morten Ibsen, Dr. Radan Slavik and Dr. Phillip Gorman, for their insightful advice, technical support and generosity in sharing their expertise.
- Dr. Jaclyn Chan, for the helpful discussions and sharing that we have had from time to time, as well as her technical and spiritual supports and prayers.

I would also like to acknowledge the following people:

- The colleagues with whom I have collaborated in the experiments presented in this thesis. They are Dr. Robin Head and Dr. Keith Wilcox from the School of Physics and Astronomy, and Dr. James Feehan, Dr. Lin Xu and Dr. James Bateman from the ORC.
- All the past and present colleagues in various research groups at the ORC, with whom I have had interesting discussions, or from whom I have borrowed equipment, components or tools occasionally during the course. They include Professor Periklis Petropoulos, Dr. Martin Berendt, Dr. Alex Heidt, Dr. Yongmin Jung, Dr. Francesca Parmigiani, Dr. Victor Fernandez Rancano, Dr. Zhixin Liu, Dr. Matthias Feinäugle, Dr. James Grant-Jacob, Dr. Jae Daniel, Dr. Zhihong Li, Dr. Richard Lewis, Dr. Tim Lee…
- The past and present members in the technical support teams. They include Mr. David Oliver, Mr. Simon Harris, Mr. Nick Gilbert, Mr. David Turner, Mr. Trevor Austin, Mr. Simon Butler, Mr. Jamie Cook and Mr. Chris Nash…

Special thanks must go to Professor Periklis Petropoulos who was the first person I met at the ORC. Without him, I would not have started my PhD journey here. I would also like to acknowledge the ORC for their financial support of my PhD studies.

I must also thank Miss Wong for her help and support during my time in Southampton, and acknowledge my brother for supporting our parents when I am away from home. Finally, I am forever indebted to my parents and late grandparents for their endless love and pride in me, without which I would never have come this far.

Praise be to God.

Chapter 1

Introduction

British Secret Intelligence Service agent James Bond was captured and strapped on a metal table underneath a high-power laser beam that inched its way towards his body as it was cutting through the metal… This is one of the scenes in the movie *Goldfinger* in 1964. Although such high-power lasers actually did not exist at the time the movie was produced, the scene was arguably the first time when the potential powerfulness of lasers was visually shown to the general public. Four years before that, engineer and physicist Maiman demonstrated the first laser using a ruby crystal and generating red light at 694 nm [1].

Over the past 50 years since its invention, the laser has grown to the current status where numerous types of lasers are playing key roles in a host of industries. Applications can be found in almost every aspect of our daily lives, ranging from DVD players, fibre broadband for internet connection, bar-code scanners and speeding detectors, to medical surgery, biomedical diagnostics, chemical sensing and material processing. Due to its versatility, laser technology has become one of the forerunners in both industrial development and scientific research. This chapter serves to provide the readers with an overview of the author's work in one aspect of this ever-growing field of research by laying out the motivations of the project, highlighting the key achievements from the work and outlining the flow of the thesis.

A set of novel, high-power and high-energy ultrashort-pulse sources were developed and will be presented in this thesis. They are picosecond systems generating tunable near- and mid-infrared (NIR and MIR) wavelengths and a femtosecond system for NIR supercontinuum generation. Although they had different configurations and thus components and characteristics, these sources shared a common high-level system architecture, which was formed by a master-oscillator power amplifier (MOPA) consisting of a compact semiconductor seed laser and a Yb^{3+}-doped-fibre (YDF)-amplifier cascade, followed by a nonlinear frequency converter. Figure 1-1 illustrates the block diagram of such an approach. Details of these systems will be unfolded as the thesis progresses.

Figure 1-1 Block diagram of the ultrashort-pulse systems to be presented in this thesis

1.1 Motivation

1.1.1 *Table-Top Pulsed Laser Sources for Mid-Infrared Material Processing*

The MIR regime (~2.5-20 µm) of the electromagnetic spectrum has drawn huge attention from a wide span of disciplines largely due to its overlap with the vibrational transitions of various functional groups in many organic and inorganic molecules. Moreover, there are two atmospheric transmission windows (3-5 µm and 8-13 µm) within the MIR regime, which allow the realisation of important free-space applications, such as remote sensing. These features have led to the development of MIR technological applications in spectroscopy [2,3], environmental monitoring [4,5], materials processing [6–8], atomic physics [9], surgery[10], and military countermeasures [11] to name but a few. The suitability of a laser source for a particular application depends on parameters such as wavelength, bandwidth, average power and peak power. In the cases where pulsed operation is required, further optimisation could be achieved through investigation of the parameter space including pulse duration, pulse energy and repetition rate.

Of particular interest in this work, pulsed MIR technology has become a key player in organic-material processing via techniques such as resonant infrared pulsed-laser deposition (RIR-PLD) and ablation (RIR-PLA) [7,12,13], where excitation of vibrational resonances can break the relatively weak intermolecular bonds and lead to ablation and deposition of high-quality polymer films with unmodified chemical structure. Figure 1-2 shows some examples of vibrational modes in organic and polymeric materials. Recent work has also provided a relatively new paradigm for PLD based on microjoule, picosecond pulses at MHz repetition rates [14] rather than nanosecond pulses at a few tens of Hz. This has enhanced both the reaction rates and throughput. In addition, broadly tunable sources are desired as they can process a larger range of materials.

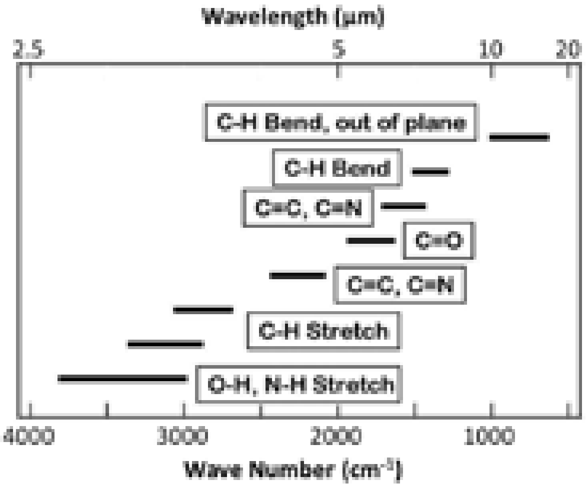

Figure 1-2 Examples of vibrational modes in organic and polymeric materials [14]

However, there is a dearth of such kinds of laser sources in the current technology. For instance, wavelengths around 2 to 5 μm can be generated separately from lasers such as Cr^{2+}:ZnSe, Er:YAG, HBr and Fe^{2+}:ZnSe but pulse energies of $\gtrsim 1$ μJ were typically achieved by operating these lasers in the nanosecond regime and/or at repetition rates of Hz or kHz [12,15–17]. Moreover their tuning ranges were typically $\lesssim 1$ μm [18–20]. As a consequence, the majority of RIR-PLD experiments to date have been performed by free-electron lasers (FELs) [7,8,14,21–25] which are ideal for demonstration but not suitable for a commercial processing facility due to their room-size occupancy of space and enormous cost.

In contrast, these problems can be circumvented by employing optical parametric down-conversion of readily available NIR picosecond lasers. Such techniques will be discussed in Chapter 2, Chapter 4 and Chapter 5 of this thesis. High energies or powers can be realised in a pump source by employing a MOPA configuration, which will be discussed in Chapter 2 and Chapter 3 in this thesis. High-power or high-energy picosecond MIR pulses at MHz repetition rates generated with this approach have been previously demonstrated in various systems [13,26–29] but unfortunately each comes with its own drawbacks. More details will be described in Chapter 3, Chapter 4 and Chapter 5 accordingly. For example, their pulse energies were not high enough for RIR-PLD/ RIR-PLA, their pump sources were built with free-space optics and thus alignment between stages throughout the whole system was required for daily operation, their MOPAs employed additional components such as polarisation controllers and chirped fibre Bragg gratings which could be eliminated, or their optical parametric configurations required components such as acousto-optic modulator and array of mirrors to realise operation at MHz repetition rates. All of these introduced complexities to the implementation, minimisation or operation of the systems.

The work presented in this thesis was motivated to develop a novel, compact and efficient source of high-energy picosecond pulses with broad tunability in the MIR regime to fulfil the requirements of a commercial processing facility for deposition of high-quality and chemically unmodified polymer thin films of high technological importance via the technique of RIR-PLD. Here, the combination of a gain-switched-diode (GSD) laser with an YDF-amplifier cascade was exploited to form a stable, compact and robust MOPA in a nearly-all-fiberised configuration with a minimum of free-space optics to enhance the practicality of the system. High pulse energies at MHz repetition rates, along with narrow spectral linewidth and diffraction-limited beam quality, were targeted so that the MOPA could be employed to efficiently pump optical parametric devices to generate broadly tunable MIR wavelengths with microjoule pulse energies for RIR-PLD/ RIR-PLA processes. In particular, the spectral region of 2.5-4 μm covering the vibrational resonance of a wide range of important functional groups including the OH-stretch and the CH-stretch was investigated. Furthermore, tunable repetition rate and capability of power-scaling to high average power (~100 W) would increase the flexibility of the system to allow a wider span of potential applications as well as a more comprehensive investigation on the parameter space for optimising the RIR-PLD/ RIR-PLA processes. Therefore these attributes were also taken into consideration when designing the MOPA. Optical parametric devices of different configurations with different pros and cons were then implemented based on periodically-poled-MgO:LiNbO3 (PPLN) crystals. The performances and output characteristics of these systems as well as their potential for RIR-PLD/ RIR-PLA were compared, although time limitations meant that no actual ablation experiments were conducted.

While this flexible high-energy and high-power table-top system is of interest for the growing of polymer thin films, the MOPA by itself and the system as a whole should also be attractive to diverse sectors for a variety of applications. These include but not limited to environmental monitoring, high-throughput material processing, and nonlinear frequency conversion to generate high-energy or high-power pulses in other spectral regions.

1.1.2 Supercontinuum Generation with Fibre-Amplified Vertical-External-Cavity Surface-Emitting Lasers

Supercontinuum sources find a wide range of applications including spectroscopy [30], semiconductor characterisation [31], microscopy [32], optical coherence tomography [33], communications [34], metrology [35] and astronomical spectrometer calibration [36]. Generation of supercontinua can be carried out in bulk materials by pumping with high-intensity pulses such as the first reported supercontinuum generation in bulk borosilicate glass with 5-mJ picosecond pulses [37]. However, to increase the nonlinear interaction and thus the spectral broadening of the pulses, a high-intensity beam maintained over a long nonlinear interaction length is favourable. Unfortunately, this is difficult to achieve in bulk glass due to diffraction of laser beams. Optical fibres provide a solution by offering strong optical confinement in a waveguide structure together with low propagation losses that allow a long nonlinear interaction length. Supercontinua generated in optical fibres can thus combine the brightness and focusing properties of a laser with a bandwidth comparable to, or even broader than, that of a white-light incandescent bulb. In addition to the advantages found in conventional fibres, specialty fibres called photonic crystal fibres (PCFs) can provide additional degrees of freedom. By modifying the hole and pitch sizes of the microstructured fibre, specific nonlinear and dispersive characteristics can be obtained. These engineerable properties, such as high nonlinearity and shifted zero-dispersion wavelength (ZDW), make PCFs particularly interesting and useful for supercontinuum generation.

GHz repetition rates are desirable for metrological applications of frequency combs since the increased mode spacing results in higher power per mode as well as easier isolation of the individual modes. Furthermore, generation of coherent supercontinua typically requires sub-100-fs pulses when pumping near the ZDW of a PCF [38]. In contrast, it has been shown that supercontinuum with high coherence can also be generated with pulses of several hundred femtoseconds duration through all-normal-dispersion (ANDi) PCFs [39,40].

Mode-locked fibre lasers and waveguide oscillators can generate pulses running at over 10-GHz repetition rate [41,42] but typically with pulse duration of $\gtrsim$ 1 ps. A passively mode-locked Ti:Sapphire laser has been demonstrated with a 10-GHz repetition rate and pulse duration as short as 42 fs, but specially designed mechanics and optics were required [43]. Moreover, Ti:Sapphire lasers are usually pumped by bulky and inefficient Argon-ion lasers or by frequency-doubled solid-state lasers, which add complexity to the systems. Recently there have been considerable interests in developing directly diode-pumped mode-locked Ti:Sapphire lasers. Such systems have been demonstrated with sub-100fs pulse durations but the repetition rate remains at ~100 MHz [44,45].

On the other hand, mode-locked (ML) vertical-external-cavity surface-emitting lasers (VECSELs) typically work in the GHz pulse-repetition-rate regime [46], with demonstrated tunability of the repetition frequency over several GHz [47,48], pulse duration as short as 60 fs [49], and average output power up to 5.1 W [50]. However, the average output power in [49] was only 35 mW and the pulse duration in [50] was 682 fs; high-average power and sub-100-fs pulses have not yet been achieved in the same device. There is thus an interest in power scaling ML-VECSELs to produce a flexible source for coherent GHz supercontinuum generation. An attractive approach to perform power scaling is through fibre-MOPAs, as will be explained in Chapter 2. In previous work, a fibre-MOPA system seeded by a 1-GHz, 500-fs, ML-VECSEL has demonstrated 53-W average output power [51]. However, only 1% of this power could be used for pulse compression, due to the power-handling capability of the aluminium reflection grating compressor used in that experiment.

In this work, femtosecond pulses from a multi-GHz ML-VECSEL were amplified through a chain of YDF-amplifiers, compressed by a high-throughput dielectric transmission grating, and then launched into PCFs to generate supercontinua. Two PCFs with different dispersion characteristics were exploited in turn, and the generated spectra were compared.

1.2 Key Achievements

The following table highlights the main results achieved from the various systems and experiments presented in this thesis. Also shown in the table are the corresponding chapters where these systems are discussed.

Table 1-1 Key achievements from the work presented in this thesis

GSD-seeded YDF-MOPA	*Chapter 3*
· The highest pulse energies from a GSD-seeded picosecond MOPA	
Harmonic-cavity PPLN-based OPO pumped by GSD-seeded YDF-MOPA	*Chapter 4*
· The highest MIR pulse energies from a picosecond OPO	
Fibre-feedback PPLN-based OPO pumped by GSD-seeded YDF-MOPA	*Chapter 5*
· The highest NIR pulse energies from a picosecond OPO · The highest MIR pulse energies from a picosecond OPO with both signal and idler output	
PCFs pumped by fibre-amplified ML-VECSEL	*Chapter 6*
· The first reported use of a fibre-amplified ML-VECSEL as a pump source for supercontinuum generation	

1.3 Thesis Layout

A review on the background technology of compact solid-state lasers, fibre amplifiers, optical parametric devices and PCFs is provided in Chapter 2, focusing on the physics, mathematical models and state-of-the-art technologies that are directly relevant to the understanding of the chapters that follow.

Chapter 3 will discuss the design and performance of a compact, stable, robust and flexible GSD-seeded YDF-MOPA system. It was capable of delivering high-power (100-W average powers) and high-energy (approaching 18 μJ) picosecond pulses with tunable repetition rates and pulse durations, opening a door to various applications. In particular, the pulse parameters could be adjusted to make the MOPA a well-suited pump source for optical parametric devices, through which high-energy MIR pulses at MHz repetition rates for RIR-PLD/ RIR-PLA applications could be realised. Four such devices with different configurations were subsequently demonstrated and will be described in Chapter 4 and Chapter 5. Moreover, limitation on MOPA power-scaling due to fibre nonlinearity will be discussed.

In Chapter 4, MIR picosecond pulses with microjoule-energies that are required for efficient RIR-PLD/ RIRPLA were demonstrated via three different PPLN-based optical parametric devices. These devices had relatively simple configurations— an OPG, an OPA and a free-space-cavity OPO. The pros and cons of each of these devices will be discussed along with their suitability for RIR-PLD/ RIR-PLA applications in terms of parameters such as spectral bandwidth, beam quality and tunability. Damage to the nonlinear crystal in the OPA configuration was observed during the experiment and a solution was shown to overcome that problem.

As will be seen in Chapter 4, a major drawback of the free-space harmonic-cavity OPO is lack of an output at the NIR wavelengths, thus limiting its range of applications. Chapter 5 will explore a solution to this problem by exploiting a more sophisticated, yet still compact, configuration with a fibre-feedback resonating cavity to construct an OPO that was capable of providing high-energy NIR pulses at the multi-microjoule level as well as the microjoule-energies MIR pulses that are suitable for RIRPLD/ RIRPLA. Furthermore, an interesting phenomenon of intracavity supercontinuum generation was observed during the experiment. Approaches to controlling the spectral broadening will be presented.

In Chapter 6, a femtosecond YDF-MOPA seeded by a ML-VECSEL at GHz repetition rate was constructed as a pump source for supercontinuum generation. Two PCFs with different guiding properties were used in turn to demonstrate supercontinua with different spectral properties. One is an ANDi PCF and the other has a ZDW at 1040 nm. In addition, the power amplifier of the MOPA was re-designed to boost the signal power, leading to a significant improvement in the slope efficiency as well as a higher polarisation-extinction ratio, for use in future experiments.

The thesis is drawn to a close in Chapter 7 with a revisit to the major results obtained from the various experiments presented in the earlier chapters, along with some remarks on possible future work.

Chapter 2

Background Technology

As seen in Chapter 1, there are two main building blocks for the work presented in this thesis— a master-oscillator power amplifier (MOPA) and a nonlinear frequency converter. An overview of their background theories and technological aspects that are essential to the understanding of the later chapters will be introduced here in two parts: Part A will focus on Yb^{3+}-doped-fibre (YDF) MOPA systems seeded with compact solid-state lasers while Part B will discuss the relevant optical parametric devices and photonic crystal fibres (PCFs).

Part A. Master-Oscillator Power Amplifiers (MOPA)

A MOPA system consists of a low-power seed and an optical amplifier (cascade). It allows a generic high-power amplifier to be combined with a variety of pulse sources. Furthermore, the pulse properties can be controlled precisely at the seed and then projected to the output at high power through the amplifiers. In particular, as will be presented in the following sections, fibre amplifiers are simple, robust, compact, highly efficient and able to provide high beam quality when designed correctly.

Section 2.1 will introduce the operating principles of two compact seed lasers. The first is a self-seeded gain-switched laser diode (GSLD) that was built to serve as an oscillator for the picosecond MOPA in the work discussed in Chapter 3, Chapter 4 and Chapter 5. The second is a mode-locked vertical-external-cavity surface-emitting laser (ML-VECSEL) that was employed to seed the femtosecond MOPA in the work presented in Chapter 6 . The amplifiers in both of these MOPAs were constructed with YDFs due to their superior properties for high-power operation. Section 2.2 will overview various aspects of fibre amplifiers, starting from the basics of fibre optics and then move on to a brief development history of fibre lasers and amplifiers, followed by a discussion on the main properties and advantages of YDFs. The essential details of amplification, pulse propagation and nonlinearities in fibres that are relevant to the work will be introduced before the section is concluded with a brief discussion of some of the challenges of high-power operation and some common amplification schemes.

2.1 Compact Solid-State Seed Lasers

2.1.1 Gain-Switched Laser Diodes

Picosecond pulses generated by gain-switching a laser diode were first introduced by Ito et al. [52] and were primarily developed for telecommunications [53,54] at limited power levels. Recently, they have also been used as seed lasers for high-power MOPA system at 1550nm [55] and 1060nm [56,57]. The advantages of GSLDs come from their robust configurations and widely tunable repetition rates without modifying the laser cavity. In contrast to a mode-locked laser in which tuning of repetition frequency involves adjustment of resonator length and alignment of cavity, such tuning in a GSLD is alignment-free and is controlled electronically.

A GSLD is operated by modulating the laser gain of the diode with a radio-frequency (RF) driving signal biased below the threshold. Electrical current injected into the diode causes the carrier density to increase. When it reaches a level at which the optical gain exceeds the cavity losses, lasing occurs and a series of relaxation oscillations is initiated. The falling edge of the RF pulse reduces the carrier density below the threshold level before the second oscillation is initiated. The generated optical pulse from a GSLD is much shorter than the electrical pulse. Previous work [58] has shown that seeding can improve the pulse quality by decreasing the timing and amplitude jitters in addition to reducing the time-bandwidth product, which would otherwise be many times the transform-limit due to the intrinsic negative chirp in the unseeded gain-switched pulse.

Furthermore, the same experiment has shown that there was no loss of performance in both the temporal and spectral domain when using self-seeding rather than external seeding. Therefore, the oscillator built for the picosecond MOPA presented in this thesis had employed a self-seeding configuration in view of its simpler implementation and lower cost compared to the external-seeding scheme.

Figure 2-1 depicts the set-up of the oscillator. A 1030-nm Fabry-Perot semiconductor laser diode temperature-stabilised with a thermoelectric cooler was self-seeded by feedback from a uniform fibre Bragg grating (FBG). The laser diode output and the FBG were both polarisation-maintaining (PM). The picosecond pulses at MHz repetition rate seeding the MOPA system presented in Chapter 3 through Chapter 5 were generated using an FBG with reflectivity of 12.5% and a centre wavelength of 1034.5 nm. The laser diode was DC-biased below the lasing threshold via a Bias-T and gain-switched by a train of RF pulses.

As an alternative mode of operation, mode-locked optical pulses can be generated when the driving frequency matches a harmonic of the synchronization frequency in the cavity formed by the diode and the FBG [59]. Detuning from this frequency results in broader output pulses as the oscillator shifts back towards the gain-switching regime. Picosecond pulses generated under these two different modes of operation were demonstrated and will be presented in Chapter 3.

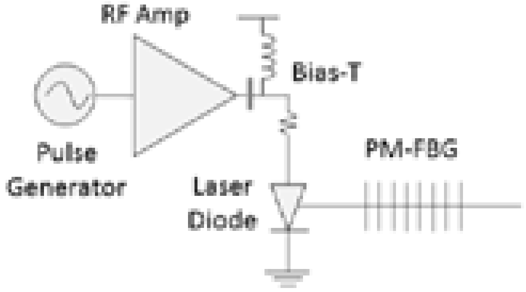

Figure 2-1 Configuration of the self-seeded GSLD for generating picosecond pulses

2.1.2 Mode-Locked Vertical-External-Cavity Surface-Emitting Lasers

ML-VECSELs typically work at multi-GHz pulse repetition rates in the sub-picosecond regime [46], with demonstrated tunability of the repetition frequency over several GHz [47,48] by adjusting the cavity length. Near-transform-limited pulses as short as 60 fs have been reported [49].

The oscillator of the femtosecond MOPA discussed in Chapter 6 was developed by the VECSEL Group in the School of Physics and Astronomy at the University of Southampton. The set-up is schematically shown in Figure 2-2. The cavity comprises a gain chip made of InGaAs quantum wells with broad gain bandwidth to support generation of ultrashort pulses [60], a semiconductor saturable-absorber mirror (SESAM) and a spherical output coupler with transmissivity of 0.3%. The AlAs/GaAs distributed Bragg reflectors (DBRs) in the gain structure and the SESAM were designed for operation at 1040 nm. Details of their design are described in [61]. The gain-structure and the SESAM were mounted on water-cooled temperature-controlled copper blocks to reduce thermal drift. Near-transform-limited pulses with a duration of 405 fs and a 3-GHz repetition rate were generated.

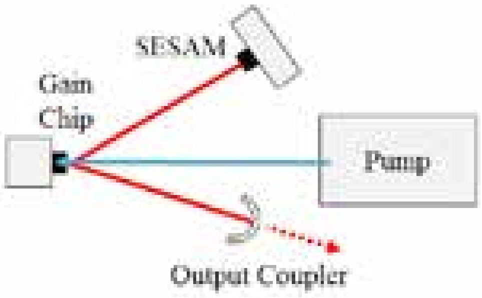

Figure 2-2 Configuration of the ML-VECSEL for generating femtosecond pulses, showing the pump (blue) and signal (red) beams in the set-up. SESAM = Semiconductor Saturable Absorber Mirror.

2.2 Fibre Amplifiers

2.2.1 Fibre Optics Basics

A conventional optical fibre contains a core surrounded by a cladding with a lower refractive index. The light is guided in the core by total internal reflection and the acceptance angle θ of the core is related to the numerical aperture NA defined by:

$$NA = \sin(\theta) = \sqrt{n_{core}^2 - n_{clad}^2} \qquad (2.1)$$

where n_{core} and n_{clad} are the refractive indices of the core and the cladding, respectively. Single-mode guidance for a step-index fibre is ensured when the V number given by equation (2.2) is less than 2.405 [62]:

$$V = \frac{2\pi}{\lambda} a\, NA \qquad (2.2)$$

where a is the core radius, λ is the operating wavelength and NA is the numerical aperture given by equation (2.1). Single-mode operation of a fibre gives good output beam quality, which is useful for many applications.

The beam quality can be quantified by the M^2 factor, which is defined according to the ISO Standard 11146 [63] as the ratio between the beam parameter product of the beam under test and that of a diffraction-limited Gaussian beam with the same wavelength λ:

$$M^2 = \frac{w_0\, \theta}{\lambda/\pi} \qquad (2.3)$$

where w_0 is the beam waist radius and Θ is the far-field half-angle beam divergence. The minimum value of M^2 is 1, corresponding to a diffraction-limited beam.

In addition to beam quality, fibres provide a lot of advantages compared to their bulk counterparts. Firstly, a relatively small doped core (typically in the order of microns or tens of microns) implies a tight beam confinement and high beam intensity, thus lower pump power is required to achieve the necessary population inversion. Secondly, long length of fibres with large overlap between the signal and pump radiation in the doped core boosts the signal gain and the pump absorption; consequently high slope efficiency and high output power can be achieved. Thirdly, the high surface-to-volume ratio of fibres provides good thermal power handling by dissipating heat efficiently, which adds to the benefits of using fibres in high-power lasers and amplifiers. Finally, fibres are robust and can be spliced together with other fibre-coupled components, thus allowing realisation of compact systems and minimisation of alignment work that would otherwise be required for free-space optics.

2.2.2 Ytterbium-Doped Fibres

Attractive properties of rare-earth (RE) ions in glass hosts include their broad emission and absorption spectra, which allow a wide range of choices on pump and signal wavelengths, as well as generation and amplification of ultrashort pulses. RE-doped fibre lasers were first reported with Nd^{3+} dopants in the 1960's by E. Snitzer et al. [64,65] and Er^{3+}-doped fibre amplifiers revolutionised the telecommunications industry when they were first realized by D. N. Payne et al. in the 1980's [66]. More recently, YDFs have become the leading RE-doped fibres for high-power and high-pulse-energy amplifier systems, mainly due to their inherently low thermal loading and high gain per unit length, arising respectively from the low quantum defect and high permissible dopant concentrations. Lasers and MOPAs generating multi-kW average powers and GW peak powers have been achieved with YDFs [67,68] and most of the commercially available high-power fibre lasers are also ytterbium-based.

The electronic energy structure of Yb^{3+} ions in germano/ aluminosilicate glass, illustrated in Figure 2-3, is simple compared to other RE ions. For optical-wavelength transitions, only two manifolds are relevant— the excited-state manifold $^2F_{5/2}$ (with three Stark levels) and the ground-state manifold $^2F_{7/2}$ (with four Stark levels). This structure prohibits excited state absorption for both the pump and laser wavelengths, non-radiative decay via multi-phonon emissions, as well as concentration quenching via ion-ion transfer. High doping levels are therefore possible, leading to high gain in a short device length. In addition, the quantum defect is small in Yb^{3+} systems:

$$quantum\ defect = \frac{\nu_{pump} - \nu_{signal}}{\nu_{pump}} \tag{2.4}$$

where ν_{pump} and ν_{signal} are the frequency of the pump and signal, respectively. For example, the YDFs in the MOPA presented in Chapter 3 were pumped at 975 nm and lased at 1034.5 nm, giving a quantum defect of less than 6% of the pump photon energy. In contrast, the quantum defect would be ~24% in a Nd^{3+}:silicate glass, with a typical pump wavelength of 808 nm and a signal at 1062 nm. This translates to a very high optical-to-optical efficiency and a small thermal load for YDF systems.

Figure 2-3 Energy level structure of Yb^{3+} ions in germano/ aluminosilicate glass [69]

Figure 2-4 shows the absorption and emission cross-sections of Yb^{3+} ions in germano/ aluminosilicate glass. It can be seen that YDFs have very broad absorption and emission spectra, which allow choices on various combinations of pump and signal wavelengths. In particular, the strong absorption bands around 915 nm and 975 nm imply that YDFs can be pumped with readily available high-power laser diodes operating at those wavelengths, thereby enhancing the practicality of YDF systems. Furthermore, compared to other RE ions such as Nd^{3+}, Yb^{3+}-doped gain medium have wider gain bandwidths and are thus more favourable for ultrashort-pulse generation and amplification. For example, an YDF amplifier with gain bandwidth of ~100 nm can theoretically support pulses with duration $\lesssim$ 20 fs [70].

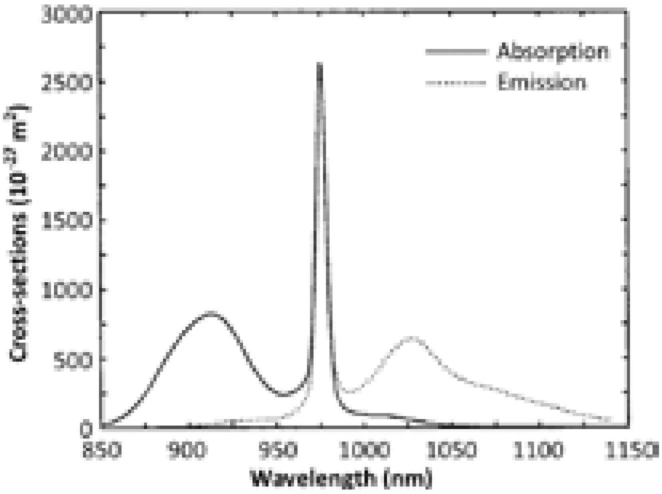

Figure 2-4 Absorption (solid) and emission (dotted) cross-sections of Yb^{3+} ions in germano/ aluminosilicate glass [69]

2.2.3 Amplification and Propagation

Amplification in a gain medium depends on the interplay between the pump power, signal power and population inversion. When neglecting amplified spontaneous emission (ASE) and assuming homogeneous broadening, the evolution of signal and pump power can be described by the following coupled rate equations [69] in the case of continuous-wave (CW) propagation:

$$\frac{\partial P_p}{\partial z} = \Gamma_p \left(\sigma_{21p} N_2 - \sigma_{12p} N_1\right) P_p \tag{2.5}$$

$$\frac{\partial P_s}{\partial z} = \Gamma_s \left(\sigma_{21s} N_2 - \sigma_{12s} N_1\right) P_s \tag{2.6}$$

where P_p, Γ_p, σ_{12p}, and σ_{21p} are respectively the power, overlapping factor, absorption cross-sections, and emission cross-sections of the pump; P_s, Γ_s, σ_{12s}, σ_{21s} are the corresponding values of the signal. N_2 and N_1 are the steady-state upper- and lower- state population densities.

In addition to the attractive properties of YDFs discussed in section 2.2.1 and 2.2.2, the cladding pumping configuration invented by Kafka [71] has played an important role in the development of high-power lasers and amplifiers over the past two decades. In a typical double-clad fibre (DCF), the signal is guided along a RE-doped core that is surrounded by an inner cladding with lower refractive index. The pump waveguide is formed by the undoped inner cladding embedded in a lower-refractive-index outer cladding (typically made of polymer). The launched pump power is gradually absorbed within the core as the pump and signal propagate along the fibre. This configuration allows realization of high-power single-mode laser output with fibres pumped by multi-mode high-power laser diodes that could not be used efficiently for core pumping.

One of the most common ways to pump a DCF, especially in laboratory work, is free-space end-pumping, in which a pump beam is directly launched into the inner cladding of a DCF through coupling lenses. This approach has a relatively simple configuration and can offer good launching efficiency, although the pump end of the fibre is not accessible for splicing. Pumping technologies with more sophisticated configurations have been invented to free the fibre ends while allowing high-power pump sources to be combined and fibre-coupled to the signal. An example of such configurations is the SPI Lasers’ proprietary GT-wave technology [72], in which multi-port injected pump power is coupled to the signal in a distributed manner by placing the multi-mode pump fibres in contact with the single-mode signal fibre, bundled together within a common low-index coating. YDF CW lasers with kW output power have been manufactured based on this technology. Another advanced pumping architecture is tandem pumping [73], which has enabled IPG Photonics’ 10-kW single-mode YDF CW lasers. This approach utilises one or several fibre lasers to pump another one, thereby allowing in-band and high-brightness pumping. This offers the advantages of reduction in thermal loading as well as a shorter device length.

In the MOPAs presented in this thesis, the free-space end-pumping configuration was employed for the final high-power pumping stage, considering the high peak power of the pulses and the availability of components. On the other hand, splicing via wavelength-division multiplexers was used for lower-power pumping by fibre-coupled diodes.

For pulse propagation in fibre amplifiers, the main dynamics can be described in a simplified model by the nonlinear Schrödinger equation (NLSE), including gain but neglecting higher-order dispersion terms and higher-order nonlinearities such as intrapulse Raman scattering [62]:

$$j\,\frac{\partial A}{\partial z} = \frac{\beta_2}{2}\frac{\partial^2 A}{\partial T^2} - \gamma|A|^2 A + j\frac{g}{2}A \tag{2.7}$$

where A is the normalised slowly varying amplitude of the pulse, β_2 is the group-velocity dispersion (GVD) with positive values for normal dispersion and negative values for anomalous dispersion, γ is the nonlinearity coefficient and g is the gain coefficient. The nonlinearity coefficient is defined as:

$$\gamma = \frac{k_0 n_2}{A_{eff}} \tag{2.8}$$

with k_0 being the free-space propagation constant, n_2 the nonlinear refractive index coefficient (typical value of ~$2.6\text{x}10^{-20}\text{m}^2\text{W}^{-1}$ for silica fibre) and A_{eff} the effective mode-field area. For a pulse with duration of T_0 and peak power of P_0, the dispersion length L_D and nonlinear length L_{NL} defined below provide respectively the length scales over which dispersive and nonlinear effects become important during pulse propagation:

$$L_D = \frac{{T_0}^2}{|\beta_2|} \tag{2.9}$$

$$L_{NL} = \frac{1}{\gamma P_0} \tag{2.10}$$

For example, when the fibre length is much less than L_{NL} but comparable to L_D, the pulse evolves in the dispersion-dominant regime. On the other hand, when the fibre length is much less than L_D but comparable to L_{NL}, the pulse propagation is mainly governed by the nonlinear effects. The interplay of dispersion and nonlinearity becomes significant when the fibre length is comparable to both L_D and L_{NL}.

2.2.4 Nonlinearities in Fibres

When an intense electromagnetic wave is applied to a dielectric, nonlinear optical effects arise. Polarisation of the dielectric induced by the electric field on the bound charges becomes nonlinear as they respond anharmonically. The induced polarisation can be written as:

$$\vec{P} = \varepsilon_0[\chi^{(1)}.\vec{E} + \chi^{(2)}:\vec{E}\vec{E} + \chi^{(3)} \vdots \vec{E}\vec{E}\vec{E} + \cdots] \tag{2.11}$$

where ε_0 is the vacuum permittivity, $\chi^{(j)}$ is the jth order susceptibility and is a tensor of (j+1)-rank, and $\vec{E}$ is the electric field. Due to the geometry of fibres, nonlinearity is of particular concern to high-power ultrashort-pulse fibre systems. A detailed discussion on this subject can be found in [62]; an overview of the nonlinear phenomena that are necessary for the understanding of the later chapters is given here. In particular, $\chi^{(2)}$ vanishes in media with symmetric molecular structure (neglecting surface effects); consequently, the lowest order nonlinearities in SiO_2-based optical fibres are the $\chi^{(3)}$ effects, which can be classified into two main groups: the Kerr effect and the inelastic scattering effect. Self-phase modulation (SPM) is an example of the first group while stimulated Raman scattering (SRS) is of the second.

The origin of SPM comes from the intensity-dependent refractive index, which can be expressed as:

$$n = n_0 + n_2 I \tag{2.12}$$

where n_0 is the linear refractive index, n_2 is the nonlinear refractive index coefficient related to $\chi^{(3)}$ [62], and I is the beam intensity. This induces a change of phase and thus instantaneous frequency, leading to chirping in the time domain and broadening in the frequency domain as the pulse propagates along a fibre. SPM increases the temporal pulse broadening rate in the normal-dispersion regime and reduces it in the anomalous-dispersion regime where the chirp induced by SPM can partially or completely cancel out that from the anomalous dispersion. In the case of a fundamental soliton, GVD and SPM balance each other in such a way that there would be no temporal or spectral broadening along the fibre. It should be noted that SPM is undesirable in laser sources that target bandwidth-limited applications, such as the picosecond MOPA presented in Chapter 3. On the other hand, it plays an important role in generating supercontinuum as will be seen in the experiments discussed in Chapter 6.

SRS stems from the oscillating polarisability given by the molecular vibration in a medium. The inelastic scattering process through optical phonons results in two possible emissions—a Stokes wave from a frequency down-shift and an anti-Stokes wave from a frequency up-shift. The Raman threshold is proportional to the effective mode-field area of the beam and inversely proportional to the effective length of the fibre, which is defined as $L_{eff} = (1-e^{-\alpha L})/\alpha$, where α is the pump attenuation per unit length. When the beam intensity is high enough, the Raman scattering process becomes highly efficient and the Stokes wave grows rapidly. For fused silica pumped at a wavelength of 1 μm, the Raman gain peaks at a frequency shift of ~13 THz as shown in Figure 2-5. These characteristic behaviours of SRS were also observed in the experiments discussed in Chapter 3, where the extractable signal pulse energies from the MOPA system were primarily limited by the rapid growth of the SRS. Moreover, thermal loading of a fibre increases with SRS intensities, thus bringing another nuisance to the amplifier system.

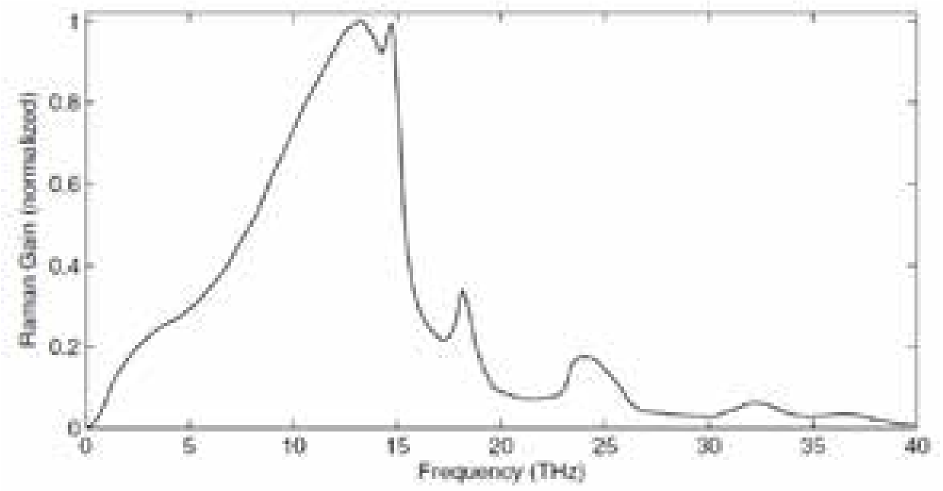

Figure 2-5 Normalised Raman Gain for fused silica pumped at 1 μm [62]

2.2.5 *High-Power Challenges and MOPA Configurations*

Nonlinear effects can be reduced in a fibre amplifier by increasing the fibre core diameter and thus the signal mode area. However, simply increasing the mode area would excite higher-order modes when for example V > 2.405 for a step-index-profile fibre. This leads to degradation of the output beam quality. To maintain single-mode guidance, large-mode-area (LMA) fibres with small NA are used. Furthermore, several techniques can be employed to ensure single-mode output from a multi-mode fibre. These include tailor-making the doping profiles to suppress the gain of higher order modes [74,75], bending the LMA fibres to introduce bending loss, which is significantly higher for higher-order modes compared to the fundamental mode [76], and using tapered sections [77] to assist the transition of the fundamental mode from single-mode fibres into LMA fibres.

When designing MOPA systems, one of the three common amplification schemes is usually employed— chirped-pulse amplification (CPA), parabolic-pulse amplification (PPA) and direct amplification.

The well-known CPA technique [78] avoids nonlinearity in the fibres by stretching femtosecond pulses with a stretcher, such as a single-mode fibre before amplifying the pulses. By conservation of energy, as the pulse is stretched, the peak power is decreased by the same factor. After amplification, the pulse is recompressed by a compressor, such as a pair of bulk gratings, and thus the peak power is boosted. The requirement of additional elements increases the complexity and cost of constructing a CPA system. However, very high peak power can be attained; millijoule pulse energies and gigawatt peak power have been achieved from femtosecond MOPAs using fibre CPA [79].

In contrast to CPA, where a stretcher is required to avoid nonlinearity, PPA utilises the interplay between SPM, normal dispersion and gain to generate parabolic pulses that propagate self-similarly [80]. This is an exact asymptotic solution to the NLSE given in equation (2.7). The resultant linear chirp can be efficiently compensated by a dispersive element such as a pair of bulk gratings. Femtosecond pulses with sub-microjoule pulse energies have been generated by this method from MOPAs with conventional YDFs [81]. However, if the pulse energy is more than a few μJ with pulses shorter than ~10ps, CPA might be needed to cope with the high nonlinearity.

Direct amplification was the approach used for the MOPAs that will be presented in this thesis. It has the simplest configuration among the three amplification schemes. In this approach, pulses from the oscillator are fed directly into the amplifier chain. Consequences resulting from nonlinearity and dispersion will exist but they are either tolerable for the applications of the system or if needed can be compensated by a compressor. In the work discussed in Chapter 3 and Chapter 6, the aforementioned nonlinearity and mode management were employed to optimize the power scaling capabilities of the MOPAs and to ensure a diffraction-limited output.

Part B. Nonlinear Frequency Converters

Two types of media were employed for the nonlinear frequency conversion presented in this thesis, lithium niobate ($LiNbO_3$, LN) crystals and glass optical fibres. Section 2.3 will overview the operating principles of the various optical parametric devices based on $LiNbO_3$ that were used to generate tunable near- and mid- infrared (NIR and MIR) pulses in the experiments discussed in Chapter 4 and Chapter 5. The optical parametric processes involved in these experiments were based on the $\chi^{(2)}$-nonlinearity, which will be introduced in the beginning of this section. Following that is a discussion on the quasi phase-matching technique for achieving an efficient nonlinear conversion. The development of parametric gain models will also be presented. After that, advantages and properties of the type of nonlinear crystal used in the work will be covered. The section is concluded with a brief comparison on the pros and cons of the different configurations for implementing optical parametric processes. The supercontinuum generation presented in Chapter 6 had involved the use of two different photonic crystal fibres (PCFs). The fundamentals of PCFs and supercontinuum generation will be introduced in Section 2.4. In-depth discussions on nonlinear optics in parametric sources and supercontinuum generation in PCFs can be found in [82] and [38], respectively.

2.3 Optical Parametric Sources

2.3.1 $\chi^{(2)}$ Nonlinearity Basics

Unlike in silica fibres, where it vanishes as mentioned in section 2.2.4, the $\chi^{(2)}$ susceptibility dominates the nonlinear processes in non-centrosymmetric crystals such as $LiNbO_3$. This gives rise to optical phenomena including second-harmonic generation, sum-frequency generation, difference-frequency generation and optical rectification. Energy is conserved and thus no heat is dissipated into the medium during these processes.

The parametric devices presented in this thesis were operated based on nonlinear processes known as optical parametric generation, amplification and oscillation, which are related to difference-frequency generation. In the first process, a pump incident on the $\chi^{(2)}$ crystal generates a signal photon and an idler photon, forming the basis of an optical parametric generator (OPG). If a signal (idler) photon is injected together with a pump photon, another signal (idler) photon will be generated along with an idler (signal) photon. This is the fundamental principle of an optical parametric amplifier (OPA). In the third process, the crystal is placed in an optical cavity to resonate the signal, idler or both. No input signal or idler is required. Such a device is called an optical parametric oscillator (OPO). In the case where both of the signal and idler are resonating, it is referred to as a doubly resonant OPO (DRO), otherwise it is a singly resonant OPO (SRO). By conservation of energy,

$$\omega_p = \omega_s + \omega_i \tag{2.13}$$

where ω_p, ω_s, and ω_i are the angular frequencies of the pump, signal and idler, respectively.

2.3.2 Quasi Phase-Matching

For efficient parametric conversion along the crystal such that an appreciable gain is acquired at the output, conservation of momentum is essential, leading to the phase-matching condition:

$$\Delta\vec{k} = \overrightarrow{k_p} - \overrightarrow{k_s} - \overrightarrow{k_\iota} = 0 \tag{2.14}$$

where $\overrightarrow{k_p}$, $\overrightarrow{k_s}$, $\overrightarrow{k_\iota}$, are the propagation vectors of the pump, signal and idler respectively, and $\Delta\vec{k}$ is the propagation-vector mismatch, which needs to be compensated for the interacting waves. Under normal circumstances, the different refractive indices at the different wavelengths mean that phase-matching is not achieved and the nonlinear wave does not grow in intensity. In order to achieve perfect phase-matching, one of the usual techniques is birefringent phase-matching (BPM), in which the birefringence of the nonlinear crystal is exploited to attain the necessary refractive indices for the ordinary and extraordinary polarisations. This is typically carried out by angle tuning which, however, comes with spatial walk-off between the interacting waves since the Poynting vector and the propagation vector are not in the same direction for the extraordinary wave when the propagation vector is neither parallel nor perpendicular to the optic axis of the crystal. This in turn leads to a reduction in the nonlinear interaction length.

Another technique is quasi phase-matching (QPM) which utilises a nonlinear crystal with spatially modulated nonlinear coefficient to compensate for the phase mismatch. One of the well-established realisations of such a technique is periodic poling of ferroelectric materials such as $LiNbO_{3,}$ in which anti-parallel electric-dipole domains were formed by applying a coercive electric field of ~21 kV/mm (for congruent $LiNbO_3$) along the crystal with a periodicity defined by a lithographic mask with standard microfabrication techniques. Due to the phase shift induced by the domain reversal, the output of the nonlinear process keeps growing at the locations where the interaction would otherwise be in the opposite direction of conversion. The phase-matching condition in equation (2.14) is modified accordingly by the grating vector $\overrightarrow{k_G}$ and becomes:

$$\Delta\overrightarrow{k_Q} = \overrightarrow{k_p} - \overrightarrow{k_s} - \overrightarrow{k_\imath} - \overrightarrow{k_G} = 0 \tag{2.15}$$

where $\overrightarrow{k_G}$ is reduced to a scalar quantity equal to $2\pi/\Lambda$ for collinear process in 1st-order QPM with Λ being the grating period. To illustrate the effect of QPM, an example is shown in Figure 2-6, comparing the growth of second-harmonic intensity [83] generated with different phase-matching techniques in a uniformly poled nonlinear crystal with duty factor of 50%. While Figure 2-6 suggests that QPM is inherently less efficient than BPM, QPM offers several important advantages. For instance, spatial walk-off is avoided, non-birefringent materials such as GaAs can be exploited for nonlinear parametric processes, the largest nonlinear coefficient that cannot be accessed via BPM can be utilized in QPM, and the full spectral transparency range of the nonlinear crystal can be utilised through different grating periods.

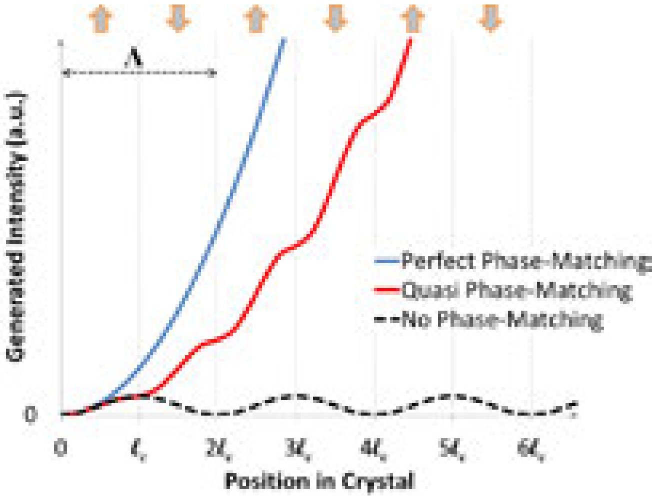

Figure 2-6 Evolution of second-harmonic intensity generated in a uniformly poled nonlinear crystal with different phase-matching techniques-- (blue) perfect phase-matching, (red) 1st-order quasi phase-matching and (black) no phase-matching. Λ is the poling period and l_c is the coherence length. Arrows at the top of the diagram indicate the domain orientations. (For more details, the readers are referred to [83])

2.3.3 *Parametric Gain*

Considering optical parametric processes in a $\chi^{(2)}$ nonlinear crystal, the interaction of the pump, signal and idler waves can be captured with three coupled wave equations derived from the Maxwell's equations. For collinear monochromatic plane waves propagating in the z-direction, the equations with the slowly-varying-envelope and CW assumptions are [82]:

$$\frac{dE_p}{dz} = j\frac{\omega_p d}{n_p c}E_s E_i e^{-j\Delta kz} \quad (2.16)$$

$$\frac{dE_s}{dz} = j\frac{\omega_s d}{n_s c}E_p E_i^* e^{j\Delta kz} \quad (2.17)$$

$$\frac{dE_i}{dz} = j\frac{\omega_i d}{n_i c}E_p E_s^* e^{j\Delta kz} \quad (2.18)$$

where E_m and ω_m are respectively the field amplitudes and angular frequencies of the pump ($m = p$), signal ($m = s$) and idler ($m = i$); n_m is refractive index for the corresponding interacting waves, d is the effective nonlinear coefficient, c is the speed of light in free space and $\Delta\vec{k}$ is the propagation-vector mismatch. Furthermore, when assuming no pump depletion, the solutions to the above coupled equations for the signal and idler are:

$$E_s(z) \propto cosh(gz) \tag{2.19}$$

$$E_i(z) \propto sinh(gz) \tag{2.20}$$

where

$$g = \sqrt{\Gamma^2 - \left(\frac{\Delta k}{2}\right)^2} \tag{2.21}$$

is the gain coefficient and Γ is defined as:

$$\Gamma = \frac{8\pi^2 d^2}{n_p n_s n_i \varepsilon_0 c \lambda_s \lambda_i} I_p \tag{2.22}$$

representing the parametric gain coefficient with λ_s and λ_i being the signal and idler wavelengths and I_p the pump intensity. The single-pass incremental power gain of the signal wave over a crystal length L can be shown to be [84]:

$$G_s(L) = \Gamma^2 L^2 \frac{sinh^2(gL)}{g^2 L^2} \tag{2.23}$$

As an example, in the case of perfect phase-matching, the incremental gain becomes $\Gamma^2 L^2$ in the low-gain regime (ΓL<<1) and $e^{2\Gamma L}/4$ in the high-gain limit (ΓL>>1).

In practice, one or more of the interacting waves in an optical parametric process are focused into the nonlinear crystal to increase the beam intensities for the nonlinear interaction. Moreover, as discussed in Chapter 1 and later in Chapter 4 and Chapter 5, pulsed parametric devices are of great interest to many industries. However, the spatial and temporal influences on the parametric gain in such situations were not taken into account in equation (2.23). Guha carried out an analysis on the conversion efficiency in the near-threshold regime of a singly resonant optical parametric oscillator (SRO) in the presence of arbitrarily focused spatially Gaussian pump and signal beams in CW operation [85]. These results were combined with McCarthy's and Hanna's plane-wave analysis on the parametric gain for temporally Gaussian pulses in a picosecond synchronously pumped OPO (SPOPO) [86] by Hanna et al. to arrive an expression for the single-pass incremental signal gain of an SPOPO with arbitrary focusing conditions [87]:

$$G_s = \frac{128\pi^2 d^2 l_{eff}}{n_p n_s \lambda_i^2 \lambda_s c \varepsilon_0} P_p g_t \xi_s Re\{h_2\} \tag{2.24}$$

where l_{eff} is the effective interaction length as defined in [86], P_p is the pulse peak power, $g_t = \sqrt{\tau_p^2/(\tau_s^2 + \tau_p^2)}$ with τ_p and τ_s being the pump and signal pulse durations, respectively, *Re{h2}* is the real part of a double integral function given in [85] and ξ_s is the focusing parameter of the signal. Considering a crystal with length *L*, the focusing parameter of a beam with a 1/e^2-intensity waist radius of w_0 at wavelength λ is given by:

$$\xi = \frac{L}{b} \tag{2.25}$$

with *b* denoting the confocal parameter defined as:

$$b = 2\frac{\pi w_0^2}{\lambda/n} \tag{2.26}$$

Similar to the case of applying the theoretical models discussed in section 2.2 to predict the performance of fibre amplifiers, the theories presented in this section cannot fully capture the experimental conditions of the optical parametric processes studied in this thesis. However, when employed correctly, they provide a predictive guidance in the interpretation of experimental results and thus complement the experimental arms of the studies. This will be shown accordingly in the later chapters.

2.3.4 Group-Velocity Mismatch

Another parameter that is essential to understand some of the experiments in the later chapters is the group-velocity mismatch (GVM) between two waves, expressed as [62]:

$$GVM_{2,1} = \frac{1}{v_2} - \frac{1}{v_1} \tag{2.27}$$

where v_1 and v_2 are the group velocities of the waves. As seen in section 2.3.2, energy transfer in a parametric nonlinear interaction is efficient only when phase-matching is achieved. GVM of the interacting waves leads to limited phase-matching bandwidth. For example, the full-width-at-half-maximum signal gain bandwidth and pump acceptance bandwidth for parametric conversion in the low-gain regime, along a crystal with length L, can be approximated by $\Delta\omega_{SG} \approx \left|1.772\pi/(GVM_{s,i}L)\right|$ and $\Delta\omega_{PA} \approx \left|1.772\pi/(GVM_{p,i}L)\right|$, respectively [82].

2.3.5 Periodically Poled Lithium Niobate

The choice of periodically poled $LiNbO_3$ (PPLN) as the nonlinear medium for the parametric experiments presented in this thesis was mainly based on the following properties on top of its established technology as a QPM material since the 1990's as well its immediate availability for the project. First, its transparency range from 0.4 to ~5 μm covers the targeted MIR wavelengths for the work while allowing pumping by YDF-MOPAs, which offer such advantages as high efficiency and compact configuration as discussed in section 2.2. Second, PPLN provides access to the largest nonlinear coefficient (d_{33} ~27pm/V for congruent $LiNbO_3$) among the commonly used ferroelectric materials such as potassium titanyl phosphate ($KTiOPO_4$, KTP) and lithium tantalate ($LiTaO_3$, LT).

However, $LiNbO_3$ suffers from the photorefractive effect [88] and from photochromic effects such as green-induced infrared absorption (GIIRA) [89], which can lead to reduced conversion efficiency and degraded beam quality in an optical parametric device, especially when operated at high power. Several approaches can be employed to overcome these problems. For instance, operating the PPLN at an elevated temperature > 100°C can increase the photorefractive resistance by re-diffusing the free carriers. Furthermore, doping with magnesium oxide (MgO) has been demonstrated as an effective means to alleviate both photorefraction and GIIRA by reducing the defect sites in the crystal lattice. The PPLN crystal (Covesion Ltd.) used for the parametric experiments presented in this thesis employed a 5% MgO doping concentration in congruent $LiNbO_3$. While preserving the high nonlinear coefficient, this doping level offers a significant increase in optical damage resistance compared to the undoped version and is thus more suitable for high-power applications.

2.3.6 Optical Parametric Configurations

To conclude the background discussion of optical parametric sources, a comparison on the differences in configuring an OPG, an OPA and an OPO is illustrated in Figure 2-7. An OPG is a simple single-pass device, which on the other hand implies a higher pump threshold to generate signal and idler pulses from the quantum noise level. As will be shown in Chapter 4, an OPA can significantly narrow the signal and idler bandwidths and improves the beam quality compared to an OPG. However, it requires an additional seed laser, thus increasing the system cost and complexity, as well as imposing a limitation on the tuning range of the device. In contrast, an OPO typically provides a broad tunability along with a good beam quality without the need of a seed laser, but its successful operation relies on the alignment of its resonating cavity. These characteristics were demonstrated in the experiments described in Chapter 4 and Chapter 5 where detailed discussions on the performance of each device will be presented.

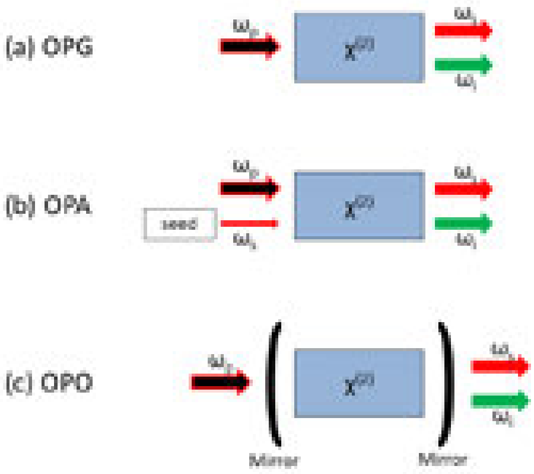

Figure 2-7 Generic configurations of (a) optical parametric generator, (b) optical parametric amplifier, and (c) optical parametric oscillator

2.4 Photonic Crystal Fibres

Photonic crystal fibres (PCFs) are speciality fibres with microstructured air holes running in the longitudinal dimension. Their advantages stem from the tailor-made guiding properties that conventional fibres cannot offer. For example, PCFs with ultra-high nonlinearity, extremely low nonlinearity, all-single-mode operation or shifted zero-dispersion wavelength can be realised with different combinations of parameters such as the hole and pitch sizes, and the core and cladding diameters. Two highly nonlinear PCFs were employed for the supercontinuum work presented in Chapter 6. They belong to the family of solid-core PCFs, in which light is guided in a solid core surrounded by a matrix of air holes that forms an effective lower-index cladding. One of the PCFs used in the experiment is all-normal-dispersion and the other has a zero-dispersion wavelength at 1040 nm.

Various nonlinear behaviours can be excited in a highly nonlinear PCF, leading to the generation of supercontinua with different shapes and degrees of coherence. These are governed by the nonlinear and dispersive profiles of the PCF as well as the pump pulse properties such as wavelength, pulse duration and chirp [38]. For femtosecond pulses propagating in the anomalous GVD regime, strong spectral broadening was generated mainly from a chain of soliton-related dynamics, including soliton formation arising from the interplay of SPM and dispersion, soliton fission, and Raman shifting of the fundamental solitons. The process is inherently sensitive to noise, thus leading to fluctuation in phase and amplitude across the spectra of the pulses. Coherence is not typically achievable in this case [38]. On the other hand, normal GVD forbids the formation of solitons and thus no soliton-related effects exist in this regime. Spectral broadening, which is less strong than in the anomalous regime, is mainly due to the interaction between normal GVD and SPM, which is not sensitive to noise. The resultant supercontinuum is thus expected to have a greater degree of coherence [40], which can be important in many applications.

2.5 Summary

The review of background technology given in this chapter was divided into two parts— Part A concentrated on high-power and high-energy YDF-MOPA technologies while Part B focused on nonlinear frequency conversion via OPGs, OPAs, OPOs and PCFs. The work presented in this thesis involves a number of sub-disciplines; each of them by itself is an extensive research area supported by decades of development. The emphasis of the review in this chapter was placed on the essential mathematics, physics and technologies that are directly relevant to the understanding of the discussion in the later chapters.

From Part A, it was seen that MOPA configurations along with cladding-pumping technology and large-mode-area fibres provide a route to compact and efficient pulsed fibre laser systems with high beam qualities and high output powers. The review started with the operating principles of two compact solid-state lasers, namely GSLDs and ML-VECSELs, followed by a section dedicated to fibre amplifiers. In that section, the basics of fibre optics, a brief development history of fibre amplifiers, and the advantages of using YDFs in high-power systems were included. It also introduced the simplified mathematical models for amplification and the NLSE for pulse propagation in fibres. The core technologies of the pumping architectures for high-power amplifiers in laboratory setting as well as commercial products were presented. After that, the fundamentals of nonlinearities covering SPM and SRS were discussed. At the end, some challenges on high-power fibre amplifiers and possible amplification schemes were explained.

In addition, it was shown in Part B that optical parametric devices and PCFs open doors to highly customisable nonlinear frequency conversion for generating MIR and supercontinua. The review began with the fundamentals of $\chi^{(2)}$-nonlinearity, which underpins the optical parametric experiments presented in this thesis. Then, the principles and advantages of the quasi phase-matching technique for achieving substantial parametric gain were presented. Following that was a discussion on the development and formulations of the single-pass gain models in different operating regimes. Essential advantages of using PPLN in optical parametric devices as well as some techniques to overcome the intrinsic problems were also discussed. After that, a brief comparison on the pros and cons of using OPGs, OPAs and OPOs for parametric processes was illustrated. The review concluded with an introduction to the basics of PCFs as well as how supercontinua are generated via PCFs.

Chapter 3

Compact High-Pulse-Energy and High-Power Picosecond MOPAs

3.1 Introduction

High-power and high-energy ultrashort-pulse laser sources are of interest for nonlinear frequency conversion employing techniques such as optical parametric processes and second harmonic generation [26,28,90–94]. They also span a wide range of activities in material processing for fundamental research and practical applications in both surface and volume processing [14,95–103]. For pulsed-laser deposition (PLD), recent work has provided a relatively new paradigm based on microjoule, picosecond pulses at MHz repetition rates [14] rather than nanosecond pulses at a few tens of Hz. This has enhanced both the reaction rates and throughput. Therefore there has been an interest in developing such kinds of picosecond sources.

With careful design, the master-oscillator power-amplifier (MOPA) approach in combination with cladding-pumping technology and large-mode-area (LMA) fibres, could provide a route to effective power-scaling, compactness and high beam quality, as described in Part A of Chapter 2.

Various systems have been reported to perform power scaling of picosecond laser sources. For instance, a MOPA based on a Nd:YVO_4 mode-locked oscillator and amplifier was built to pump an optical parametric amplifier (OPA) with 18-W average power at 1.5 MHz to demonstrate resonant infrared pulsed-laser ablation (RIR-PLA) [13]. However, the whole system was built with free-space optics, implying that alignment between stages throughout the system was required for daily operation. Another MOPA, seeded by a mode-locked fibre laser, had previously been demonstrated to deliver 3-μJ pulses at an average output power of 150 W and a peak power of 1 MW; however, it also required free-space coupling between stages and the amplifiers were comprised of rod-type photonic crystal fibres with 100-μm core diameter [104], which could not be coiled. On the other hand, a gain-switched-diode (GSD)-seeded MOPA, with a 30μm-core-diameter Yb^{3+}-doped silica fibre (YDF) in the final-stage amplifier, had been shown to deliver a maximum average output power of 200 W at 214 MHz; however, the pulse energy generated was only around 0.9 μJ, with a corresponding peak power of about 30 kW [105]. In that experiment, performance at MHz repetition rate was not explored. Moreover, the demonstrated pulse energy was too low to generate microjoule mid-infrared (MIR) pulses via nonlinear frequency conversion for effective RIR-PLD or RIR-PLA applications. A similar MOPA, which was used for pumping an optical parametric oscillator (OPO), could provide 100-ps pulses at 1064 nm with pulse energy up to around 8 μJ at a maximum average output power of 62 W [27]. However, further energy scaling with this system was primarily limited by the early onset of stimulated Raman scattering (SRS) due to the long length (15.7 m) of active fibres in the MOPA chain, including a 5.7-m-long final-stage power amplifier. Moreover, additional components such as polarisation controllers, a circulator and a chirped fibre Bragg grating were used in the oscillator set-up for chirp compensation, thus increasing the complexity of the configuration. Other approaches for power scaling include chirped-pulse amplification (CPA) and divided-pulse amplification, which are more complicated than direct amplification as they require extra components. While various high-power sources have been demonstrated, sometimes the range of their applications might be limited. For example, a 100-W CPA picosecond source running at 1-MHz burst rate [106] could potentially be useful in the material processing industry; however the 240-nm 3-dB spectral bandwidth made this system unsuitable for nonlinear frequency conversion.

An improvement in energy scaling of picosecond pulses with capability to maintain a narrow spectral linewidth, high peak power and high average power simultaneously would open a door to more scientific and technological opportunities. Furthermore, a stable, compact and robust laser source with simple topology in a fiberised configuration built with shorter and smaller-core commercial fibres, which can be coiled and spliced together, would greatly enhance its practicality; especially in applications that would benefit from stable pulse qualities over an extended period of time.

In particular, besides direct application to material processing, it would be interesting to build a high-energy and high-power source geared towards pumping nonlinear frequency conversion devices to further expand the range of applications by providing high-energy and high-power pulses at widely tunable wavelengths that cannot be directly generated by lasers. For example, the pulses from such a MOPA could be converted into the MIR regime via an OPO, and then be used for RIR-PLD. Specifically, the wavelengths between 2.5 and 4 μm covering the vibrational resonance of a wide range of important functional groups including the OH-stretch and the CH-stretch were targeted. Based on the group-velocity mismatch between the pump and idler waves, the associated acceptance bandwidth described in section 2.3.3 was estimated to be ~1 nm for quasi phase-matching at 152°C in a 4-cm-long periodically-poled lithium niobate (PPLN) crystal. Therefore, it was important to design the MOPA system such that the 3-dB spectral bandwidth of the delivered pulses stayed within 1 nm. Moreover, for efficient nonlinear frequency conversion, a polarisation-maintaining (PM) and near-diffraction-limited beam was desired from our source.

Furthermore, a tunable repetition frequency would enhance the flexibility by introducing an additional degree of freedom to control the power- and energy-scaling of the ultrashort pulses. This would further broaden the span of potential applications and allow for investigation of the parameter space for optimised performance in applications such as RIR-PLD and RIR-PLA. Gain-switching a seed laser offers a route to convenient and broad tunability of the operating repetition rate via the associated driving electronics and without any modification to the laser cavity, as described later in section 3.3.1.

This chapter describes the work on a stable, compact and robust GSD-seeded Yb^{3+}-MOPA system, in a nearly-all-fiberised configuration with a minimum of free-space optics, capable of generating narrow-linewidth picosecond pulses at MHz repetition rate with high pulse energy, high average power and high peak power simultaneously in a diffraction-limited output beam with single polarisation. With an electro-optic modulator (EOM) incorporated as a pulse picker, this MOPA had been demonstrated with high-energy pulses at various repetition frequencies.

Section 3.3 will show that the master oscillator of the MOPA was capable of generating stable pulses with duration of as short as 18.7 ps. Amplifiers were then constructed to extract high pulse energy. When power-scaling longer pulses, as will be presented in section 3.4, the MOPA was demonstrated with pulse energy up to 17.7 μJ with a 97-W maximum average power (excluding amplified spontaneous emission (ASE)). With a measured 90-ps pulse duration, this corresponded to a 197-kW peak power. For bandwidth-dependent applications, such as pumping nonlinear frequency conversion devices, this system was capable of delivering 13.8-μJ pulse energy within a well-confined stable 3-dB spectral bandwidth of 0.87 nm. This bandwidth enabled the system to potentially generate high-energy MIR pulses around 2.5-4 μm by pumping PPLN-based optical parametric devices, as will be discussed in Chapter 4 and Chapter 5. The limits of pulse-energy and power scaling with the system were also explored until SRS became significant (i.e. the spectral intensity of the SRS peak exceeds 1% of that of the signal peak). The repetition frequency was then reduced to 1 MHz to generate high-energy pulses at a relatively lower average power, preparing the system as a pump source for optical parametric processes to generate MIR pulses that would be suitable for RIR-PLD and RIR-PLA applications. To the best of our knowledge, the demonstrated pulse energies is the highest reported so far for GSD-seeded picosecond MOPAs.

The MOPA system presented in this chapter was designed, built and characterised by the author, with the diode pump source for the final-stage amplifier built by Dr. James Bateman and the testing of coupling lenses in that amplifier carried out by Dr. Lin Xu and the author collaboratively. Part of this work was published as a journal paper [107] in Optics Express.

The author was also involved in the work of another picosecond MOPA system that was demonstrated with an average power up to 200 W. In that system, the author enhanced the compactness and thermal loading of the gain-switching configuration by simplifying the driving electronics that was originally implemented by another PhD student Mr. Simon Teh. The author also built the second-stage pre-amplifier, made end-caps for the final-stage amplifier, and collaborated with Dr. Richard Lewis and Mr. Teh on building the cooling system and characterizing the MOPA at a repetition frequency of 214 MHz. This work contributed to a journal publication [105] in Optics Express. This system is not further discussed in this thesis but demonstrates the power scaling capabilities of the GSD-seeded fibre-MOPA generic configuration.

3.2 System Configuration

As depicted in Figure 3-1, the picosecond MOPA consisted of a PM-fibre-pigtailed gain-switched laser diode as the seed, followed by a 4-stage YDF-amplifier chain in a nearly-all-fiberised configuration with a minimum of free-space optics in the final stage. An EOM was used as a pulse picker to provide an additional degree of freedom to control the operating repetition frequency. Fiberised isolators were used to prevent backward ASE leakage between stages, which might otherwise cause damages to the seed and the pre-amplifiers.

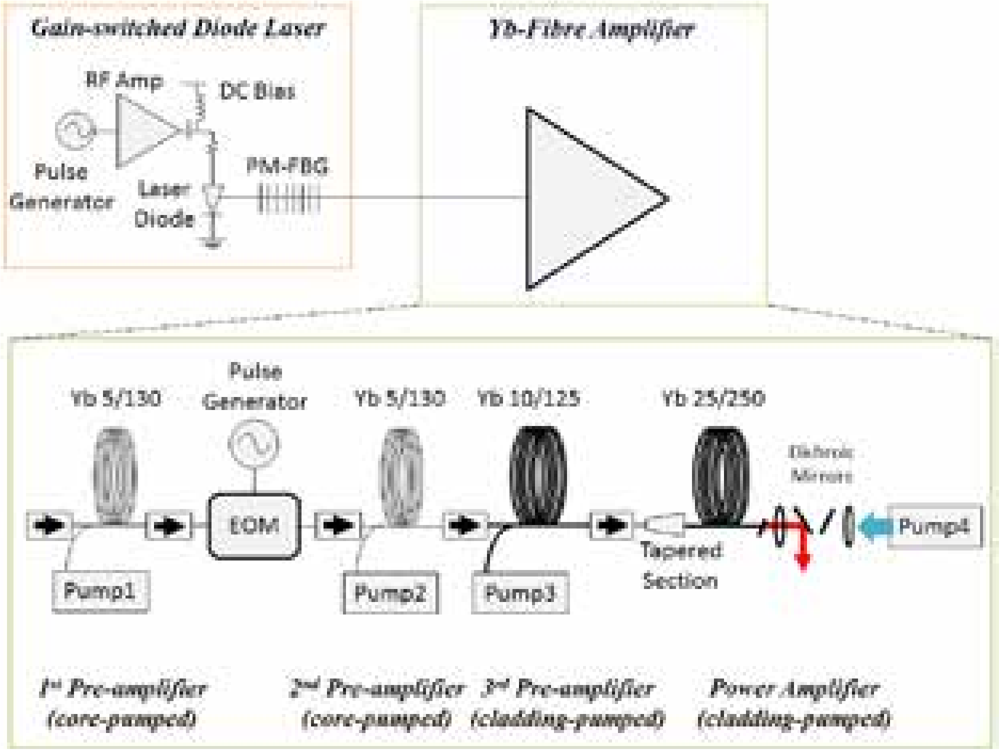

Figure 3-1 PM-picosecond Yb^{3+}-fibre-MOPA system, seeded by a gain-switched laser diode. Red arrow indicates signal output.

There are several advantages in the design of this system. First, the system employed a simple direct-amplification configuration comprising spliced and coiled commercial conventional YDFs with core diameters of ≤ 25 μm and a total length of only 6.6 m. Second, the seed wavelength was chosen such that it resided at the blue edge of the ytterbium gain band in order to minimise the build-up of short-wavelength ASE as well as to allow the lengths of the amplifiers to be kept short. As a result of the reduced length, nonlinear spectral broadening due to self-phase modulation (SPM) and nonlinear energy transfer due to SRS could be minimised. Third, the length of each stage was optimised experimentally to keep ASE and nonlinearity low while ensuring high pump efficiency. Fourth, pulse energies approaching 18 μJ and average powers at the 100-W level were simultaneously extracted. Finally, the stability and robustness of the system indicated its potential for practical use, in addition to a proof-of-concept demonstration.

3.3 Ultrashort Pulse Generation and Energy Extraction Test

3.3.1 Ultrashort Pulse Generation

The set-up of the oscillator in the MOPA system (Figure 3-1) was built around a 1030-nm Fabry-Perot semiconductor laser diode embedded in a hermetically sealed 14-pin butterfly package (Oclaro LC96A1030-20R). For a simpler configuration and lower cost, self-seeding by feedback from a uniform fibre Bragg grating (FBG) was chosen over external injection seeding as mentioned in section 2.1.1, where the operating principle of a gain-switched laser diode was also discussed. Temperature stabilisation of the laser diode was implemented by a thermoelectric cooler. The pulse generator that was used to drive the laser diode could only generate repetition frequencies down to ~40 MHz; therefore an EOM was employed in the MOPA system in order to reach to the MHz repetition rates. The laser diode was DC-biased below the lasing threshold of ~26 mA to avoid continuous-wave leakage and gain-switched by a train of RF pulses with repetition rates matching the synchronisation frequency in the cavity formed by the diode and the FBG to generate ultrashort mode-locked pulses [59]. Detuning from the synchronisation frequency towards the gain-switching regime resulted in broader pulses.

Two PM uniform FBGs with different reflectivity were chosen for investigation of their effects on the properties of the generated pulses. One of them had a centre wavelength of 1040 nm with a reflectivity of 4.4%, and the other was centred at 1034.5 nm with a higher reflectivity of 12.5%. Each of these FBGs was spliced to the pigtail of the laser diode in turn; the physical length of the fibre between the diode and the FBG was ~2.3 m. Temporal and spectral characteristics of the generated pulses in each case were then measured (via tap couplers spliced to the output end of the FBGs) and compared.

With the 4.4%-reflectivity FBG and a 300-mA peak-to-peak current gain-switching the laser diode at 985.2 MHz, the oscillator generated 24.4-ps pulses (fitted to Gaussian profile) at 1039.95 nm. The full-width-at-half-maximum

(FWHM) pulse duration was calculated based on the autocorrelation measurement, shown in Figure 3-2, with an autocorrelator (Femtochrome Research FR-103MN) and a de-convolution factor of 0.707 for Gaussian pulses. Figure 3-3 is the corresponding temporal profile of the pulses measured with a 32-GHz-bandwidth photodetector (Agilent HP 83440D) and a 50-GHz-bandwidth digital communication analyser (Agilent 86100A). RMS time jitter observed on the analyser was ~4 ps; however, most of this jitter was believed to be contributed by the internal jittering of the electronics which was 1-5 ps from the pulse generator and < 2.5 ps for the analyser as specified by their manufacturers. Spectral characteristics were measured with an optical spectrum analyser (OSA) (Yokogawa AQ6317C). As shown in Figure 3-4 (a), the pulses carried a 3-dB bandwidth of 0.11 nm, giving a time-bandwidth product (TBP) of 0.744 which was about 1.69 times of the transform limit of a Gaussian pulse. The optical signal-to-noise ratio (OSNR) was 39 dB (Figure 3-4 (b)). An average power of 8.5 mW was measured after the FBG, corresponding to a pulse energy of 8.63 pJ.

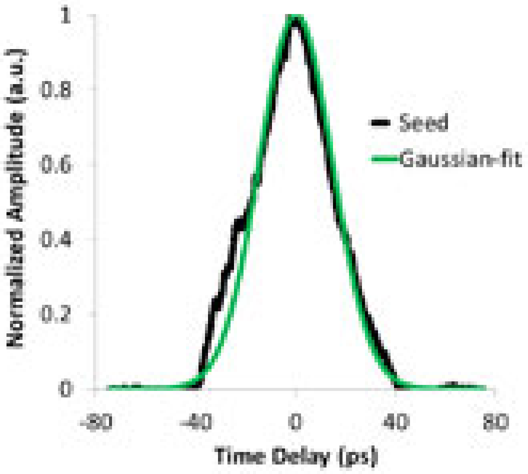

Figure 3-2 Autocorrelation of the pulses generated from the oscillator with the 4.4%-reflectivity FBG

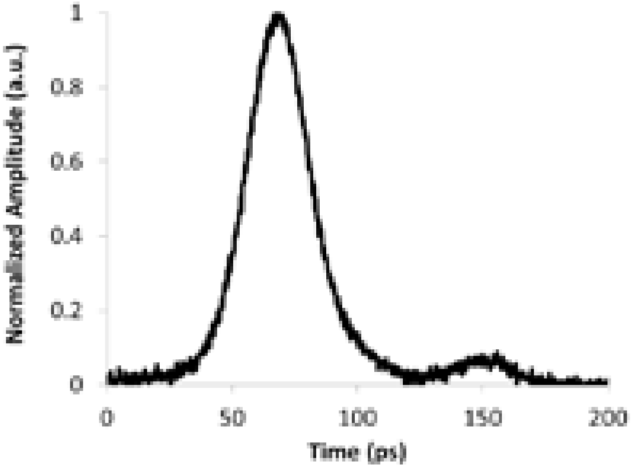

Figure 3-3 Temporal profile of the pulses generated from the oscillator with the 4.4%-reflectivity FBG. Measurement was performed with a 32-GHz-bandwidth photodetector.

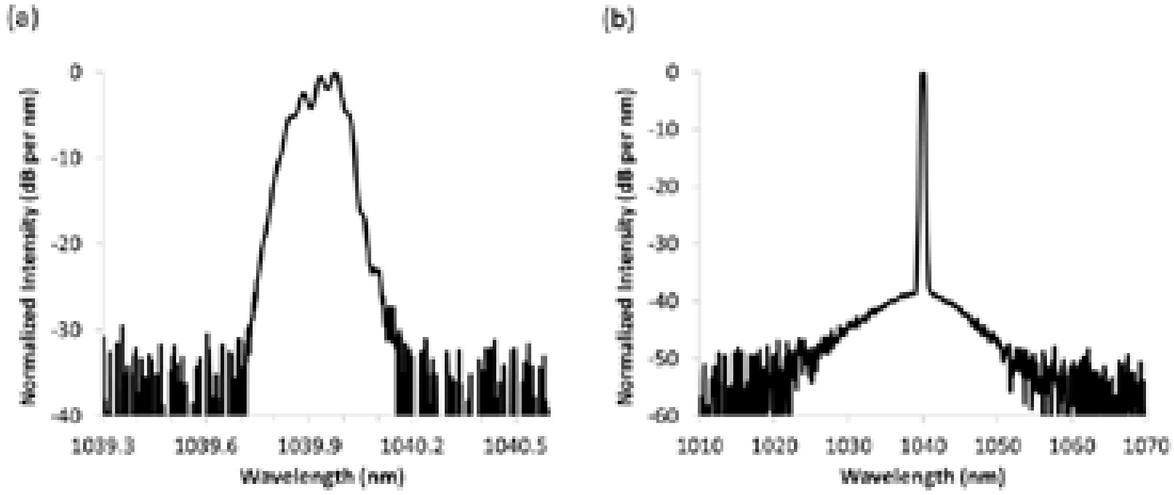

Figure 3-4 Spectrum of the pulses generated from the oscillator with the 4.4%-reflectivity FBG. (a) Resolution = 0.01 nm and (b) resolution = 0.5 nm.

During the experiments, it was observed that the spectrum of the generated pulses was unstable; the spectral profile measured on the OSA fluctuated slightly every few seconds. Adjusting the temperature of the diode did not resolve the problem; therefore the instability did not arise from any thermal issues with the diode, but was believed to be caused by the insufficiently strong self-seeding feedback. This was verified subsequently by the generation of very stable pulses when self-seeding the diode with the 12.5%- reflectivity FBG.

The oscillator with the 12.5%-reflectivity FBG was capable of generating 18.7-ps pulses (fitted to Gaussian profile) at 1034.5 nm with the aforementioned current amplitude at a repetition rate of 963.7 MHz. The autocorrelation measurement is shown in Figure 3-5. The temporal profile of the pulses in Figure 3-6 was measured with a 32-GHz-bandwidth photodetector (Agilent HP 83440D) and a 20-GHz-bandwidth digital communication analyser (Agilent 83480A). The RMS time jitter observed on the analyser was ~3 ps; as mentioned before, most of this jitter was believed to be contributed by the internal jittering of the pulse generator and the analyser. Spectral characteristics were measured with an OSA (ANDO AQ6317B). The 3-dB bandwidth was 0.12 nm (Figure 3-7 (a)), leading to a TBP of 0.629 which was about 1.43 times of the transform limit of a Gaussian pulse. Compared to the 4.4%-reflectivity FBG, the 3-dB bandwidth was about the same but the stability of the spectral profile was greatly improved and there was no observable fluctuation at all. The stronger feedback had also enhanced the OSNR to 45 dB (Figure 3-7 (b)), which was 6 dB better than that with the 4.4%-reflectivity FBG. An average power of 8.9 mW was measured after the FBG, corresponding to a pulse energy of 9.24 pJ and a peak power of ~500 mW.

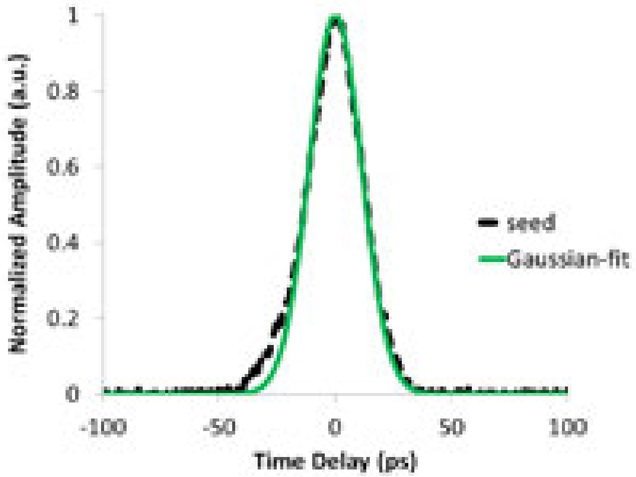

Figure 3-5 Autocorrelation of the pulses generated from the oscillator with the 12.5%-reflectivity FBG

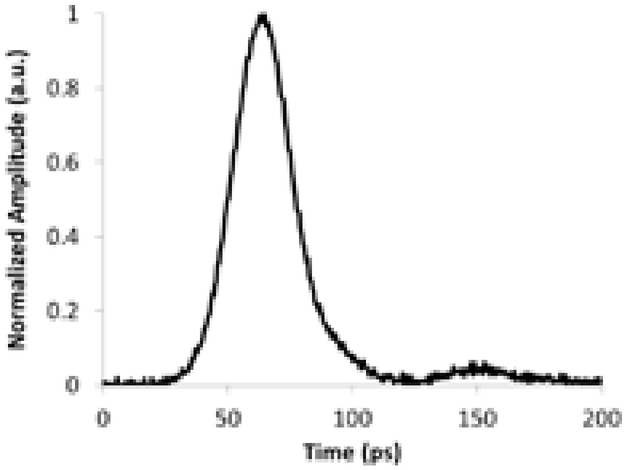

Figure 3-6 Temporal profile of the pulses generated from the oscillator with the 12.5%-reflectivity FBG. Measurement was performed with a 32-GHz-bandwidth photodetector.

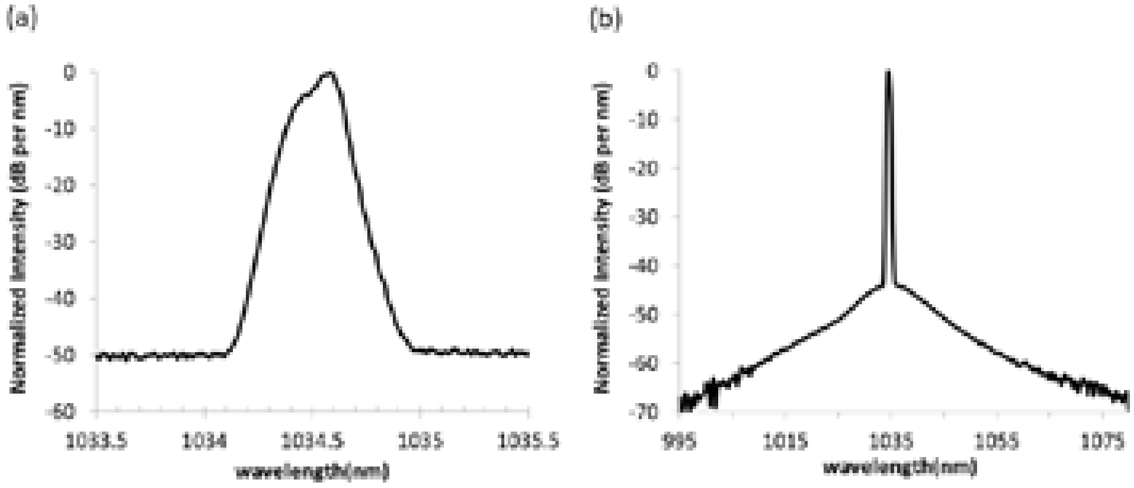

Figure 3-7 Spectrum of the pulses generated from the oscillator with the 12.5%-reflectivity FBG. (a) Resolution = 0.01 nm and (b) resolution = 0.5 nm.

3.3.2 Amplifier Construction

To reach the microjoule regime for RIR-PLD at wavelengths of 2.5-4 μm, it was estimated that pulse energies of at least ~5 μJ would be needed from the YDF-MOPA pump source for the optical parametric process. The MOPA was therefore constructed to amplify the stable 9.24-pJ pulses to reach the required pulse energy level.

The optimisation of amplifier lengths in the MOPA was performed experimentally to assure high pump absorption while ensuring an efficient signal power extraction with limited ASE build-up and SPM broadening. The pump absorption was ~95% in the final-stage power amplifier and ASE was suppressed by at least ~25 dB below the signal throughout the entire pre-amplifier chain.

The first-stage pre-amplifier consisted of an 85-cm-long PM-YDF of 5-μm core diameter and 130-μm cladding diameter, with NA of 0.12 and 0.46, respectively. A 975-nm, single-mode, fibre-pigtailed laser diode with 200-mW available output power was employed to forward core-pump the YDF to amplify the pulses to an average power of 47 mW (48.8-pJ pulse energy). The forward core-pumping was chosen for higher OSNR. A fibre pigtailed electro-optic modulator (EOM) (Photline NIR-MX-LN-10) was then used as a pulse picker to reduce the repetition frequency to 7.53 MHz. A total loss of 26 dB was measured resulting from the 5-dB insertion loss of the EOM as well as a factor of 128 in the reduction of the operating frequency. This relatively high loss dictated the use of an additional pre-amplifier. The second-stage pre-amplifier, having a similar physical configuration to the first-stage pre-amplifier brought the average power to 5 mW (664-pJ pulse energy), ensuring adequate seeding of the third-stage pre-amplifier. The third pre-amplifier was composed of a 2.5-m-long PM-YDF that had a core diameter of 10 μm with an NA of 0.075 and a cladding diameter of 125 μm with an NA of 0.46. Pump power up to 10 W was provided by a 975-nm, multi-mode, fibre-pigtailed laser diode. The active fibre was forward cladding-pumped to scale the average output power to around 16 mW, corresponding to a pulse energy of 2.12 nJ. A TEC was implemented to thermally stabilise the pump diode. The pulses were then fed into the final-stage amplifier. Fiberised isolators were used to prevent backward ASE leakage between stages.

The final-stage power amplifier comprised a 2.5-m-long commercial large-mode-area (LMA) PM-YDF (Nufern PLMA-YDF-25/250-VIII), which had a core diameter of 25 μm with an NA of 0.06 and a cladding diameter of 250 μm with an NA of 0.46. An angle-polished silica end-cap was spliced to the output end of the fibre to reduce the risk of facet damage. Although this LMA fibre could support two spatial modes, namely LP_{01} and LP_{11}, an in-house-made tapered section was used to preferentially excite the fundamental mode. A fibre-coiling diameter of 80 mm was used to enhance the leakage loss for the LP_{11} mode in order to maintain single-mode operation while maintaining a low loss for the LP_{01} mode. An array of 975-nm, multi-mode, fibre-coupled laser diodes, each with a maximum output power of 50 W, were combined through a 7x1 pump combiner to form the pump source for the power amplifier. The pump delivery fibre had a cladding diameter of 125 μm and an NA of 0.46. Free-space backward-pumping was employed to reduce nonlinearity and maximise the conversion efficiency. Aspherical lenses with focal lengths of 12 mm and 8 mm were used to couple light for the YDF and the pump delivery fibre, respectively. At optimised alignment, a pump coupling efficiency of

95.5% was measured. Dichroic mirrors were placed between the coupling lenses to separate the pump and signal beam. Residual pump light in the power amplifier was stripped in the tapered section. To increase the robustness and stability of the amplifier, a water cooling system was implemented to minimise the risk of thermal damage to the LMA fibre as well as to reduce thermal drift of the pump wavelength. The LMA fibre was put in a water-cooled assembly made of aluminium plates with ~1 mm of stripped fibre extending out for pump launch.

3.3.3 Energy Extraction Test

The pump power of the final-stage amplifier was then turned up to test the energy extraction capability until the SRS spectral peak intensity reached 20 dB below the signal peak. At this operating point, the pulse energy was 3.2 μJ. This was based on the 23.8-W average power calculated by taking into account the contribution due to ASE, estimated from the spectrum measured at the output power of 28W (see red line in Figure 3-8).

Figure 3-8 illustrates the spectral evolution of the amplified pulses at the MOPA output as the pump power increased. The spectra were measured with an OSA (ANDO AQ6317B). The SRS peak at ~1082 nm started to become apparent when the average power scaled beyond ~17 W, corresponding to a peak power of ~120 kW. As the signal power further increased from 17 W to 23.8 W (i.e. a factor of 1.4), the SRS peak spectral intensity rapidly grew by more than 10 dB, reaching to 20 dB below the signal peak. At this operating point, the OSNR was ~17 dB. Figure 3-9 plots the spectral profiles of the pulses at the output of the oscillator and after each amplifier of the MOPA chain when the system was delivering pulse energy of 3.2 μJ. Further energy scaling was primarily limited by the rapid growth in the SRS level. Autocorrelation measurement of the 3.2- μJ pulses at the MOPA output showed a pulse duration of 17.4 ps, which was shorter than that of the seed pulses. However, it is believed that the pulse width would be about the same as the seed pulse if a spectral filter were used to exclude the wavelengths beyond 1050 nm, which will be shown in section 3.4.1 where similar phenomenon was observed when the MOPA was seeded with 120-ps pulses. Therefore the peak power attained by the signal pulse was about 166 kW at the maximum operating condition.

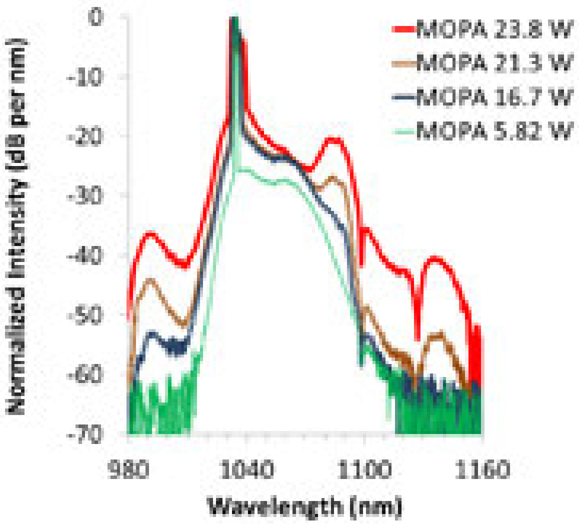

Figure 3-8 Spectral evolution (resolution = 0.5 nm) when power and energy scaling were performed.

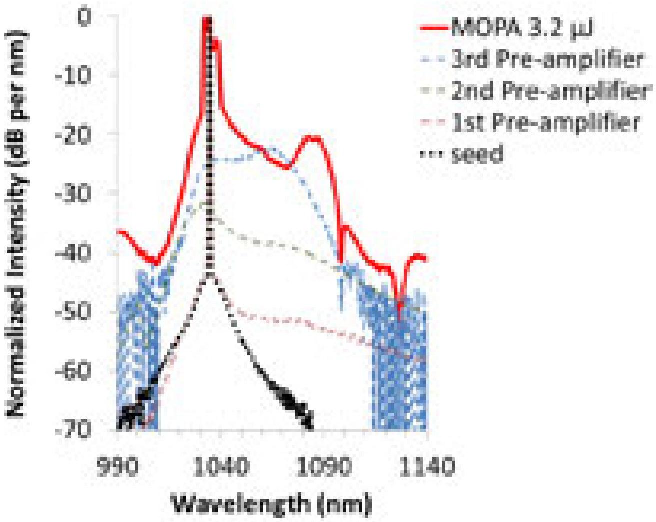

Figure 3-9 Spectra (resolution = 0.5 nm) measured at the output of the oscillator and after each amplifier of the MOPA system when the pulse energy reached 3.2 μJ

In the above energy extraction test with the 18.7-ps pulses, the maximum pulse energy delivered by the MOPA was limited by nonlinear effects to only ~60% of the target. It should also be noted that the 3-dB bandwidth of these pulses had increased to 2.7 nm, which was broader than desired for parametric frequency conversion mentioned in section 3.1. In order to achieve the required pulse energies of ~5 μJ, one of the solutions would be to replace the fibre in the final-stage power amplifier with another fibre that had a larger core diameter to reduce the nonlinearity. Unfortunately, there was no access to such a fibre in a short period of time. An alternative and quicker approach was to generate longer pulses from the oscillator and amplify them to higher energies (but similar peak powers) through the MOPA. Characterisation of the MOPA operated in this regime will be presented in the next section, showing extracted pulse energies of more than 3 times of the targeted level.

3.4 High-Power and High-Pulse-Energy MOPA

With the 12.5%-reflectivity FBG in the oscillator, 120-ps pulses were generated with a current of 270-mA amplitude at a repetition rate of 87.5 MHz, as the operation moved towards the gain-switching regime. These pulses spectrally centred at 1034.5 nm with a 3-dB bandwidth of 0.026 nm and an OSNR of 43 dB. The temporal profile is shown in Figure 3-10 and the spectral characteristics at 0.01-nm and 0.5-nm resolution are illustrated in Figure 3-11. The resulting TBP was 0.874, which was almost twice the transform limit of a Gaussian pulse; this was higher than that of the pulses in section 3.3.1 as expected since the pulses here were not mode-locked. The generated pulse energy was 3.77 pJ, calculated based on the measured average power of 0.33 mW for the pulses.

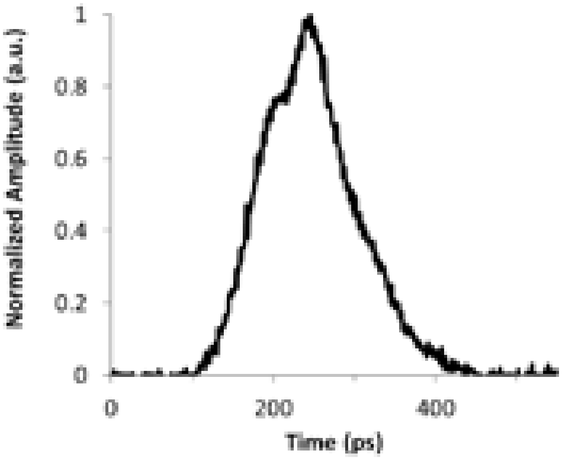

Figure 3-10 Temporal pulse profile of the pulse generated from the oscillator. Measurement was performed with a 32-GHz-bandwidth photodetector.

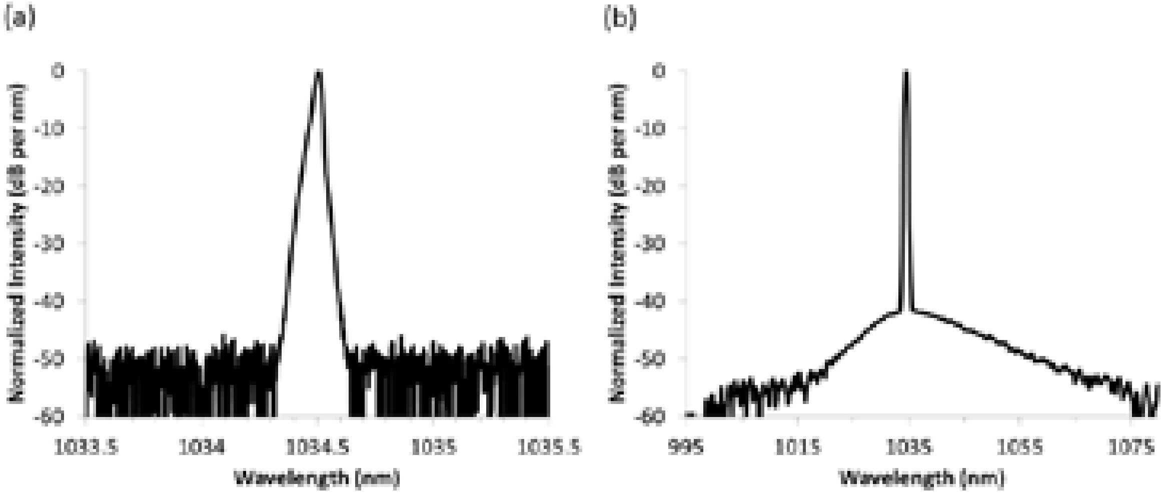

Figure 3-11 Spectrum of the pulse generated from the oscillator. (a) Resolution = 0.01 nm and (b) resolution = 0.5 nm

In this experiment, the goals were to extract higher pulse energies as mentioned in the previous section and to simultaneously amplify the pulses to attain high average powers at the 100-W level. With the 120-ps pulses, these could be achieved by operating the MOPA at a repetition rate of ~5 MHz. The pulses generated from the oscillator were passed into the amplifier chain through a fiberised isolator as shown in the set-up in Figure 3-1. After the first-stage pre-amplifier, the pulses attained an average power of 17 mW (194-pJ pulse energy). With the EOM running at 5.47 MHz, a total loss of 17 dB was measured. The second-stage pre-amplifier then brought the average power back to 12 mW (2.19-nJ pulse energy) to ensure adequate seeding of the third-stage pre-amplifier, which scaled the average power to around 80 mW, corresponding to a pulse energy of 14.6 nJ. Carrying the same 3-dB bandwidth and temporal profile as the seed pulses, the pre-amplified pulses were fed into the final-stage amplifier through a fiberised isolator and a tapered section, as aforementioned, for high-power scaling and high-pulse energy extraction.

3.4.1 High-Power and High-Energy Performance

The average output power (excluding ASE) of the MOPA system is plotted against the launched pump power of the final-stage amplifier in Figure 3-12, showing a slope efficiency of 79%. An overall energy gain of 66.7 dB was achieved through the MOPA system, reaching 17.7 μJ. This was based on the 97-W maximum average power calculated by taking into account the contribution due to ASE, estimated from the spectrum (Figure 3-15) measured at the total output power of 109 W. The gain provided by the power amplifier was more than 30 dB.

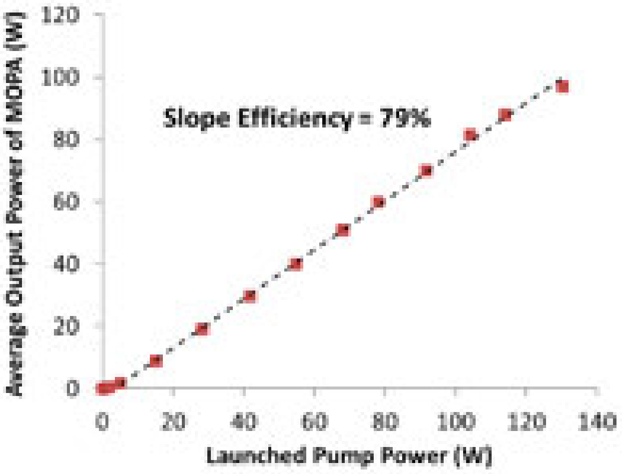

Figure 3-12 Average output power (excluding ASE) versus launched pump power of the final-stage power amplifier

The design of the pre-amplifier chain provided a good suppression of nonlinearity before the pulses entered the power amplifier. This means that significant SPM only took place in the final stage of the MOPA, leading to a broadening of the 3-dB spectral bandwidth from 0.026 nm to 0.87 nm when the power and energy were scaled up. This effect is delineated in Figure 3-13. The spectral profile of the seed pulse was included in the figure as a reference. It can be seen that the spectral broadening became apparent when the average output power exceeded 19 W, corresponding to a pulse energy of 3.5 μJ. When the pulse energy reached 17.7 μJ at average output power of 97 W, the 3-dB and 10-dB spectral bandwidths of the signal broadened to 0.87 nm and 1.08 nm, respectively. Figure 3-14 plots the spectral profiles at 0.5-nm OSA resolution, showing the change in the measured OSNR from the output of the oscillator to the output of the MOPA when the system was delivering the maximum pulse energy of 17.7 μJ. The OSNR decreased from 43 dB at the seed stage to 25 dB after the 3rd pre-amplifier, and finally to 18 dB after the power amplifier at the maximum operating condition.

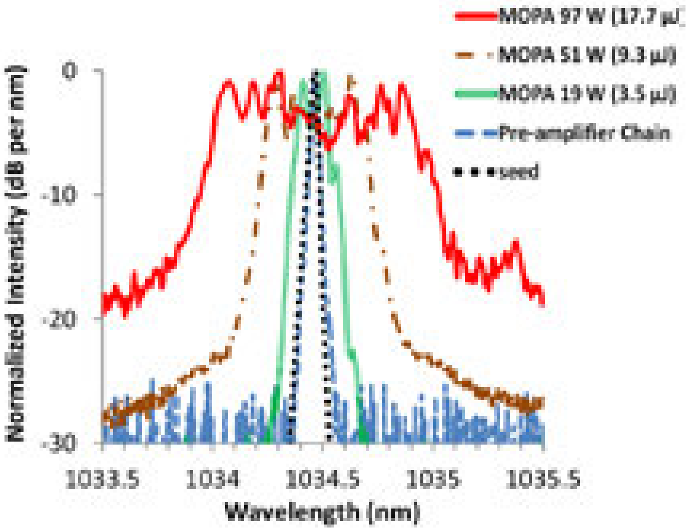

Figure 3-13 Spectra (resolution = 0.01 nm) measured after the seed, after the pre-amplifier chain and at different average output power (and energy) levels of the MOPA system.

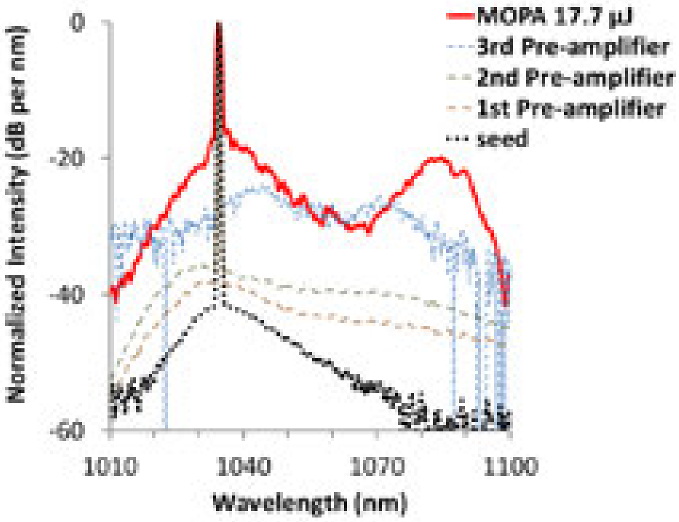

Figure 3-14 Spectra (resolution = 0.5 nm) measured at the output of the oscillator and after each amplifier of the MOPA system when the pulse energy reached 17.7 µJ.

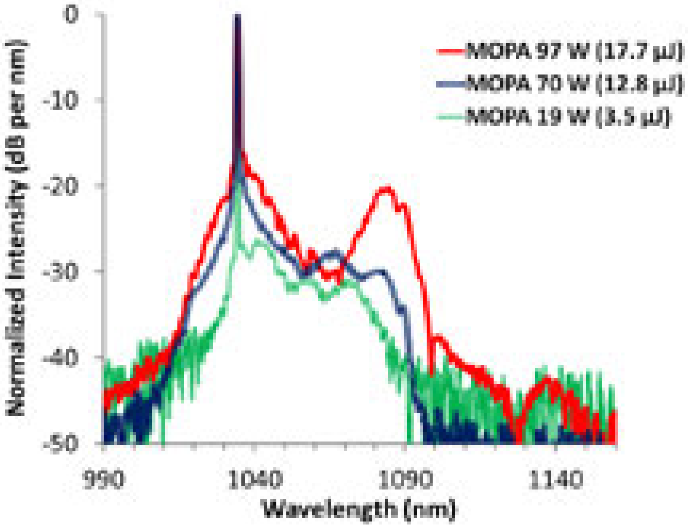

Figure 3-15 Spectral evolution (resolution = 0.5 nm) when power and energy scaling were performed

An exploration of the limits on the capability of pulse energy and power scaling with the MOPA system was performed. The associated spectral evolution shown in Figure 3-15 clearly indicates a rapid growth of the SRS peak spectral intensity as the power scaled up. When the average output power reached 70 W, corresponding to a peak power of 107 kW, the SRS peak at ~1082 nm started to become apparent and lay at 30 dB below the signal peak. However, as the output power increased from 70 W to 97 W (i.e. a factor of 1.38), a rapid 10-fold growth of the SRS peak spectral intensity was observed, reaching to 20 dB below the signal peak. At this point, 0.87-nm 3-dB spectral bandwidth of the pulses, carrying 13.8-μJ pulse energy, sat well within the targeted 1-nm acceptance bandwidth for MIR generation via a PPLN-based OPO. Further energy scaling would escalate the SRS level.

In the temporal domain, a 90-ps pulse width was measured at the output of the MOPA system, as illustrated in Figure 3-16, where the seed pulse is included for comparison. This implied a peak power of 197 kW for the 17.7-μJ pulses at a repetition rate of 5.47 MHz. By using a spectral filter (Semrock LP02-1064RU-25) to exclude the wavelengths beyond 1050 nm, it was found that the measured pulse width increased to 124 ps, which was comparable to the 120-ps duration of the seed pulse. This was expected since the dispersion length defined in equation (2.9) was 4 orders of magnitude longer than the total fibre length of the MOPA. With the peak power of 130 kW attained by the 124-ps pulses, the peak nonlinear phase shift accrued in the final amplifier stage was estimated to be ~5π [62]. Figure 3-17 showed the two measured temporal profiles corresponding to the wavelengths below and above1050 nm respectively. The latter had a pulse width of 70 ps. All the pulse widths were measured at the FWHM using a 20-GHz digital communication analyser (Agilent HP 83480A) and a photodetector with 32-GHz bandwidth (Agilent HP 83440D).

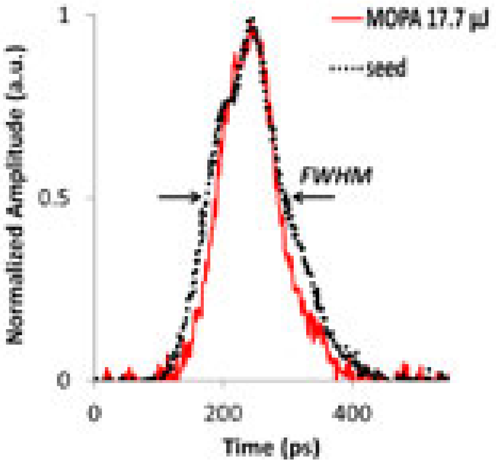

Figure 3-16 Temporal profiles of the pulses before and after amplification. Measurement was performed with a 32-GHz-bandwidth photodetector.

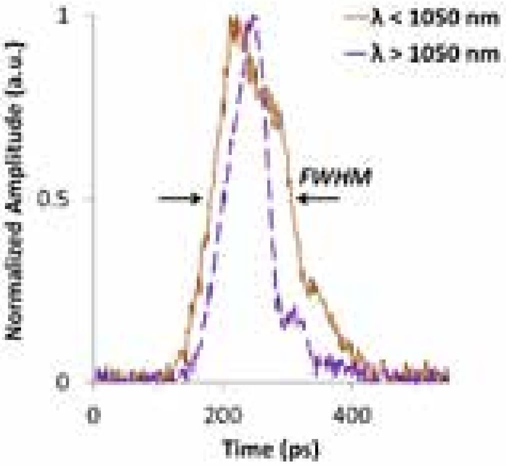

Figure 3-17 Temporal profiles corresponding to wavelengths below and above 1050 nm separated by a spectral filter. Measurement was performed with a 32-GHz-bandwidth photodetector.

At the maximum operating condition, an output polarisation extinction ratio (PER) of > 14 dB was measured with a half-wave plate and a polarisation beam-splitter (ER ≳ 1000). A diffraction-limited beam quality of $M^2 \approx 1.06$ was measured with a beam profiler (Thorlabs BP209-IR). Fluctuation of only ~1% was observed in the output power over 30 minutes of continuous operation at the maximum power, with no change in the spectral and temporal profiles, highlighting the stable and practical attributes of the system when operating in the high-power and high-energy regime. Therefore this system was not merely a proof-of-concept demonstration, but also a promising source for high-throughput material processing and for pumping nonlinear frequency conversion devices to reach high-power and high-energy pulses at other wavelengths such as the MIR regime.

3.4.2 MOPA towards RIR-PLD and RIR-PLA Applications

Under the operating conditions in section 3.4.1, at 100-W-level average power, the designed MOPA was capable to deliver more than 3 times of the required pump pulse energy for nonlinear frequency conversion to generate microjoule MIR pulses for RIR-PLD and RIR-PLA applications. On the other hand, other experiments had shown that average powers of greater than ~20 W could sometimes lead to associated thermal effects in PPLN-based OPOs [108]. In order to avoid this possible complication it was decided to operate the MOPA at a lower average power whilst maintaining the high pulse energy.

Without changing any parameters of the oscillator, the repetition frequency of the MOPA output was reduced to 1.006 MHz via the EOM. In this operating regime, the average power at the MOPA output was 17.4 W, corresponding to an extracted pulse energy of 17.3 μJ, when the SRS peak spectral intensity reached to 20 dB below the signal peak; the OSNR at this point was 15.5 dB (Figure 3-18). The 3-dB and 10-dB spectral bandwidths of the signal were broadened to 0.88 nm and 1.09 nm respectively. Similar to the operating regime in section 3.4.1, there was no spectral broadening before the pulses entered the final-stage amplifier, as delineated in Figure 3-19.

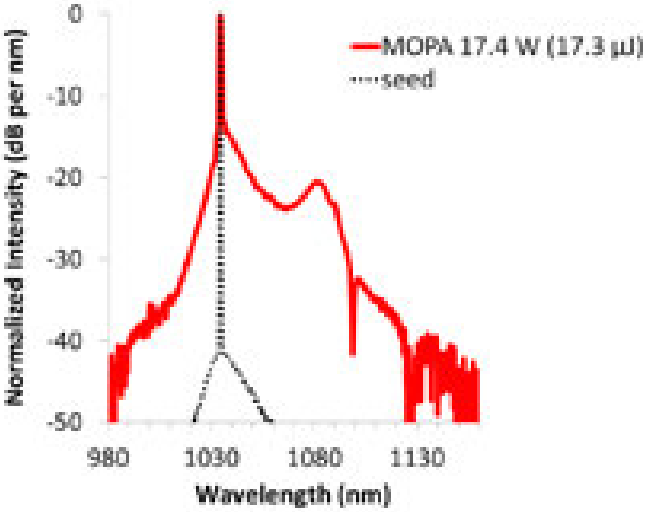

Figure 3-18 Spectrum (resolution = 0.5 nm) measured at the MOPA output when the power was scaled to 17.4 W

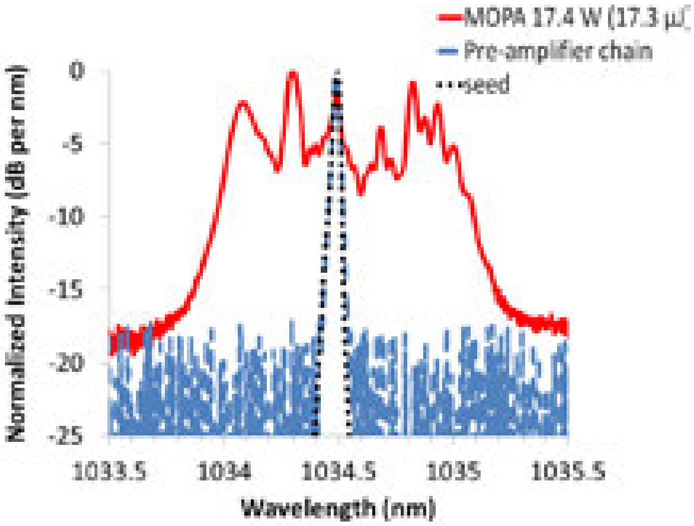

Figure 3-19 Spectra (resolution = 0.01 nm) measured after the seed, after the pre-amplifier chain and at the MOPA output

By operating the MOPA at repetition frequency of 1 MHz, the system was demonstrated with pulse energy, spectral linewidths and pulse duration practically the same as those when operating the system at 5.47 MHz at the 100-W-level average power. Combined with single-polarisation and a diffraction-limited beam quality, this MOPA became an attractive pump source for nonlinear frequency conversion to generate MIR pulses with the targeted pulse energies, average powers and repetition rate suitable for RIR-PLD and RIR-PLA applications. Application of this MOPA as a pump source for various optical parametric devices to generate such MIR pulses will be demonstrated in Chapter 4 and Chapter 5.

3.5 Summary

This chapter has presented a stable, compact, robust and flexible GSD-seeded MOPA system capable of producing high-energy, high-peak-power and high-average-power picosecond pulses with narrow linewidth in a diffraction-limited and single-polarisation output beam. It employed simple direct amplification through commercial conventional YDFs with core diameters of ≤ 25 μm and a total length of 6.6 m. The MOPA was nearly all-fiberised with a minimum of free-space optics in the final-stage power amplifier.

Pulse durations as short as 18.7 ps were realised with a gain-switched laser diode self-seeded by the reflection of a 12.5%-reflectivity FBG. A 4-stage amplifier chain was built to boost the power and extract high pulse energy. An average power of 23.8 W was achieved, corresponding to a pulse energy of 3.2 μJ at a repetition rate of 7.53 MHz. The peak power achieved was ~170 kW, at which point the SRS became significant and the 3-dB spectral bandwidth was broadened to 2.7 nm. Further energy scaling was primarily limited by SRS and broadening of the pulse spectrum.

With 120-ps pulses fed into the amplifier chain from the master oscillator, an overall energy gain of 66.7 dB was achieved, reaching pulse energies of 17.7 μJ at 5.47-MHz repetition frequency. With an average output power of 97 W, a maximum peak power of 197 kW was demonstrated. The measured 3-dB spectral bandwidth of 0.87 nm contained 13.8-μJ pulse energy, making this MOPA an attractive high-energy source for bandwidth-dependent applications. The PER and M^2 were measured to be > 14 dB and ≈ 1.07 respectively at the maximum operating condition. Stability tests showed a power fluctuation of only ~1% over 30 minutes of continuous operation at the maximum output power, with no change in the spectral and temporal domains. By providing pulse energies approaching 18 μJ simultaneously with 100-W-level average power at MHz repetition rates in a diffraction-limited and single-polarisation beam, combined with narrow spectral linewidth and 200-kW-level peak power, this compact, stable and robust picosecond source should be attractive to diverse sectors for a variety of applications, especially in high-throughput material processing and for nonlinear frequency conversion to generate high-energy pulses in other spectral regions. In particular, when operating at 1-MHz repetition frequency, it became a promising pump source for optical parametric devices, e.g. a PPLN-based OPO, to generate MIR pulses with energies and average powers that had been shown adequate for RIR-PLD and RIR-PLA applications. Practical applications of this MOPA system will be demonstrated through the work in Chapter 4 and Chapter 5 where this MOPA was used as a pump source for various optical parametric processes.

Chapter 4

High-Energy Mid-Infrared Generation: Fibre-MOPA-Pumped Picosecond OPG, OPA and OPO

4.1 Introduction

As stated in section 1.1.1, there is a lack of compact, economical and broadly tunable laser sources that are suitable for resonant infrared pulsed-laser deposition (RIR-PLD) and ablation (RIR-PLA), where microjoule picosecond mid-infrared (MIR) pulses running at MHz repetition rates have been shown to be advantageous. Various systems based on the approach of optical parametric conversion of readily available near-infrared (NIR) picosecond lasers have been previously demonstrated but unfortunately each has its own drawbacks.

For instance, an optical parametric generator (OPG) with a periodically-poled lithium niobate (PPLN) crystal pumped by 7-ps pulses from a Nd:YVO$_4$ mode-locked MOPA system at 82-MHz repetition rate, has demonstrated an idler average power of 2.6 W [26]. However, the maximum MIR pulse energy generated was less than 3% of what would be required for RIR-PLD applications. Other OPG systems delivering μJ-level MIR pulse energies have been reported, but they were usually operated at Hz or kHz repetition frequency; for example, 150-ps pulses with 3.7 μJ of energy at ~4 μm was generated from a CdSiP$_2$-based OPG [109] but at a repetition rate of 1 kHz, which is too low for efficient RIR-PLD processes.

Another MOPA system based on a Nd:YVO$_4$ mode-locked oscillator and amplifier was built to pump a dual-stage PPLN-based optical parametric amplifier (OPA) with 18-ps pulses to generate 1.3-μJ MIR pulses at a repetition frequency of

1.5 MHz to demonstrate resonant infrared pulsed-laser ablation (RIR-PLA) at 3.5 μm [13]. While the pulse energies and repetition rate were suitable for RIR-PLA and RIR-PLD applications, the tunability of the OPA was limited by that of the seed laser to only 35 nm, which limited the range of materials that can be processed.

A fibre-feedback PPLN-based optical parametric oscillator (OPO), synchronously pumped by 100-ps pulses from a gain-switched-diode (GSD)-seeded YDF-MOPA, has been demonstrated with pulse energies of 0.49 μJ at 1.5 μm and 0.19 μJ at 3.6 μm with tunability from 1.5 to 1.7 μm (signal) and 2.9 to 3.6 μm (idler) at a repetition rate of 7.19 MHz [27]. However, the generated MIR pulse energies were less than 20% of what would be required for RIR-PLD applications.

The need for a compact and practical picosecond pump source for parametric conversion to MIR pulses that are required for efficient RIR-PLD and RIR-PLA applications has been fulfilled by the GSD-seeded YDF-MOPA presented in Chapter 3. This chapter presents the work on the investigation of generating such MIR pulses via three different optical parametric devices with relatively simple configurations, namely OPG, OPA and free-space-cavity OPO. There are pros and cons in each of the devices. OPGs can be attractive because of their simple single-pass nature, leading to devices that are more compact and less sensitive to external perturbations compared to OPOs, which require a resonating cavity. However, as a result of the single-pass interaction, OPGs require higher-intensity pump pulses to achieve a high parametric gain for generating high-energy signal and idler pulses starting from the quantum noise level. Moreover, the signal and idler pulses generated from OPGs are usually spectrally broader than those from OPAs [26,109,110] and therefore might not be suitable for bandwidth-dependent applications. The M^2 of both the signal and idler generated from an OPA are typically smaller than those from an OPG [110]. However, the tuning range of an OPA is usually limited without a tunable seed laser. In contrast, OPOs typically provide a broad tunability as well as a good beam quality [108]; however, operating at MHz repetition rates implies a cavity length of several 10s to several 100s of metres if the fibre-feedback or relay-imaging technique were employed; thus an alternative approach allowing a shorter cavity was explored in the work.

In section 4.3, an MgO:PPLN-based OPG is shown to generate signal and idler pulses with tunable wavelengths of 1.48-1.79 μm and 2.45-3.45 μm, and pulse energies up to 3.2 μJ and 1.4 μJ, respectively. The 3-dB spectral bandwidth of the signal was 5.6 nm and that of the idler was 38 nm. Section 4.4 shows the performance of the OPA when two lasers with different linewidths were used to seed the OPG in turn. When seeding with the narrower-linewidth laser, maximum pulse energies of 3.3 μJ (signal) and 1.6 μJ (idler) were achieved before the crystal was damaged. The increase in pulse energies was a result of a decrease in the pump threshold. Moreover, the 3-dB spectral bandwidths of the generated signal and idler were significantly reduced to 0.06 nm and 6.7 nm, respectively. On the other hand, it was observed that using the seed laser with a broader linewidth enabled the OPA to take in the full pump power without any damage to the crystal, leading to a further increase in maximum achievable pulse energies of 4 μJ and 1.87 μJ for the signal and idler, respectively.

Section 4.5 presents an OPO with a harmonic cavity where the cavity length was a factor of 192 times smaller than that required for a conventional synchronously pumped OPO, leading to a compact cavity even when pumped at MHz repetition rate. Prior work has been reported on the use of such kind of cavities but the focus was mainly to generate GHz signal pulses in both femtosecond and picosecond signal-resonating OPOs [111,112]. The cavities in those experiments required signal output coupling and the large number of round-trips experienced by the signal pulses before the arrival of the next pump pulse incurred a significant intracavity loss. In contrast, the interest of the work presented here was the generation of high-energy idler pulses at MHz repetition rates by employing a harmonic cavity in which the resonating signal ran at a repetition frequency of ~200 times of that of the pump without output coupling. Idler pulse energy of as high as 1.8 μJ was achieved along with tunability in the MIR region of 2.3-3.5 μm. To the best of our knowledge, these are the highest MIR pulse energies achieved so far for a picosecond OPO.

The optics between the pump source and the OPG/A/O were built by the author while initial calculation of the OPO cavity parameters and its initial alignment were carried out by Dr. Lin Xu, who collaborated with the author to perform the experiments on the OPG, OPA and OPO. The filtered ASE source used in the OPA for the investigation of broader-bandwidth seeding was built by Dr. Yongmin Jung and the author with components from the Optical Fibre Communications group at the department. The data analysis presented in this chapter was performed by the author. The work described in this chapter contributed to two journal papers; one in Optics Express [113] and the other in Optics Letters [114]. Unless specified otherwise, all the signal and idler output powers and pulse energies mentioned in this chapter are referred to those after the exit facet of the PPLN in the cases of the OPG and OPA or after the output mirror of the OPO, taking into account the losses of the optical elements involved in the measurements.

4.2 System Configuration

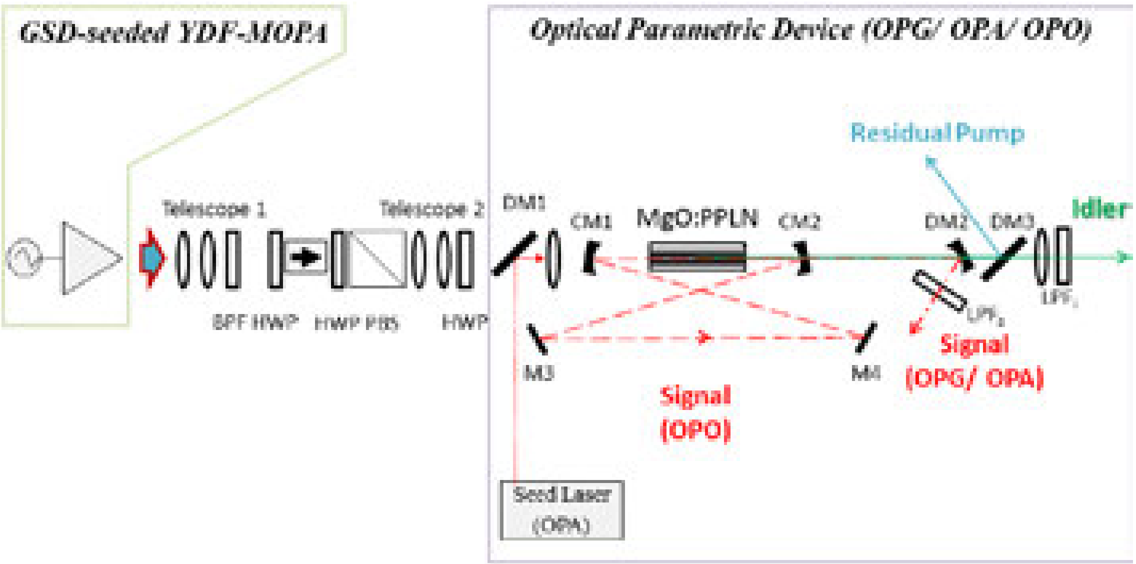

Figure 4-1 Set-up of the experiments on high-energy MIR generation via different optical parametric processes, OPG, OPA and OPO, pumped with a compact high-pulse-energy GSD-seeded YDF-MOPA at a repetition rate of 1MHz. BPF = band-pass filter, HWP = half-wave plate, PBS = polarisation beam splitter, DM = dichroic mirror, CM = curved mirror, M = plane mirror, LPF = long-pass filter.

The schematic of the experimental set-up is illustrated in Figure 4-1. The pump source was a GSD-seeded YDF-MOPA system delivering 124-ps pulses with pulse energy of as high as 17.3 μJ at a repetition rate of 1.006 MHz in a linearly polarised and diffraction-limited beam. The pulses were centred at 1034.5 nm with a 3-dB spectral bandwidth of 0.8 nm. Details of the design and performance of this MOPA system are discussed in Chapter 3 of this thesis.

A band-pass filter (BPF) centred at 1025 nm with a 3-dB bandwidth of 50 nm was used to exclude the SRS and ASE outside the signal region from the high-energy NIR pulses, followed by a free-space optical isolator to protect the MOPA from any accidental back-reflection from the optical parametric device. A variable attenuator was implemented by combining a half-wave plate (HWP) with a polarisation beam-splitter (PBS) to control the pump power for the parametric processes. A two-lens telescope (Telescope 2) formed by lenses with focal lengths of 75 mm and 40 mm as well as a focusing lens with 250-mm focal length were then used to obtain the required pump waist size and location inside the nonlinear crystal for the experiments in sections 4.3 and 4.4, while the focusing lens alone was used in section 4.5. Unless specified otherwise, all the spot sizes mentioned in the rest of the chapter are referred to the $1/e^2$-intensity waist radii. Pump waists ranging from 77.5 μm to 87.5 μm were used for the experiments to ensure high peak intensity for parametric conversion whilst avoiding the crystal damage threshold of ~1 GW/cm^2 reported by the manufacturer. A half-wave plate was placed in front of the optical parametric devices to set the polarisation of the pump beam for optimisation of the quasi phase-matching.

The nonlinear gain medium used in the optical parametric experiments was a 40-mm-long, 1-mm-thick PPLN crystal (Covesion Ltd.) with a 5% magnesium oxide doping concentration. High beam intensity and long nonlinear interaction length were desired for high parametric conversion efficiency. The beams were to be focused at the centre of the crystal without damaging it, but divergence increases with the tightness of the focusing. In addition to passing of beams through channel aperture, temporal walk-off among the interacting waves and acceptance bandwidth of the crystal were also taken into consideration when determining the crystal length. The longest available from our suppliers was 40 mm. It consisted of five periodically poled gratings with periods of 29.52 μm, 29.98 μm, 30.49 μm, 31.02 μm and 31.59 μm. Each grating had an aperture of 1 mm by 1 mm as shown in Figure 4-2. The end facets had specified parallelism within 5’ and anti-reflection (AR) coated reflectivity of < 1.5% at 1064 nm and < 1% at 1400-1800 nm. To implement temperature tuning and as an additional precaution against photorefractive damage, the crystal was mounted in an oven with a temperature controller tunable up to 200°C and a resolution of 0.1°C.

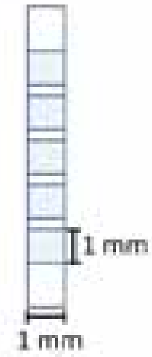

Figure 4-2 Illustration (front view) of the crystals used in the experiments: MgO-doped $LiNbO_3$ with five periodically poled gratings.

No cavity mirrors were required for the single-pass OPG. The separation of the signal and idler pulses at the output of the OPG is shown in Figure 4-1: A dichroic mirror (DM2), highly reflective for signal but highly transmissive at pump and idler wavelengths, was placed at the output of the crystal followed by a long-pass filter (LPF_s) (Thorlabs FEL1250) with a cut-off wavelength at 1250 nm to obtain the signal pulses. The idler pulses were then extracted through another long-pass filter (LPF_i) (Northumbria Optical Coatings LWP-4047-1-1-09) cutting off at 1950 nm, after the residual pump was filtered by a dichroic mirror (DM3).

Realisation of the OPA was implemented by injecting a seed signal through a dichroic mirror (DM1 in Figure 4-1) and focusing it into one of the periodically poled channels in the MgO:PPLN by the same lens that was used to focus the pump beam. The signal spot size was ~90 μm at the centre of the channel. Two seed lasers with different spectral bandwidths were used in the experiments for the investigation of their effects on the power extraction from the parametric amplification process as well as the associated spectral characteristics of the generated signal and idler pulses. One of the lasers was a commercial fibre-coupled continuous-wave (CW) external-cavity diode laser (Photonetics Tunics-Plus) that was tunable from 1480 to 1650 nm with a 3-dB spectral bandwidth of ~0.03 nm. The other one was a filtered ASE source built in-house with Er-doped-fibre amplifiers (EDFAs) and a bandwidth-variable tunable filter (Alnair-Labs

BVF-100). The centred wavelength of this source could be tuned from 1530 to 1570 nm with a 3-dB spectral bandwidth tunable from 0.1 to 10 nm. Figure 4-3 shows the output spectrum of the commercial laser at 1503.6 nm while Figure 4-4 is that of the filtered ASE source at 1541.3 nm with a 3-dB spectral bandwidth set to 0.3 nm. Both spectra were acquired by an optical spectrum analyser (OSA) (ANDO AQ6317B). The signal and idler pulses generated from the OPA were separated by the same method as for the OPG mentioned above.

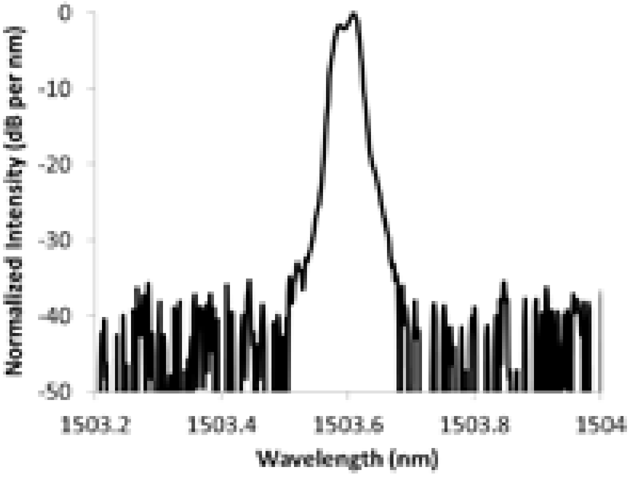

Figure 4-3 Spectrum (resolution = 0.01nm) of the signal from the seed laser with narrower linewidth used in the OPA experiment

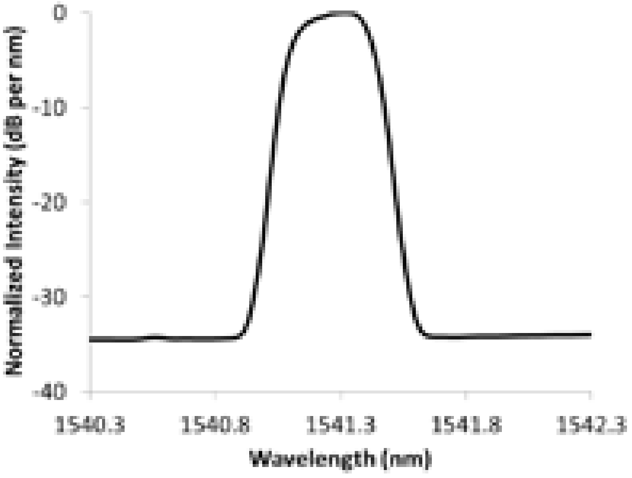

Figure 4-4 Spectrum (resolution = 0.1 nm) of the signal from the seed laser with broader linewidth used in the OPA experiment

The resonator of the OPO was constructed in a bow-tie ring cavity, formed by two curved mirrors (CM1 and CM2 in Figure 4-1, each with a radius of curvature of -250 mm) on both sides of the crystal and two plane mirrors (M3 and M4 in Figure 4-1) at the other corners of the arms. The ABCD matrix formalism [115] was used to calculate the separation of mirrors for a signal waist size of 90 μm and a repetition frequency of 200 MHz. Since generating high-energy idler pulses was the focus in this work, no output coupler was used in the resonator in order to minimise the signal cavity loss. Therefore, all the cavity mirrors in the set-up were coated to be highly reflective at the signal wavelengths but highly transmissive for the pump and idler. The final optical cavity length after alignment and optimisation was ~1.553m, i.e. a signal-resonating frequency of 193.1 MHz (192 times the pump repetition rate). On the other hand, the idler pulses were generated only when the signal pulses synchronised with the pump pulses and thus had the same repetition rate as that of the pump. Since there was no output coupling for the signal, the dichroic mirror DM2 and filter LPF_s in Figure 4-1 were not required for the characterisation of the OPO. Idler pulses were obtained through the dichroic mirror DM3 and filter LPF_i, as aforementioned.

4.3 Optical Parametric Generation

In the OPG experiment, the pump beam was focused to a waist of 77.5 μm at the centre of a periodically poled channel in the crystal by a lens with a focal length of 250 mm. The corresponding focusing parameter was $\xi_p = 0.502$, which implied that the pump beam was less tight than the confocal focusing condition; however, the priority in the experiment was given to the prevention of crystal damage rather than maximizing the conversion efficiency.

Spectral selection and tuning of the OPG were performed by utilizing different channels of the PPLN crystal as well as varying the oven temperature. Figure 4-5 shows a demonstration of the tuning capability with different gratings at a constant temperature of 91°C, allowing selection of the signal and idler centre wavelengths from 1479 to 1787 nm and 2455 to 3445 nm, respectively. Utilising the relevant Sellmeier equation [116], a tuning curve (black dashed line) was simulated for the 1034.5-nm-pumped MgO:PPLN-based OPG to show the expected signal and idler wavelengths from the corresponding quasi-phase-matched interactions (discussed in section 2.3.2) as a function of the grating period. It can be seen that the measured wavelengths agreed well with the locus of the simulated tuning curve. In addition, when tuning from 91°C to 150°C, the signal and idler wavelengths generated with the 29.5-μm grating period changed from 1479 nm to 1500 nm and 3445 nm to 3330 nm, respectively; thereby demonstrated the spectral-tuning dependency on temperature. (Results are not shown in the figure.)

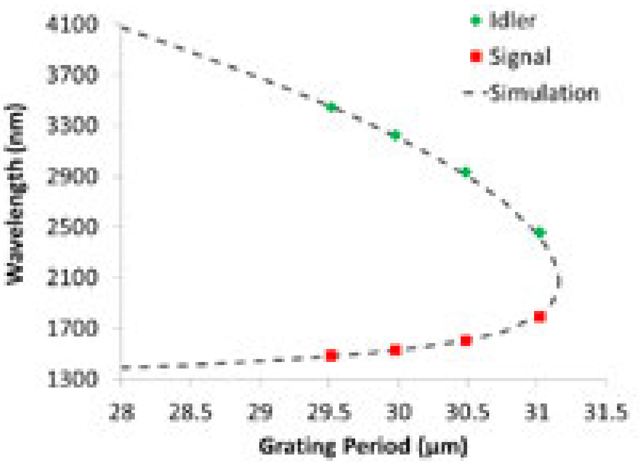

Figure 4-5 Selection of signal and idler wavelengths generated from the OPG by accessing different gratings of the MgO:PPLN at temperature of 91°C. The dashed curve is the simulated tuning curve.

Figure 4-6 plots the evolution of the signal and idler power generated from the OPG with the 29.5-μm channel against the pump power at the entrance of the crystal at an oven temperature of 150°C. The pump threshold was observed to be ~5 W, after which the signal and idler powers increased with slope efficiencies of 38% and 17.5%. The maximum extracted pulse energies were 2.7 μJ and 1.2 μJ respectively, corresponding to an overall parametric conversion efficiency of 32% with respect to the maximum available pump power of 12.2 W (i.e. pulse energy of 12.1 μJ). A beam quality of $M^2 \approx 3.2$ was measured for the signal beam with a beam profiler (Thorlabs BP209-IR) under the maximum operating condition. Another beam profiler (Ophir Photonics Nanoscan) which was sensitive in the MIR wavelengths was used to measure the M^2 of the idler beam and resulted in a value of ≈ 4.4. The relatively poor M^2 of both the signal and idler beams were expected; beam qualities at such levels had been previously reported in other OPGs [110].

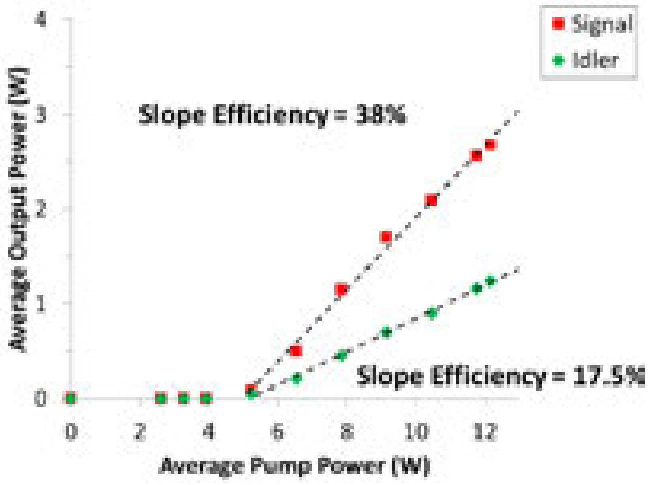

Figure 4-6 Average signal and idler output power versus pump power of the OPG, generated with 29.52-µm grating period at 150°C

The signal and idler spectra measured under this operating condition are shown in Figure 4-7 and Figure 4-8, respectively. The signal spectrum was measured with an OSA (ANDO AQ6317B) at a resolution of 0.1 nm while the idler spectrum was measured with another OSA (Bristol 721) at a resolution of 1 nm. It can be seen that the signal peak at 1500 nm had a 3-dB spectral bandwidth of 5.6 nm. The stimulated Raman scattering (SRS) spectral intensity peak at ~1510 nm lay at ~3.5 dB below the signal peak. The location of the SRS spectral intensity peak is consistent with the reported first-stoke Raman shift of 46 cm^{-1} in an MgO:PPLN [117]. The idler had a centre wavelength of 3330 nm with a 3-dB spectral bandwidth of 38 nm. Such broad signal and idler spectra are typical in OPGs [26,110,118]. However, in order to ensure that the measured spectral bandwidths were indeed reasonable under our experimental conditions, the measurements were compared to the calculations based on the existing theories of parametric gain analysis presented in section 2.3.3. The 3-dB gain bandwidths were calculated to be 2.6 nm and 12.7 nm for the signal and idler pulses, respectively, in the low-gain regime of the OPG with the focusing conditions used in the experiments. In addition, when employing the plane-wave model and taking into account high parametric gain, 3-dB gain bandwidths of 9.5 nm (signal) and 46.8 nm (idler) were obtained. Therefore it was believed that the measured bandwidths were consistent with the theoretical predictions.

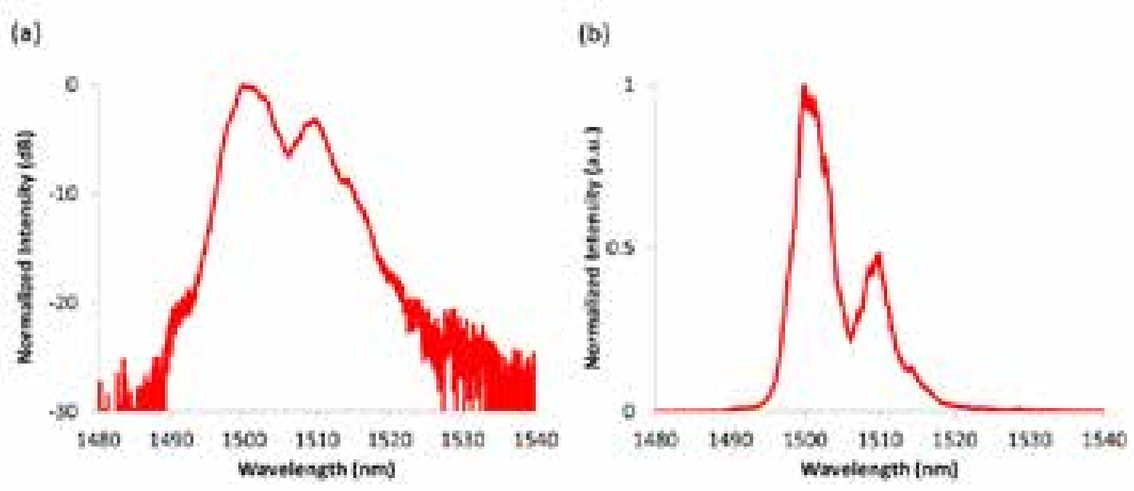

Figure 4-7 Spectrum (resolution = 0.1 nm) of the signal output from the OPG, generated with 29.52-μm grating period at 150°C. (a) Logarithmic scale and (b) linear scale.

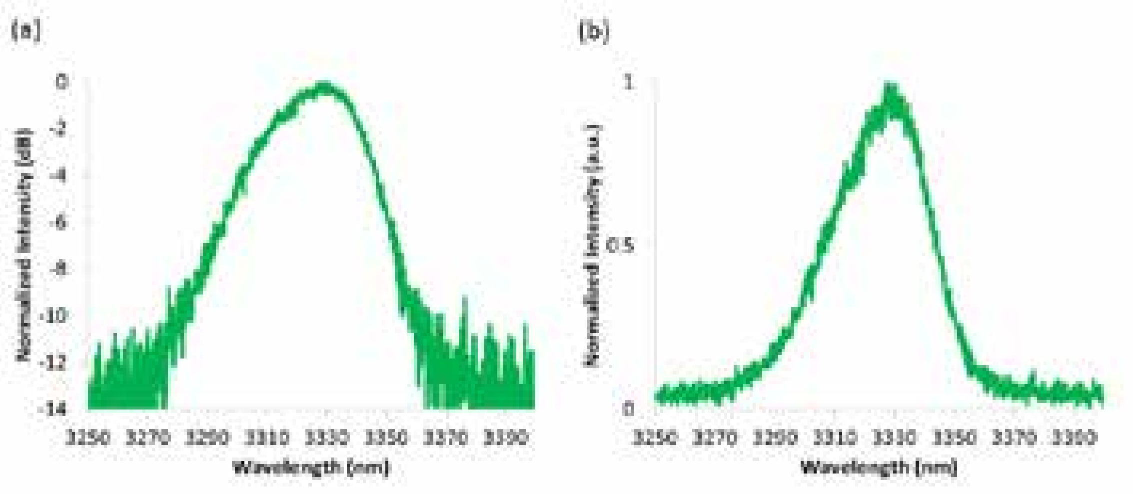

Figure 4-8 Spectrum (resolution = 1 nm) of the idler output from the OPG, generated with 29.52-μm grating period at 150°C. (a) Logarithmic scale and (b) linear scale.

The temporal profile of the signal pulses was measured with a 32-GHz-bandwidth photodetector (Agilent HP 83440D) and a 20-GHz-bandwidth digital communication analyser (Agilent 83480A). It should be noted that the full-width-at-half-maximum (FWHM) pulse duration measured before the electro-optic modulator (EOM) in the MOPA system was 120 ps, but a 145-ps duration was shown on the oscilloscope when measured after the EOM with a different triggering source. The slightly lengthened pulse width was believed to be an artefact due to a triggering problem. This triggering source was used for the measurement of all the temporal profiles presented in this chapter as there was no other accessible alternative source. However, this was not a detrimental issue since the focus of measuring the temporal profiles in the optical parametric experiments was the relative durations between the pump and the signal pulses. All the pulse durations mentioned in the rest of this chapter are the inferred actual pulse widths. Due to the temporal gain narrowing effect [110], the measured FWHM pulse duration of the signal was shorter than that of the pump pulse by 16% as shown in Figure 4-9. This corresponded to a FWHM duration of 104 ps for the signal pulse and a time-bandwidth product (TBP) of 77.1, which was more than 175 times of the transform-limit of a Gaussian pulse and thus indicated a strongly chirped signal pulse. The counterpart measurement of the idler pulses could not be performed as there was not any suitable photodetector or autocorrelator available at the time of the experiments. However, the idler pulse duration was expected to be similar to that of the signal and thus an estimated TBP of ~107, i.e. more than 240 times of the transform-limit of a Gaussian pulse. The maximum peak power attained by the signal was 25.5 kW whilst the pump peak power was 97.4 kW.

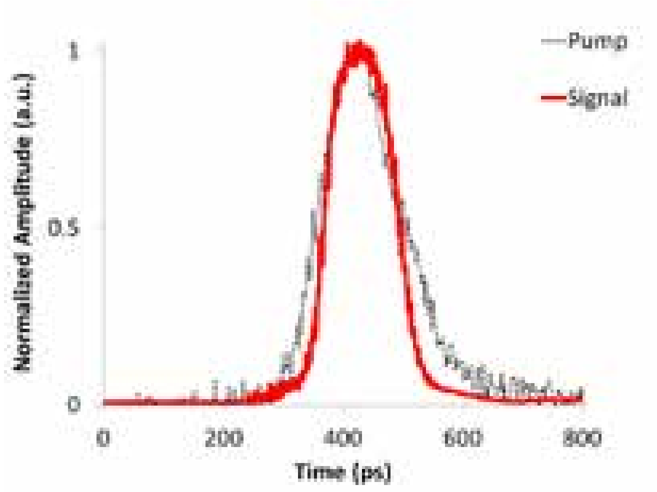

Figure 4-9 Temporal profile of the signal pulses from the OPG, generated with 29.52-µm grating period at 150°C. Measurement was performed with a 32-GHz-bandwidth photodetector.

From a practical perspective, the relatively broad spectral bandwidths of both the signal and idler pulses from the OPG presented in this section could limit its potential applications. However, this should not be a restraint on its applicability to RIR-PLD and RIR-PLA; for example, the infrared absorbance of the C-H stretch in polyethylene glycol (PEG) has a FWHM bandwidth of 81 nm [14], which is approximately twice that of the 3-dB idler spectral bandwidth. In addition, the tunability of the OPG covered the vibrational resonance of many important functional groups such as the C-H stretch (3.45 µm) and the O-H stretch (2.9 µm). On the other hand, the relatively poor M^2 of the idler beam could become a limiting factor when implementing the RIR-PLD/ RIR-PLA process.

4.4 Optical Parametric Amplification

An OPA with a narrow-linewidth signal seed was set up for the investigation of its effects on narrowing the signal and idler spectral bandwidths as well as suppressing the SRS growth in the signal spectrum that were observed in the OPG in section 4.3. The pump focusing parameter used in the experiments presented in this section stayed the same as that in the OPG experiments.

4.4.1 Thirty-Picometre Seeding Bandwidth

Signal seed with a 3-dB spectral bandwidth of 0.03 nm and an M^2 of ≈ 1 were provided from the tunable (1480 to 1650 nm) Photonetics Tunics-Plus fibre-coupled CW external-cavity diode laser described in section 4.2. The beam was launched into the 29.5-µm-period gratings in the MgO:PPLN crystal such that a waist of 90 µm was focused at the centre of the channel to approximately match the pump waist.

Figure 4-10 is an example of the saturation behavior of the OPA average output power as a function of the seeding power. The measurement was carried out at an oven temperature of 150°C, pump power of 8.5 W, and with the seed laser emitting at 1504 nm. It can be seen that the signal output power turned towards saturation at a seed power of only 0.5 mW. Further increasing the seeding power to 5 mW settled the OPA in the saturation regime, reaching an average output power of 2.8 W.

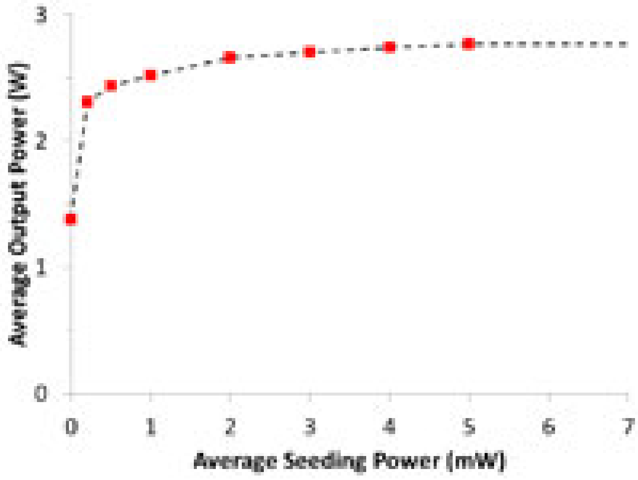

Figure 4-10 Average output power of the signal versus the seeding power of the OPA at 150°C

With the seed operated at 1504 nm and an average power of 5 mW, the signal and idler power generated from the OPA at 150°C was measured and plotted against the input pump power as shown in Figure 4-11. It was observed that the pump threshold had been reduced to 2.2 W from the 5-W threshold in the OPG presented in section 4.3. The slope efficiencies of the signal and idler power scaling were 45.7% and 17%, respectively. Maximum pulse energies of 3.2 μJ (signal) and 1.3 μJ (idler) were reached before an abrupt significant drop in output power to $\lesssim$ 100 mW accompanied by an enormous emission of visible light from within the crystal, when the average pump power was increased beyond ~10.5 W. Adjusting the positions of the pump and signal waists in the same grating only recovered the output power to ~77% and it was concluded that the grating was damaged. At the maximum operating condition, the signal M^2 was measured to be ≈ 2.1 with the same beam profiler used for the signal in the OPG experiment. The improvement of M^2 compared to that from the OPG was believed to be caused by signal growth from a good-quality seed rather than parametric noise. The idler M^2 was not measured as the beam profiler for the MIR wavelengths was not accessible at the time of this experiment. However, enhancement of M^2 in both signal and idler beams by signal seeding has been reported before [110].

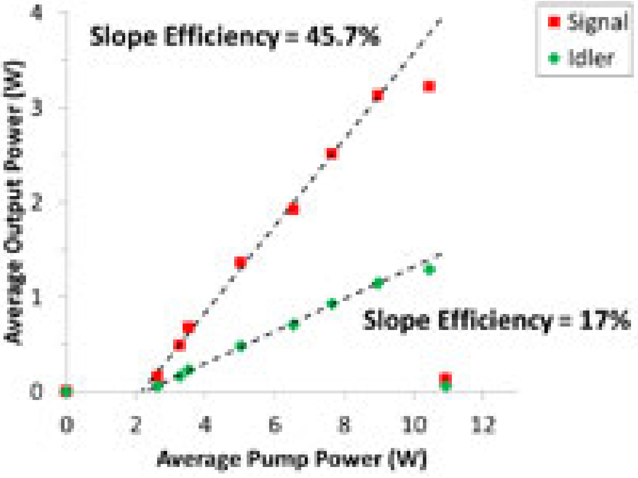

Figure 4-11 Average signal and idler output power versus pump power of the OPA, generated with 29.52-μm grating period at 150°C and a seeding laser with a 3-dB spectral bandwidth of 0.03 nm

The spectra of the signal and idler pulses measured at the maximum power before the damage of the crystal are shown in Figure 4-12 and Figure 4-13, respectively. The spectra were measured with the same OSAs used for the counterpart measurements in the OPG experiments. Comparing to the signal generated from the OPG, the 3-dB spectral bandwidth of the signal in the OPA was narrowed by ~100 times to 0.06 nm (at OSA resolution of 0.01 nm), which was approximately twice that of the seeding signal. Moreover, the SRS spectral intensity peak was greatly suppressed to 38 dB below the signal peak since the signal bandwidth was not broad enough to seed the growth of the SRS. The idler pulses centred at 3319 nm had a 3-dB spectral bandwidth of 6.7 nm, which was approximately 6 times narrower than that generated from the OPG. This was expected since the frequency bandwidth was practically a direct transfer from the pump (0.168 THz) to the idler (0.182 THz) with a much narrower signal spectrum [119].

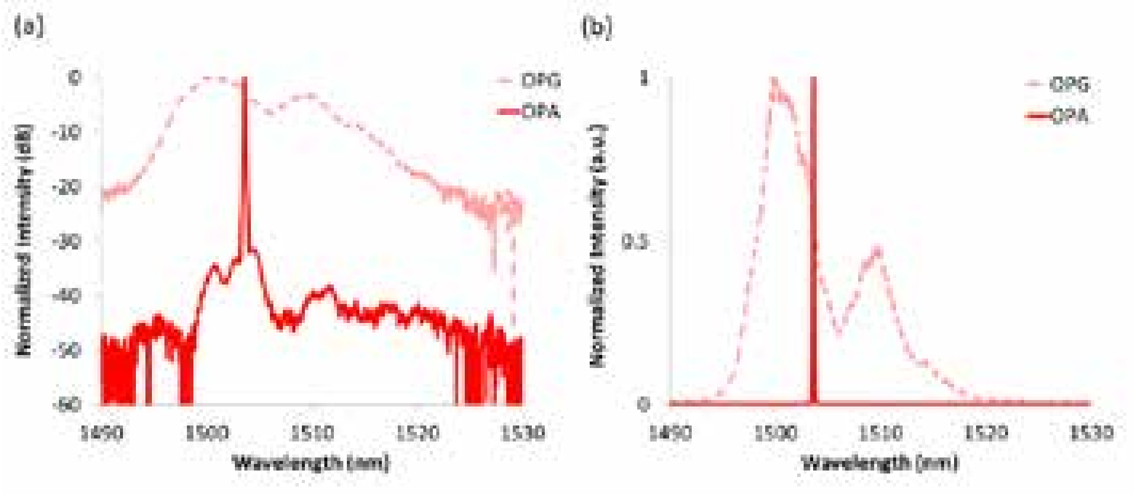

Figure 4-12 Spectrum (resolution = 0.1 nm) of the signal output from the OPA, generated with 29.52-µm grating period at 150°C and a seeding laser with a 3-dB spectral bandwidth of 0.03 nm. Corresponding OPG spectrum is included for reference. (a) Logarithmic scale and (b) linear scale.

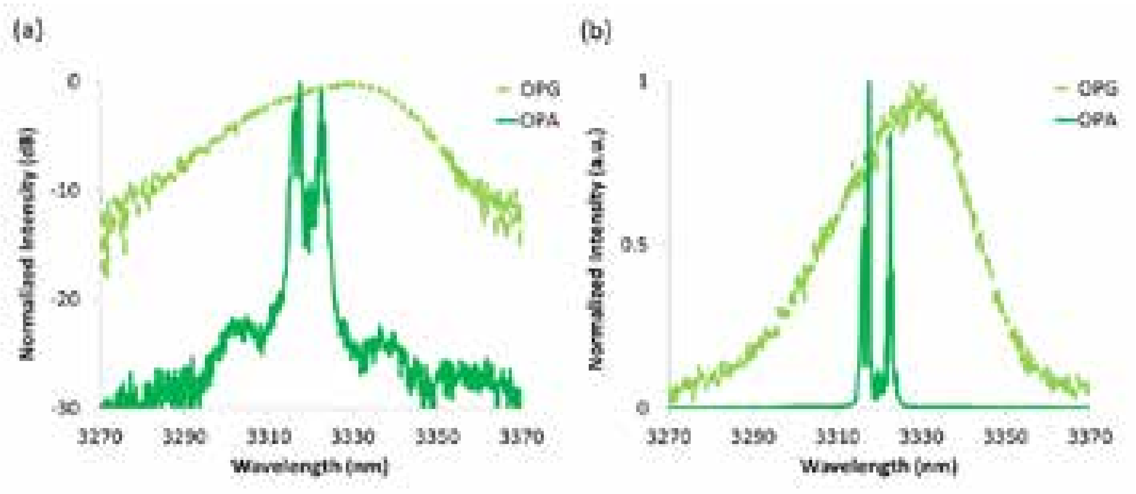

Figure 4-13 Spectrum (resolution = 1 nm) of the idler output from the OPA, generated with 29.52-µm grating period at 150°C and a seeding laser with a 3-dB spectral bandwidth of 0.03 nm. Corresponding OPG spectrum is included for reference. (a) Logarithmic scale and (b) linear scale.

The temporal profile of the amplified signal (Figure 4-14) was measured in the same way as in the OPG experiment. The FWHM pulse duration was~3.3% shorter than that of the pump pulse but ~15% longer than that of the signal pulse generated from the OPG as a result of the saturated gain in the OPA operation. The pulse duration of 120 ps implied a TBP of 0.955, which was 2.17 times of the transform-limit of a Gaussian pulse. The pulse duration of the idler was not measured as explained in section 4.3 but the TBP was estimated to be ~22, assuming a pulse width similar to that of the signal. It can be seen that the TBPs of the signal and idler could be greatly improved when operating the system as an OPA rather than an OPG. In the experiments, the signal and idler TBPs were 80.6 times and 4.8 times smaller in the OPA, respectively.

Before the crystal was damaged, the maximum peak power attained by the amplified signal was 26.7 kW while the pump peak power was 83.8 kW, which corresponded to a peak intensity of 0.89 GW/cm^2. However, the pump peak intensity was lower than that in the OPG where no damage to the crystal was observed. While the reasons for the damage were unknown, there was a noticeable increase in the intensity of visible light generated in the OPA compared to that in the OPG, which may be related to the damage. Furthermore, the peak intensities of the pump beams in both the OPG and OPA were in the regime where self-focusing in PPLN could occur [120], but seeding the OPA with a narrow bandwidth might have decreased the self-focusing threshold [121]. It was thus speculated that seeding with a broader bandwidth may increase the maximum extractable pulse energies from the OPA; such experiments are presented in the next section.

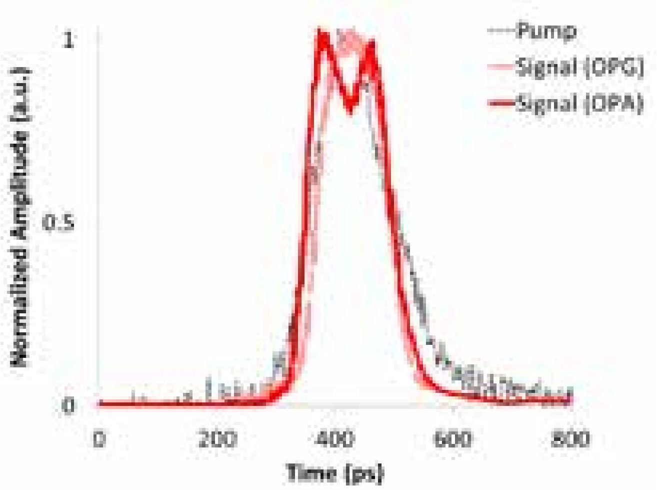

Figure 4-14 Temporal profile of the signal output from the OPA, generated with 29.52-μm grating period at 150°C. Measurement was performed with a 32-GHz-bandwidth photodetector.

4.4.2 Sub-Nanometre Seeding Bandwidth

The damaged crystal was then replaced by a new MgO:PPLN crystal of the same model and the OPA in section 4.4.1 was reconstructed again to ensure similar parametric scaling was generated. The in-house-built filtered ASE source described in section 4.2 was set to deliver a seeding signal at 1541 nm with a 3-dB spectral bandwidth of 0.3 nm, i.e. 10 times broader than the seed laser used in the OPA in section 4.4.1. The output power from the seed was 29 mW, which was believed to be considerably higher than required to saturate the OPA output power based on the experimental results (Figure 4-10) discussed earlier. However, this power was not attenuated before launching into the MgO:PPLN crystal in order to ensure the alignment of the seeding beam was the same for the two OPAs. Seed spot size was 90 µm at the centre of the crystal.

Figure 4-15 plots the measured average signal and idler output powers generated with the 30-µm-period grating at 110°C. Unlike the OPA in section 4.4.1, no damage to the crystal was observed when the pump power was increased beyond 10.5 W in this OPA. The resulting pump threshold was 2.7 W and the slope efficiencies of the signal and idler were 40.5% and 18%, respectively. At the maximum available pump power, the extracted pulse energies were 3.8 µJ (signal) and 1.7 µJ (idler), corresponding to an overall parametric conversion efficiency of 45.6%. At this operating point, the 3-dB spectral bandwidth of the signal was measured to be 0.33 nm (Figure 4-16), which was about the same as that of the seed as expected. The idler was centred at 3147 nm with a 3-dB spectral bandwidth of 8.6 nm (Figure 4-17), i.e. 0.26 THz, whereas the pump bandwidth was 0.22 THz in this experiment.

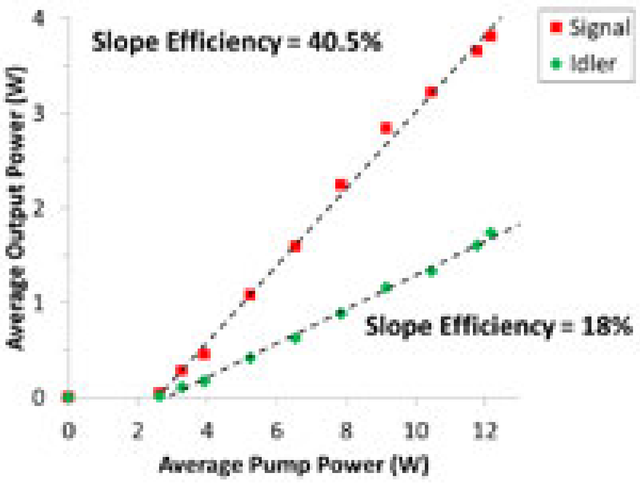

Figure 4-15 Average signal and idler output power versus pump power of the OPA, generated with 29.98-µm grating period at 110°C and a seeding laser with a 3-dB spectral bandwidth of 0.3 nm

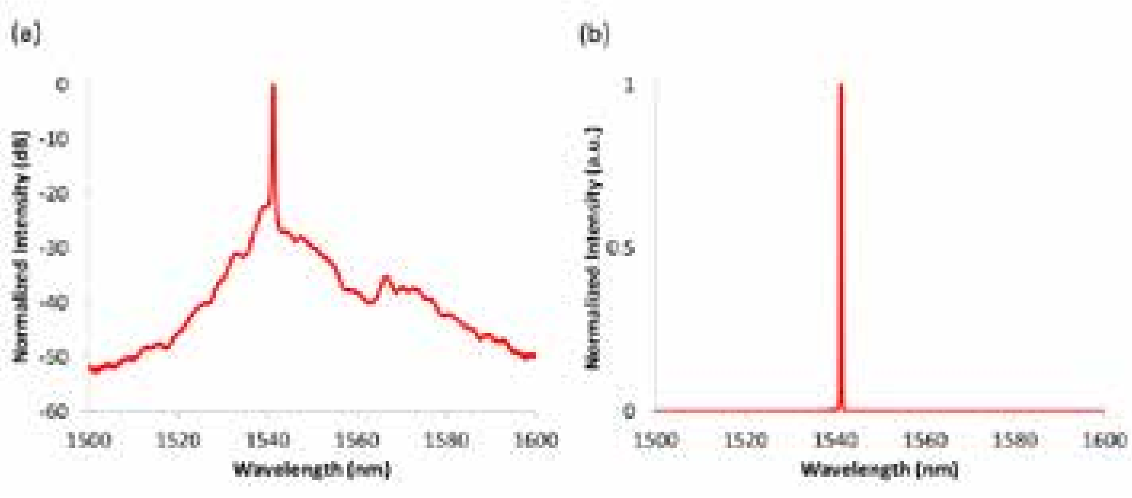

Figure 4-16 Spectrum (resolution = 0.1 nm) of the signal output from the OPA, generated with 29.98-µm grating period at 110°C and a seeding laser with a 3-dB spectral bandwidth of 0.3 nm. (a) Logarithmic scale and (b) linear scale.

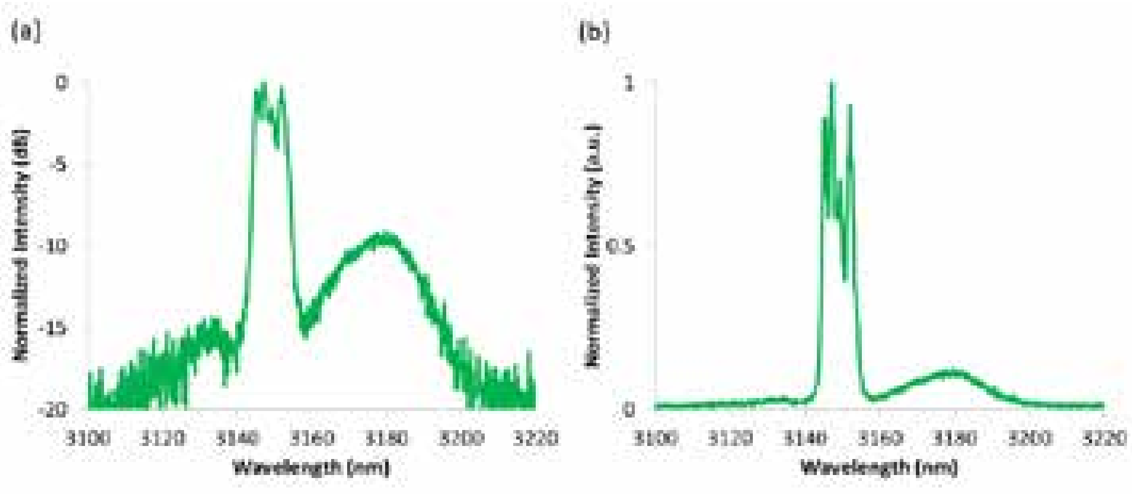

Figure 4-17 Spectrum (resolution = 1 nm) of the idler output from the OPA, generated with 29.98-µm grating period at 110°C and a seeding laser with a 3-dB spectral bandwidth of 0.3 nm. (a) Logarithmic scale and (b) linear scale.

With respect to its applicability, the OPA discussed above had been demonstrated with 3-dB idler spectral bandwidths that were ~10 times narrower than that of the C-H stretch absorbance involved in RIR-PLD and RIR-PLA of materials such as PEG. Moreover, the M^2 of the idler beam was expected to be better than that from the OPG presented in section 4.3, thus relieving the difficulty of implementing the RIR-PLD/ RIR-PLA process. However, the tunability of the OPA depended heavily on that of the seed source, and this could be a limiting factor for such applications. For instance, signal seed at ~1478 nm would be required for generating an idler to match the vibrational resonance of the C-H stretch, but the source with 3-dB spectral bandwidth of 0.3 nm used to avoid crystal damage at full pump power was not capable of providing such wavelengths.

4.5 Optical Parametric Oscillation

As shown in sections 4.3 and 4.4, the OPG had a simple single-pass configuration, but the idler pulses had bandwidths of several tens of nanometres and an M^2 of ≈ 4.4. The OPA configuration reduced the bandwidth to as narrow as 6.7 nm and slightly improved the M^2, but the tuning range was limited by that of the signal seed. Therefore, there was an interest to also construct an OPO to explore its performance compared to the OPG and OPA. The OPO discussed in this section employed a cavity length equal to an exact fraction of that required for a conventional synchronously pumped OPO (SPOPO) to avoid a long cavity length that would be required otherwise for pumping at the 1-MHz repetition rate. The schematic of the cavity and the measurement optics has been shown in Figure 4-1 in section 4.2, and is re-drawn below (Figure 4-18) for reference.

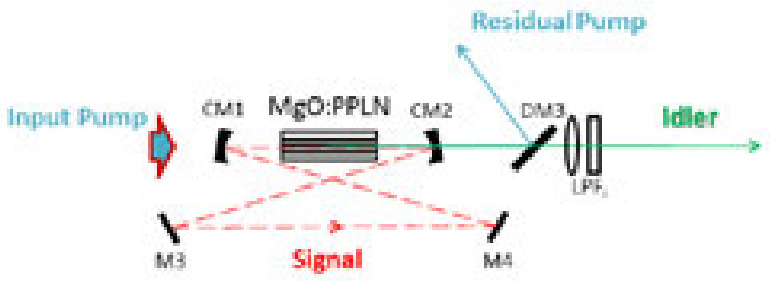

Figure 4-18 Set-up of the OPO cavity and measurement optics. DM = dichroic mirror, CM = curved mirror, M = plane mirror, LPF = long-pass filter.

The initial set-up of the resonator was based on the cavity dimensions calculated for a waist radius of 90 µm in a harmonic cavity of ~200-MHz repetition rate operating below the damage threshold of the crystal. This corresponded to a focusing parameter of 0.590 and a cavity length of ~1.5 m. To match the pump to the signal waist size at the centre of the crystal, the pump was focused to a waist of 87.5 µm, corresponding to a focusing parameter of 0.397. Both the pump and signal beams were not focused as tight as the confocal focusing condition; however, this was again accepted in favour of reducing the risk of damaging the crystal as opposed to maximising the conversion efficiency. Optimisation of the alignment was then carried out experimentally using the 30-µm-period PPLN grating at a temperature of 100°C. Figure 4-19 shows the signal pulse train measured from the leakage through the OPO plane mirror M3 (Figure 4-18) with a 1-GHz-bandwidth photodetector (OSI) and a 1-GHz-bandwidth digital oscilloscope (Agilent InfiniiVision MSO7104) The time between two spikes was 5.18 ns, indicating that the signal-resonating frequency was 193.1 MHz; this corresponded to an optical cavity length of 1.553 m. Furthermore, due to intracavity losses from an AR-coated facet of the crystal and four cavity mirrors, the signal pulse intensity decreased with time until the next pump pulse arrived. A round-trip loss of 5% was estimated by fitting the peaks of the normalised pulse train to the equation $I = (1-\alpha)^N$ where α is the intracavity round-trip loss and N is the number of round trips. The accumulated loss between each synchronisation of the signal and pump pulses, was thus estimated to be ~43 dB.

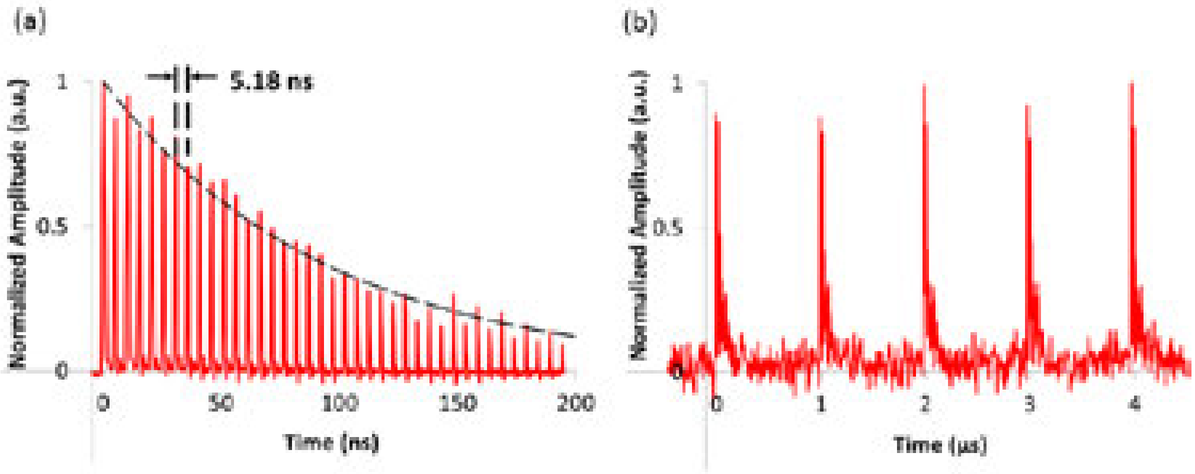

Figure 4-19 Pulse train of the signal resonating in the OPO cavity, generated with 29.98-μm grating period at 100°C. Measurement was performed with a 1-GHz-bandwidth photodetector. Figure in (a) and (b) show the same pulse train in different time scale.

The power, M^2 and spectra of the idler generated from the OPO were measured as in the OPG and OPA experiments in sections 4.3 and 4.4. The OPO started to oscillate at an average pump power of 2.9W incident on the PPLN crystal. It was observed in the OPA experiments that the seeding signal with an average power of 0.2 mW was amplified to 2.3 W with a pump power of 8.5 W (Figure 4-10 in section 4.4.1). This corresponded to a small-signal effective gain of 80 dB within the 120-ps signal pulse duration. Therefore, the observed pump threshold and the calculated intracavity loss of the OPO were believed to be in reasonable agreement with the gain available from such systems. Considering the power external to the cavity (Figure 4-20), the idler output power started to increase at an average pump threshold of 3.2 W, with a slope efficiency of 17.3% leading to a maximum extracted pulse energy of 1.5 μJ after the mirror CM2. Inside the cavity, the idler power scaled up at a slope efficiency of 22.6%, reaching pulse energies of 1.8 μJ at the maximum pump power of 10.9 W. This corresponded to a conversion efficiency of 16.6% and an overall parametric conversion efficiency of 51.2% with the idler generated at 3191 nm. Figure 4-21 is the corresponding spectrum, showing a 3-dB spectral bandwidth of 6.5 nm. The measured beam caustic is plotted in

Figure 4-22, leading to an M^2 of ≈ 2.4 on the horizontal plane (parallel to the resonator plane) and ≈ 1.9 on the vertical plane (normal to the resonator plane). The asymmetric M^2 on the two planes could be caused by factors such as the asymmetric beam waist arisen from the astigmatism due to the tilted curved mirrors (CM1 and CM2 in Figure 4-18) on the horizontal plane. It should be noted that the measured idler M^2 was about half of that from the OPG. It was also approximately the same as the signal M^2 from the OPA, for which idler M^2 measurements were not taken but can be expected to be inferior to the amplified signal.

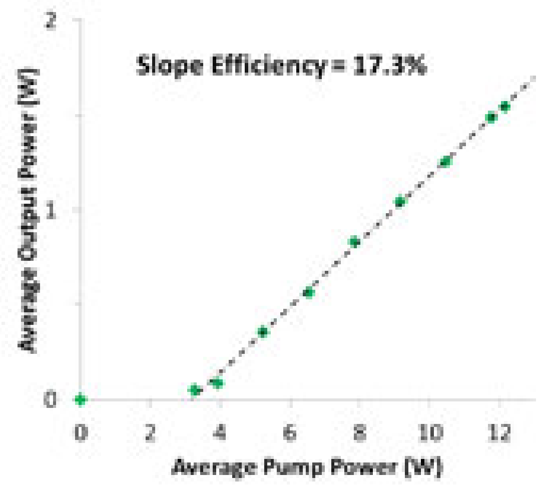

Figure 4-20 Average idler output power versus pump power of the OPO, generated with 29.98-µm grating period at 100°C

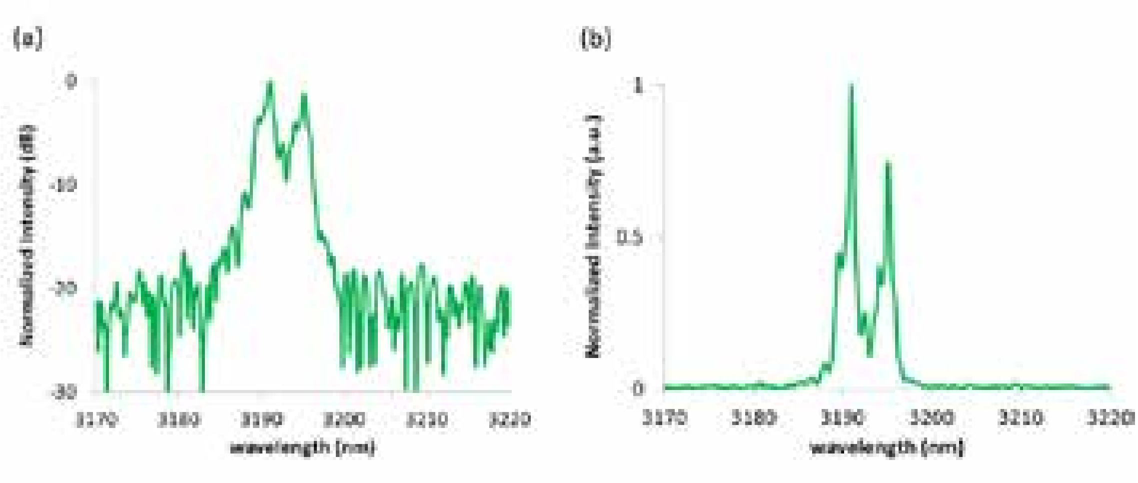

Figure 4-21 Spectrum (resolution = 1 nm) of the idler output from the OPO, generated with 29.98-μm grating period at 100°C. (a) Logarithmic scale and (b) linear scale.

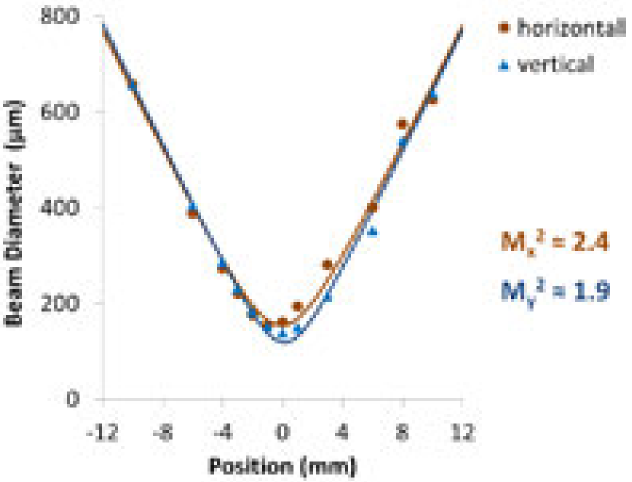

Figure 4-22 Beam caustic and curve fitting for M^2 measurement of the idler beam from the OPO described in text

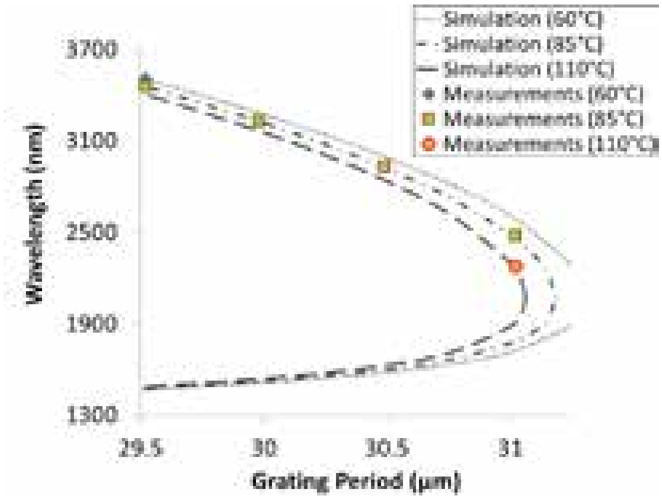

Figure 4-23 Tuning of idler wavelengths generated from the OPO by accessing different gratings of the MgO:PPLN and adjusting the oven temperature. The dashed curves are the simulated tuning curves.

Tuning of the idler centre wavelengths from 2276 nm to 3504 nm was demonstrated by accessing different gratings of the crystal as well as changing the oven temperature. This is illustrated in Figure 4-23, which shows that the experimental measurements agreed with the loci of the simulated spectral tuning curves (black dashed and dotted lines) which utilised the Sellmeier equation for MgO:PPLN [116] under the same conditions used in the experiments.

The characteristics of cavity-length detuning was also explored with the OPO by adjusting the distance between the plane mirrors M4 and M3 (Figure 4-18). When tuning the cavity length in steps of 0.5 mm over about 28 mm, four cycles of idler power oscillation were observed. This oscillation corresponded to the shift of the resonating frequency to different harmonic synchronisation as illustrated in Figure 4-24. The minimum output power did not fall to zero between the peaks since there was power generated from the optical-parametric-generation process even when the OPO ceased synchronous oscillation. Furthermore, detuning in finer steps of 20 μm revealed that the OPO could be sustained over a total detuning length of ~1.2 mm (green curve in Figure 4-25).

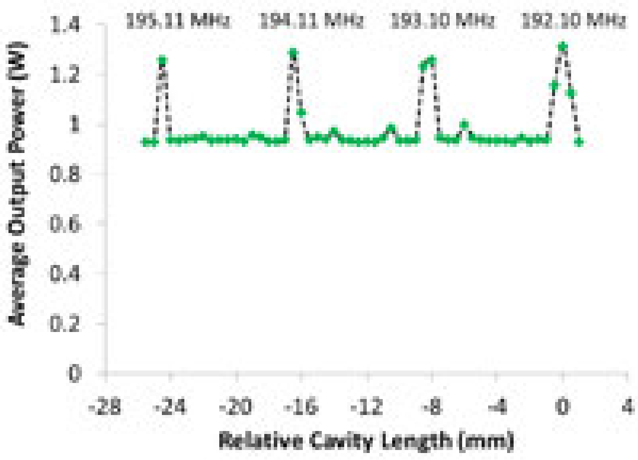

Figure 4-24 Average output power of the idler versus coarse cavity-length detuning in steps of 0.5 mm. 29.98-µm grating period were used for the OPO at 100°C

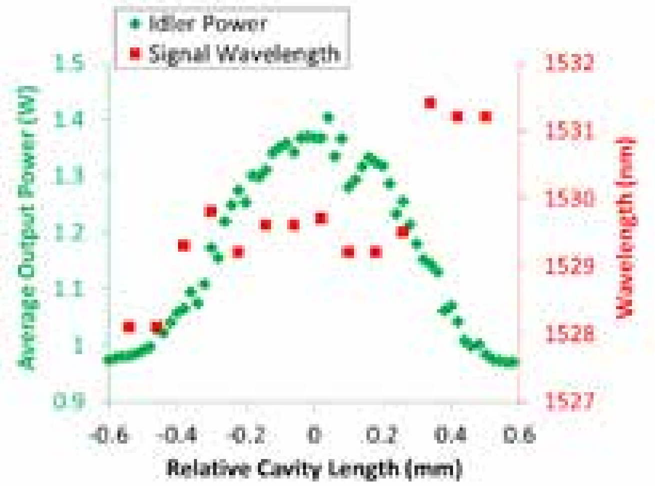

Figure 4-25 Average idler output power versus fine cavity-length detuning in steps of 20 µm (Green), and change in signal wavelength with detuning (Red). 29.98-µm grating period were used for the OPO at 100°C

It is well known that the signal wavelength can be tuned by adjusting the cavity length of an OPO [122,123]. Cavity-detuning reduces the synchronism between the pump and signal pulses and thus introduces losses at the signal wavelength, which then shifts within the gain bandwidth of the system towards a wavelength with a group velocity that satisfies the new round-trip time to optimise the synchronism and parametric gain. Figure 4-25 plots the shift in wavelength of the 193.1-MHz resonating signal measured from the leakage through the OPO plane mirror M3 (Figure 4-18) with an OSA (ANDO AQ6317B), while operating the OPO with the 30-µm-period grating at 100°C. It can be seen that the wavelength decreased with cavity length, resulting in a total shift of 3 nm from ~1531 nm to ~1528 nm over the entire cavity detuning-length of the OPO. The decrease in wavelength as the cavity became smaller was expected since the signal was residing in the normal-dispersion regime of the PPLN as shown in Figure 4-26. Furthermore, 3-dB gain bandwidths calculated based on the parametric gain models described in equation (2.24) and equation (2.23) were 2.9 nm and 9.9 nm, respectively. Therefore the measured shift in signal wavelength was within this expected regime.

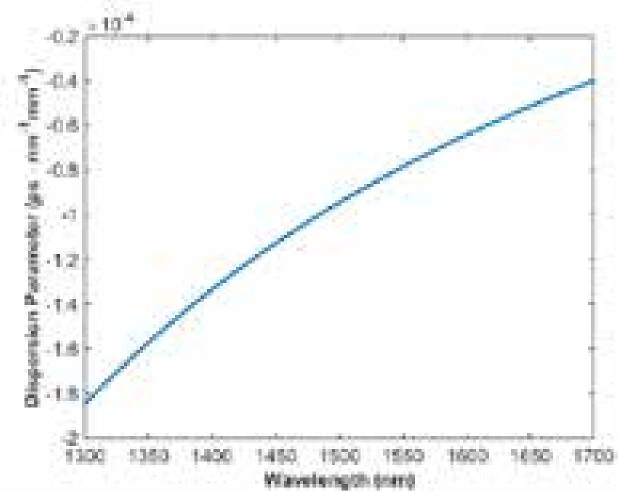

Figure 4-26 Dispersion around the signal wavelengths in the PPLN crystal under the operating conditions described in text. (Calculated from the Sellmeier equation [116])

The time delay between the waves at1528 nm and 1531 nm due to dispersion of the 40-mm-long PPLN was calculated to be 10.2 fs which accumulated to 1.96 ps after 192 round trips in the OPO cavity. However, a FWHM cavity-detuning length of 600 μm for the 193.1-MHz cavity corresponded to a time delay of 384 ps between the signal pulse and the next pump pulse, which had a FWHM pulse width of 124 ps. Therefore the time delay due to the dispersion of the signal was not sufficient to compensate for the cavity-detuning even after taking into account a 4.3-ps time delay between the pump and signal in one pass through the PPLN. This discrepancy was not further investigated due to time constraint of the project, but possible mechanisms involved in this phenomenon include high-gain-induced detuning tolerance and self-adaptation of the resonant beam path within the cavity to maintain a constant round-trip time. Such a geometrical adaptation has been reported before but with a diffraction grating in the cavity[124].

It should be noted that there was no output coupling for the signal pulses from the harmonic cavity and thus only the idler pulses could be used. However, this did not affect the suitability of this OPO as a source for RIR-PLD and RIR-PLA. For example, the idler spectral bandwidth was 12.5 times narrower than that of the PEG C-H stretch absorbance. Moreover, in terms of the beam quality, the idler M^2 was approximately the same as that of the signal in the OPA discussed in section 4.4, and is thus assumed to be better than that of the OPA idler. In addition, idler tunability of more than 1200 nm was demonstrated with a coverage of the vibrational resonance of many important functional groups in polymers such as PEG and polystyrene (PS).

4.6 Summary

This chapter has presented the use of various parametric processes to generate microjoule MIR picosecond pulses at 1-MHz repetition rate, targeting applications such as RIR-PLD and RIR-PLA. A GSD-seeded MOPA employing simple direct amplification in a nearly all-fiberised configuration was employed to provide high-energy pump pulses for three optical parametric devices in relatively simple setups— OPG, OPA and harmonic-cavity OPO. Their performance was investigated and compared.

The OPG had a simple single-pass configuration and was demonstrated with a tunability of 1479-1787 nm (signal) and 2455-3445 nm (idler). The generated signal and idler pulse energies increased with slope efficiencies of 38% and 17.5%, reaching 2.7 μJ and 1.2 μJ, respectively. However, their TBPs were 77.1 (signal) and 107 (idler) as a result of their very broad 3-dB spectral bandwidths. In addition, the M^2 were measured to be ≈ 3.2 and ≈ 4.4 for the signal and idler, respectively. The relatively poor M^2 would cause practical difficulties when implementing RIR-PLD, although the idler spectral bandwidth and tunability were adequate for such processing of materials including PEG and PS.

The 3-dB spectral bandwidths of the signal and idler were significantly narrowed from 5.6 nm to 0.06 nm and from 38 nm to 6.7 nm when injecting a seeding signal with a 3-dB spectral bandwidth of 0.03 nm to realise an OPA. In addition, the TBP of the signal was improved to only twice of the transform limit of a Gaussian pulse, and the TBP of the idler was estimated to be a factor of ~5 better compared to the OPG. Also, the M^2 of the signal was improved to be ≈ 2.1. Unfortunately, idler M^2 measurement was not performed due to lack of a suitable camera at the time, but the M^2 can be expected to be greater than that of the signal. Effective gain of as high as 80 dB was observed from the OPA. However, possibly due to self-focusing, the crystal was damaged when the energies reached to 3.2 μJ (signal) and 1.3 μJ (idler). Seeding the OPA with a broader 3-dB spectral bandwidth of 0.3 nm increased the maximum extractable signal and idler pulse energies to 3.8 μJ and 1.7 μJ without damaging the crystal at maximum available pump power, corresponding to an overall conversion efficiency of 45.6%. Slope efficiencies of 40.5% and 18% were observed for the signal and idler, respectively.With a broader seeding bandwidth, the 3-dB spectral bandwidths increased to 0.33 nm (signal) and 8.6 nm (idler), but they are still significantly narrower than those from the OPG. With a narrow spectral bandwidth and an expected idler M^2 better than that of the OPG, the OPA could be a potential candidate as an MIR source for RIR-PLD/ RIR-PLA. However, the tuning range of the OPA significantly relied on the tunability of the signal seed, which could become a limiting factor for such applications.

The harmonic-cavity OPO employed a cavity length of 192 times shorter than that required for a conventional SPOPO pumped at 1-MHz repetition rate. External to the cavity, the slope efficiency of the idler generation was 17.3%, reaching a maximum idler pulse energy of 1.5 μJ, which was 10% less than that from the OPA. Inside the cavity, the idler power scaled up at a slope efficiency of 22.6%; pulse energy of 1.8 μJ was generated at the maximum pump power, corresponding to a conversion efficiency of 16.6% for the idler. The overall parametric conversion efficiency from pump to signal and idler was 51.2%. The spectral bandwidth of the idler pulses was in the same order as that from the OPA. Moreover, the idler M^2 was measured to be ~2, which was equivalent to that found for the signal in the OPA and was consequently assumed to be better than that for the OPA idler. Tuning of the idler wavelengths from 2276 nm to 3504 nm was demonstrated by accessing different gratings of the crystal at various temperatures. Cavity-length detuning was explored and a shift of 3 nm in the signal wavelength was observed with the detuning before oscillation ceased. An obvious drawback of this OPO was that there was no output coupling for the signal power and thereby imposing a restriction on its range of applicability. However, this does not limit its application towards an alternative source for RIR-PLD and RIR-PLA since the spectral bandwidth, M^2 and tunability were all expected to be suitable for such processing of materials including PEG and PS.

Table 4-1 compares the performance of the demonstrated parametric devices in terms of the pulse energies, tunability, spectral bandwidths and beam quality of the generated signal and idler outputs.

Table 4-1 Key attributes of the signal and idler outputs from the parametric devices presented in this chapter

	OPG		***OPA***		***Harmonic-Cavity OPO***	
	Signal	*Idler*	*Signal*	*Idler*	*Signal*	*Idler*
Pulse Energy	2.7 μJ	1.2 μJ	3.8 μJ	1.7 μJ	/	1.5 μJ
Tunability	1479-1787 nm	2455-3445 nm	/	/	/	2276-3504 nm
Bandwidth (3-dB)	5.6 nm	38 nm	0.33 nm	8.6 nm	/	6.5 nm
M^2	3.2	4.4	~2	/	/	~2

Chapter 5

Fibre-Feedback Picosecond OPO: High-Energy Near- and Mid-Infrared Generation and Nonlinear Phenomena

5.1 Introduction

The gain-switched-diode (GSD)-seeded Yb^{3+}-doped-fibre (YDF) master-oscillator power amplifier (MOPA) system presented in Chapter 3 was designed to be a robust and compact high-energy pump source for optical parametric processes targeting MIR pulses in ~2.5-4 μm for resonant infrared pulsed-laser deposition (RIR-PLD) and ablation (RIR-PLA) of organic materials. Pumped by this near-infrared (NIR) MOPA, three different devices with relatively simple configurations were demonstrated to generate microjoule, picosecond pulses at MHz repetition rates, as discussed in Chapter 4. They were an optical parametric generator (OPG), an optical parametric amplifier (OPA) and a harmonic-cavity optical parametric oscillator (OPO). With respect to the suitability for RIR-PLD/ RIR-PLA of materials such as polyethylene glycol (PEG) and polystyrene (PS), the simple single-pass OPG was demonstrated to have adequate idler spectral bandwidth and tunability, but the relatively poor M^2 would limit the focused spot sizes achievable in a PLD chamber and hence cause practical difficulties for implementation. On the other hand, the signal-seeded OPA provided better M^2 and narrower spectral bandwidths, but the tunability was limited by that of the seed source, complicating any proposed application. Finally, the harmonic-cavity OPO, although more complex, generated idler pulses with suitable spectral bandwidth, M^2 and tunability. However, a major inherent disadvantage of this configuration was that the whole range of parametrically generated signal output could not be extracted due to lack of an output coupler in its cavity. While this is not an impediment to application in RIR-PLD/ RIR-PLA, the lack of a signal output would limit some potential applications. For instance, inscription of waveguides in materials such as silicon and germanium require pulses at wavelengths above 1060 nm in the NIR region with MHz repetition rates and pulse energies of ~1 μJ [29].

Other ultrashort-pulse OPOs have been realized by employing techniques including cavity dumping [28], relay imaging [29] and fibre-feedback cavities [27] to generate high-energy signal and idler pulses at repetition rates of less than tens of MHz. The highest pulse energies reported among these systems were 0.65 μJ (signal) in sub-picosecond pulses at a repetition rate of 0.1 MHz [28] and 0.19 μJ (idler) in 100-ps pulses at repetition rate of 7.19 MHz [27], limited by their corresponding pump power.

Furthermore, the cavity dumping and relay imaging approaches require additional components such as an acousto-optic modulator for the former and an array of mirrors for the latter; thus introducing additional complexities to the implementation and difficulties to the minimisation of the footprint of the OPOs. In contrast, although the fibre-feedback configuration also requires an additional component (i.e. the feedback fibre), the resultant cavity can be more compact and simpler than the first two approaches since most of the optical cavity length could be constructed with a fibre that can be coiled.

Consequently, there has been an interest to build a fibre-feedback picosecond OPO to generate high-energy signal pulses that could be utilised outside the cavity, in addition to microjoule idler pulses that could be used for RIR-PLD/ RIR-PLA. It should be noted that the MIR pulse energies from the fibre-feedback OPO in [27] was less than 20% of what would be required for RIR-PLD/ RIR-PLA applications; thus further energy scaling was necessary. Moreover, elimination of components such as polarisation controllers, circulators and chirped fibre Bragg grating in the pump source would further simplify its configuration as discussed in section 3.1. Clearly, the implementation of such high-energy OPO would greatly benefit from the use of a compact high-energy MHz MOPA such as the one presented in Chapter 3, which therefore was employed again as the pump source for the fibre-feedback OPO discussed here. It provided 124-ps pump pulses centred at 1034.5 nm with pulse energy of more than 17 μJ at 1-MHz repetition rate. It should also be noted that such high pulse energies have not been reported before for pumping a fibre-feedback OPO; therefore it would also be interesting to explore the spectral broadening acquired by the signal pulses in the feedback fibre.

The experiments presented in this chapter were part of the investigation of the high-energy performance pertaining to an SPOPO with a single-mode feedback fibre in the cavity. As will be discussed in section 5.3, preliminary results from the experiments using an output coupler with transmissivity of 75% already demonstrated that the fibre-feedback OPO was capable of generating NIR and MIR pulse energies, internal to the cavity, with slope efficiencies of 53.6% and 17.8%, reaching to 4.1 μJ and 1.4 μJ, respectively. The overall parametric conversion efficiency was 50% at the maximum operating condition. The corresponding pulse energies extracted out of the cavity were 3.0 μJ (signal) and 1.1 μJ (idler) with 3-dB spectral bandwidths of 7.8 nm (signal) and 50.5 nm (idler). In addition, an intracavity supercontinuum covering components from 1510 nm to 1970 nm was observed. Section 5.4 shows an attempt to narrow the signal and idler spectral bandwidths by reducing the power launched into the feedback fibre. As a result, the 3-dB spectral bandwidth of the idler was narrowed by more than 42% to 29 nm and that of the continuum spectra was significantly reduced by ~10 times to 35 nm. It is believed that the performance of the OPO has not been optimised yet due to limitation by the available components including the lenses, output coupler and the feedback fibre at the time of the experiments. Nonetheless, to the best of our knowledge, the demonstrated pulse energies under these non-optimized conditions have already exceeded the highest reported pulse energies for picosecond OPOs that have both signal and idler extractable out of the cavity.

The optics between the pump source and the OPO were built by the author while the parameters of the initial OPO cavity were calculated by Dr. Lin Xu, who collaborated with the author to carry out the experiments. The data analysis presented in this chapter was performed by the author. It should be noted that the experiments were implemented towards the end of the author's candidature; therefore the results presented in this chapter only cover the data obtained up to the write-up of this thesis and do not represent a comprehensive investigation of the performance of the fibre-feedback OPO. Further optimisation and full characterisation of the system are yet to be implemented after the submission of this thesis and the results are expected to be published as a journal paper.

5.2 System Configuration

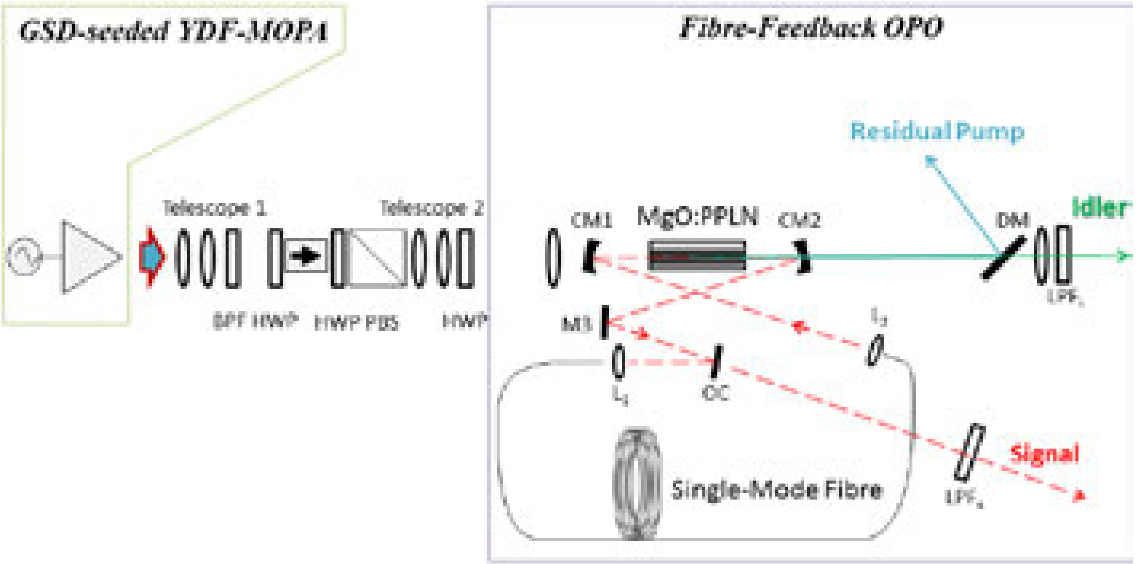

Figure 5-1 Experimental set-up of the fibre-feedback OPO, synchronously pumped by a compact high-pulse-energy GSD-seeded YDF-MOPA at a repetition rate of 1MHz.
BPF = band-pass filter, HWP = half-wave plate, PBS = polarisation beam splitter, DM = dichroic mirror, CM = curved mirror, M = plane mirror, OC = output coupler, L = aspherical lens, LPF = long-pass filter.

A schematic diagram of the experimental set-up is depicted in Figure 5-1. The pump source and the optical arrangement before the fibre-feedback OPO were the same as those used in Chapter 4 for the high-energy MIR generation experiments. The compact GSD-seeded YDF-MOPA system delivered 124-ps pulses with pulse energy of as high as 17.3 μJ at a repetition rate of 1.006 MHz in a linearly polarised and diffraction-limited beam. The pulses were centred at 1034.5 nm and carried a 3-dB spectral bandwidth of 0.8 nm. Details of the design and performance of this MOPA system are discussed in Chapter 3 of this thesis.

The band-pass filter (BPF) centred at 1025 nm with a 3-dB bandwidth of 50 nm was used to exclude the SRS and ASE outside the signal region from the high-energy NIR pulses, followed by a free-space optical isolator to protect the MOPA from any accidental back-reflection from the OPO. Pump power launched into the nonlinear crystal was controlled by a variable attenuator, which was implemented by combining a half-wave plate (HWP) with a polarisation beam-splitter (PBS). A two-lens telescope (Telescope 2) and a focusing lens were then used to obtain the required pump waist size and location inside the nonlinear crystal for the experiments. Unless specified otherwise, all the spot sizes mentioned in the rest of this chapter are referred to the $1/e^2$-intensity waist radii. A half-wave plate was placed in front of the optical parametric devices to set the polarisation of the pump beam for optimisation of the quasi phase-matching.

The nonlinear gain medium in the fibre-feedback OPO was the same crystal used in the harmonic-cavity OPO presented in section 4.5, i.e. a 40-mm-long, 1-mm-thick PPLN crystal (Covesion Ltd.) with a 5% magnesium oxide doping concentration. The crystal had five periodically poled gratings with periods of 29.52 μm, 29.98 μm, 30.49 μm, 31.02 μm and 31.59 μm. Each grating had an aperture of 1 mm by 1 mm. The end facets had specified parallelism within 5’ and were anti-reflection (AR) coated with reflectivity of < 1.5% for the pump and < 1% for the signal. The length was chosen based on the consideration discussed in section 4.2, i.e. interaction length, beam clipping at the crystal aperture, temporal walk-off among the interacting waves and acceptance bandwidth of the crystal. To implement temperature tuning and as an additional precaution against photorefractive damage, the crystal was mounted in an oven with a temperature controller tunable up to 200°C and a resolution of 0.1°C.

The resonator of the OPO was constructed based on a free-space bow-tie ring cavity (Figure 5-2), formed by two curved mirrors (CM1 and CM2, each with a radius of curvature of -250 mm) on both sides of the crystal and two plane mirrors (M_a and M_b) at the other corners of the arms of the cavity. Relatively large spot sizes in the PPLN were desired to reduce the peak intensities. The ABCD matrix formalism [115] was then used to model this ring resonator at an arbitrary repetition rate of 180 MHz (optical cavity length of 1.667 m), resulting in a signal waist of 106 μm at the centre of the PPLN. A pump waist of 102.5 μm was then used to approximately match the calculated signal waist. The corresponding signal and pump focusing parameters as defined in equation (2.25) were $\xi_s = 0.40$ and $\xi_p = 0.29$, respectively, which were less tight than the confocal focusing condition; however, this was accepted as the priority in the experiment was given to the prevention of damage to the crystal.

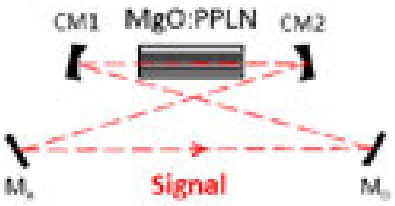

Figure 5-2 Bow-tie ring cavity with dummy mirrors M_a and M_b as described in text.

A standard single-mode fibre (Corning SMF-28e) for the telecommunication band around 1300-1600 nm was used as the feedback fibre to cover the majority of the required optical cavity length of 298.211 m for synchronisation with the pump repetition frequency. M_a was replaced by an output coupler and M_b was removed. The two fibre ends were positioned close to where the two plane mirrors were located. As shown in Figure 5-1, it was found that a plane mirror (M3) was needed for an additional folding of the signal beam to reach the output coupler (OC) due to limited space on the optical breadboard. The input end of the fibre was put after the output coupler (OC) and the output end of the fibre was directed towards the curved mirror CM1 to complete the resonator. All the cavity mirrors were coated to be highly reflective at the signal wavelengths but highly transmissive for the pump and idler; thereby forming a singly signal-resonant OPO. In addition, the single-mode fibre would be strongly absorbing for light at the idler wavelengths. Aspherical lenses (L_1 and L_2) were then used for launching the signal beam into and out of the fibre. The beam radii at these locations were 500 μm as calculated in the aforementioned model. For maximum launching efficiency, the numerical aperture (NA) of the focused beam going into the fibre should be matched to that of the fibre core, which was ~0.14. This implied a lens with focal length of ≈ 3.6 mm would be needed, but unfortunately no such lens was available at the time of the experiment and consequently lenses with focal lengths of 4.5 mm were used for L_1 and L_2. The positions of the fibre ends were then adjusted based on the ABCD model of the fibre-feedback cavity, whilst maintaining the calculated signal waist in the PPLN. Considering a signal wavelength of 1525 nm generated from parametric oscillation with grating period of 29.98 μm at a temperature of 90°C, the group index of refraction for the signal in the PPLN was calculated to be 2.1978, based on the temperature-dependent Sellmeier equation [116], and that in the fibre core was ~1.468 according to the calibrated data from the manufacturer. As a result, the required physical fibre length for the fibre-feedback SPOPO was calculated to be 202.16 m, after taking into account the free-space section of the resonator.

A long-pass filter (LPF_s) (Thorlabs FEL1250) with a cut-off wavelength at 1250 nm was placed after the output coupler (OC) to obtain the signal output pulses. The idler pulses were extracted through another long-pass filter (LPF_i) (Northumbria Optical Coatings LWP-4047-1-1-09) cutting off at 1950 nm, after the residual pump was filtered by a dichroic mirror (DM3). It should be noted that unless specified otherwise, the quoted pump powers correspond to power incident on the curved mirror CM1 and all the signal and idler output powers (and thus pulse energies) mentioned in this chapter have already taken into account the losses of all the optical elements involved in the measurements, i.e. they correspond to the values immediately after their respective output coupling mirrors.

5.3 High-Energy Performance with Intracavity Supercontinuum Generation

An OC with reflectivity of 25% was first chosen to explore the performance of the OPO. The signal and idler powers generated from the OPO with the 30-µm channel at an oven temperature of 90°C were plotted against the pump power in Figure 5-3. External to the cavity, the extracted pulse energies reached values of 3.0 µJ (signal) and 1.1 µJ (idler) at the maximum available pump power of 12.2 W. The corresponding slope efficiencies were 36% and 13.2%, respectively, and the pump threshold was ~3.8 W. Considering the power inside the cavity, the signal and idler were generated at a pump threshold of ~3.5 W and increased with slope efficiencies of 53.6% and 17.8%, respectively, reaching pulse energies of 4.0 µJ (signal) and 1.4 µJ (idler) after the exit facet of the PPLN, at the maximum pump power incident on the PPLN crystal of 10.9 W. At this maximum operating condition, the overall parametric conversion efficiency was 50%.

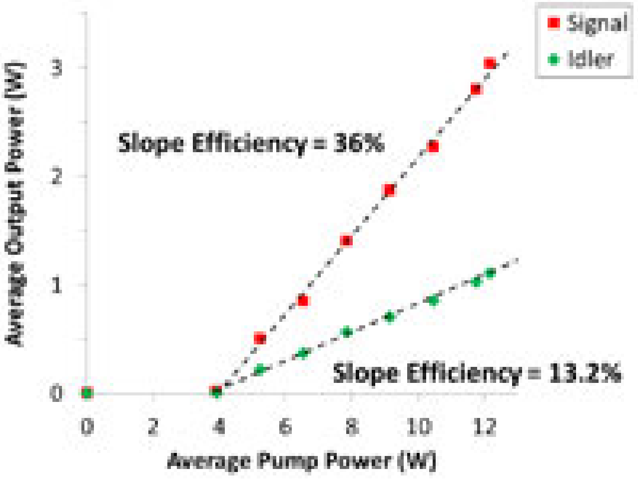

Figure 5-3 Average signal and idler output power versus pump power of the fibre-feedback OPO, generated with 29.98 µm grating period at 90°C and using an output coupler with transmissivity of 75%. Values shown were external to the cavity.

Figure 5-4 compares the signal spectra going into and out of the feedback fibre, measured at the maximum pump power, after the OC and with an 8%:92% beam splitter (Thorlabs BP108) at the fibre output, respectively. Both spectra were measured with an optical spectrum analyser (OSA) (Yokogawa AQ6375). The signal launched into the feedback fibre was centred at 1526 nm with a 3-dB spectral bandwidth of 7.8 nm. It can be seen that there was a significant spectral broadening as the pulse propagated through the fibre. The generated supercontinuum covered components from 1510 nm through 1970 nm, with 3-dB and 20-dB spectral bandwidths of 340 nm and 440 nm, respectively. From the dispersion profile of the feedback fibre (Figure 5-5), it is clear that the signal launched into the fibre was well into the anomalous dispersion regime. The spectral broadening was thus red-shifted and was predominantly due to a sequence of soliton-related dynamics as a result of soliton fissions. The idler spectrum shown in Figure 5-6 was measured with another OSA (Bristol 721) that was sensitive to the MIR wavelengths. The obtained spectrum indicates a 3-dB spectral bandwidth of 50.5 nm centred at 3212 nm.

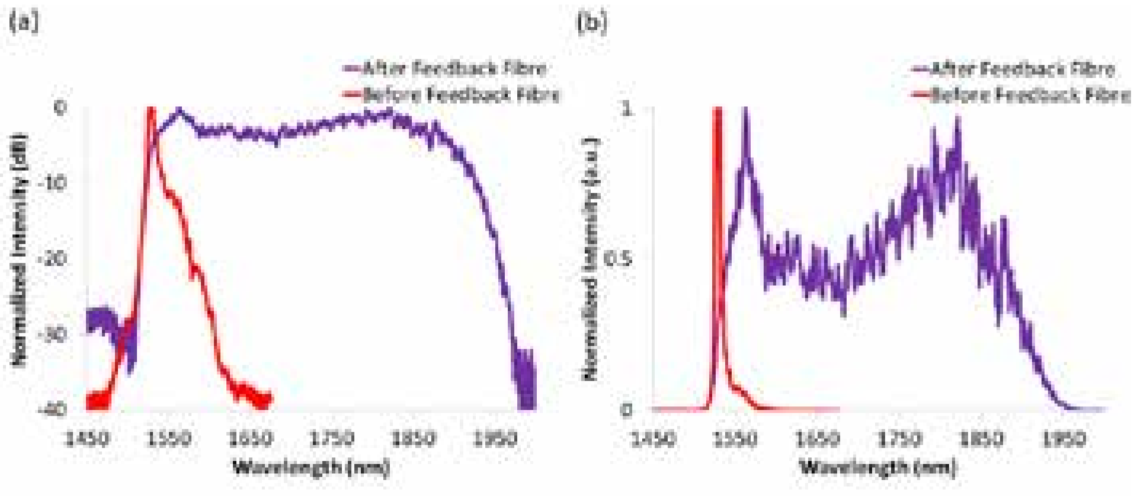

Figure 5-4 Spectrum of the signal before (resolution = 0.5 nm) and after (resolution = 1 nm) the feedback fibre in the OPO, generated with 29.98-μm grating period at 90°C and using an output coupler with transmissivity of 75%. (a) Logarithmic scale and (b) linear scale.

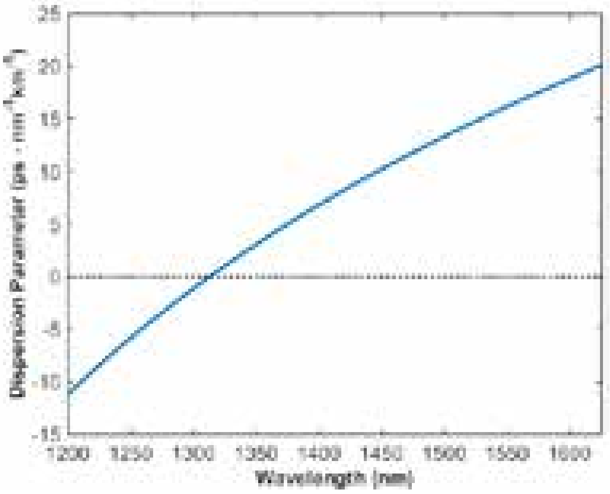

Figure 5-5 Dispersion parameter of the feedback fibre in the OPO cavity. (Based on data from supplier)

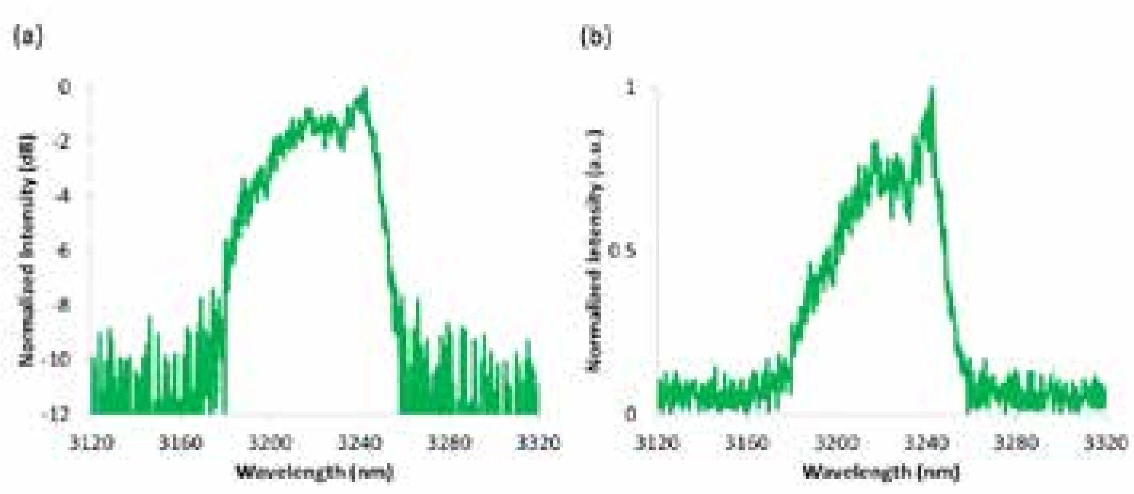

Figure 5-6 Spectrum (resolution = 1 nm) of the idler output from the fibre-feedback OPO, generated with 29.98-μm grating period at 90°C and using an output coupler with transmissivity of 75%. (a) Logarithmic scale and (b) linear scale.

Shown in Figure 5-7 is the temporal profile of the output signal measured after the OC with a 32-GHz-bandwidth photodetector (Agilent HP 83440D) and a 20-GHz-bandwidth digital communication analyser (Agilent 83480A). Due to the temporal gain narrowing effect [110], the measured FWHM pulse duration of the signal was 9.7% shorter than that of the pump pulse, implying a full-width-at-half-maximum (FWHM) duration of 112 ps after taking into account the artefact of a triggering problem mentioned in section 4.3. The maximum peak power of the output signal pulses was therefore 27.0 kW after the OC and 36.1 kW after the PPLN. The time-bandwidth product (TBP) of the output signal pulses was 113, which was 257 times of the transform-limit of a Gaussian pulse. The counterpart measurement of the idler pulses could not be performed as there was not any suitable photodetector or autocorrelator available at the time of the experiments.

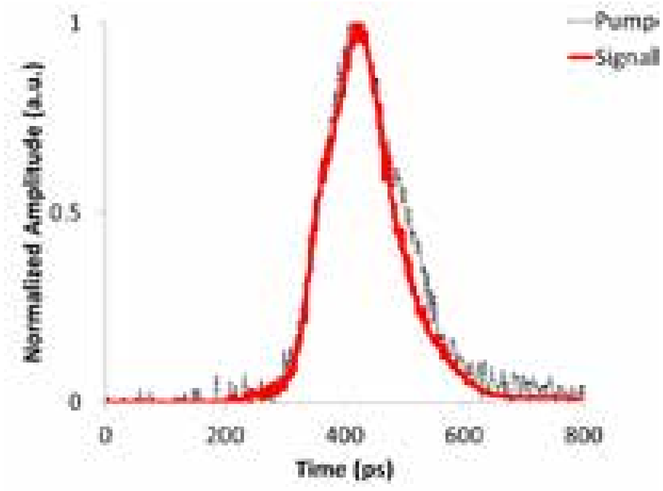

Figure 5-7 Temporal Profile of the signal output from the fibre-feedback OPO, generated with 29.98-μm grating period at 90°C and using an output coupler with transmissivity of 75%. Measurement was performed with a 32-GHz-bandwidth photodetector.

5.4 Spectral Bandwidth Reduction

As an attempt to reduce the spectral broadening of the signal and idler pulses, the OC in the experiment presented in the previous section was replaced with one that had a transmissivity of 90%. With this in the OPO, the maximum pulse energy extracted out of the cavity was measured to be 2.8 μJ and 1.05 μJ for the signal and idler, respectively, as shown in Figure 5-8. The pump threshold was ~4.7 W and the slope efficiencies were 37.8% (signal) and 14.1% (idler). When considering the power internal to the cavity, the signal and idler power scaled up with that of the pump at slope efficiencies of 46.8% and 19.6%, respectively, after the pump exceeded a threshold of ~4.2W. The maximum pulse energy of the signal after the PPLN was 3.2 μJ while that of the idler was 1.3 μJ, implying an overall conversion efficiency of 41.7%.

When comparing the spectral characteristics of the pulses to those generated with the 25%-reflectivity OC in the previous section, the spectral bandwidths of both the signal after the feedback fibre and the idler were narrowed as expected, due to the lower peak power of the signal pulses entering the fibre. At the maximum operating condition, the supercontinuum generated from the fibre shrank significantly by a factor of 10 in the 3-dB spectral bandwidth to 35 nm as shown in Figure 5-9, while the 3-dB spectral bandwidth of the idler was reduced to 29 nm (Figure 5-10).

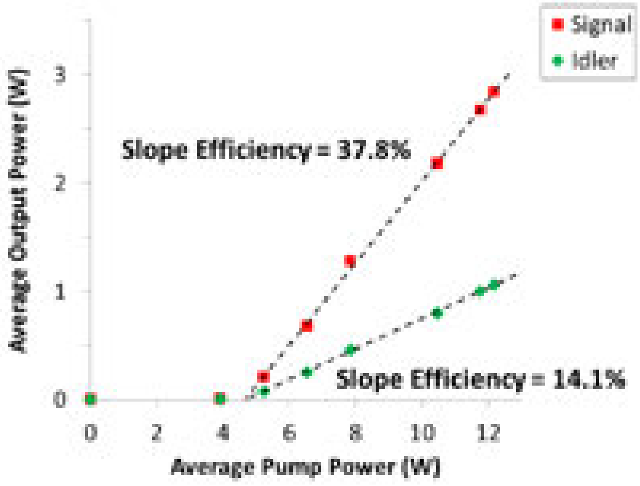

Figure 5-8 Average signal and idler output power versus pump power of the fibre-feedback OPO, generated with 29.98 μm grating period at 90°C and using an output coupler with transmissivity of 90%. Values shown were external to the cavity.

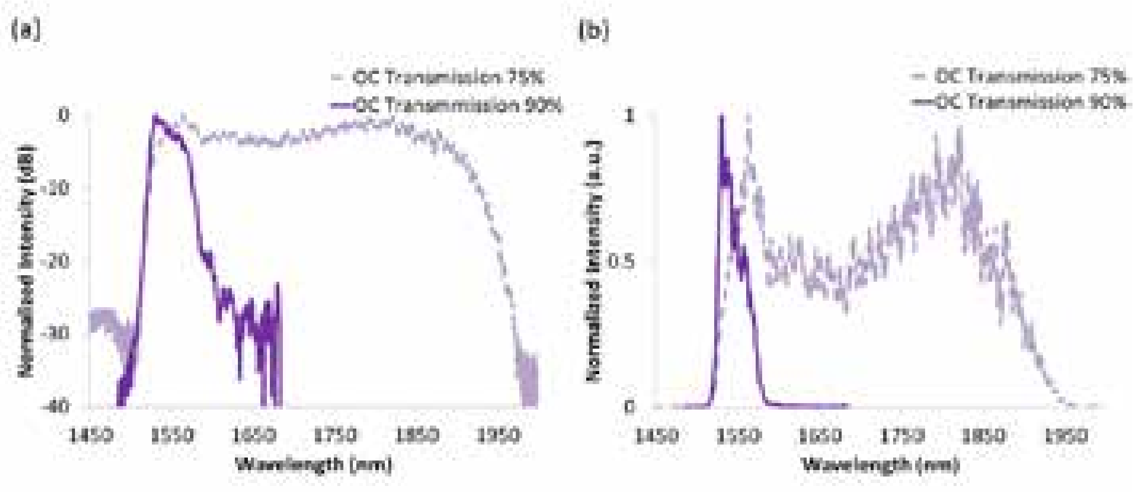

Figure 5-9 Spectrum (resolution = 1 nm) of the signal after the feedback fibre in the OPO, generated with 29.98-μm grating period at 90°C and using an output coupler with transmissivity of 90%. Corresponding spectrum with 75%-transmission output coupler was included for reference. (a) Logarithmic scale and (b) linear scale.

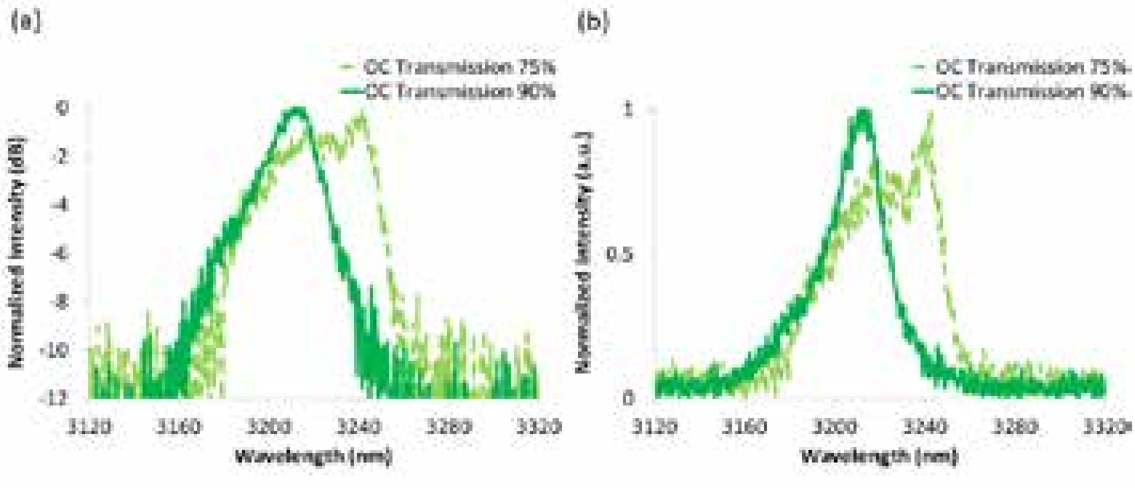

Figure 5-10 Spectrum (resolution = 1 nm) of the idler output from the fibre-feedback OPO, generated with 29.98-μm grating period at 90°C and using an output coupler with transmissivity of 90%. Corresponding spectrum with 75%-transmission output coupler was included for reference. (a) Logarithmic scale and (b) linear scale.

These results represent preliminary investigations of this fibre-feedback cavity. Further work should include other characterizations such as M^2 measurement for both the signal and idler beams, as well as further reduction of nonlinear spectral broadening by replacing the current feedback fibre with a hollow-core fibre.

5.5 Summary

In Chapter 4 three optical parametric devices, OPG, OPA and harmonic-cavity OPO were built to generate microjoule MIR picosecond pulses with different characteristics. In particular, the high-energy signal pulses in the harmonic-cavity OPO could not be coupled out. This chapter has presented the work towards a solution to this problem. A fibre-feedback configuration with a SMF-28e fibre was employed to construct a compact singly-resonant SPOPO at 1-MHz repetition rate to provide high-energy signal and idler pulses external to the cavity for potential practical applications.

With a 75%-transmission output coupler, pulse energies as high as 3.0 μJ (signal) and 1.1 μJ (idler) could be extracted out of the cavity. The 3-dB spectral bandwidth of the signal was 7.8 nm and that of the idler was 50.5 nm. The maximum pulse energies generated inside the cavity were 4.0 μJ (signal) and 1.4 μJ (idler), corresponding to an overall parametric conversion efficiency of 50%. The slope efficiencies were 53.6% (signal) and 17.8% (idler) within the cavity while those external to the cavity were 36% (signal) and 13.2% (idler). The generated idler pulse energies and spectral bandwidths were adequate for RIR-PLD/ RIR-PLA of materials such as PEG and PS, whilst the multi-microjoule signal pulses could also be utilised outside the cavity. In addition, an intracavity supercontinuum covering components from 1510 nm through 1970 nm was generated via the feedback fibre. The output signal attained a peak power of 36.1 kW with a FWHM pulse width of 112 ps. The TBP was 113, i.e. more than 250 times of a transform-limited Gaussian pulse.

When replacing the OC with one that had a transmissivity of 90%, the 3-dB spectral bandwidth of the idler pulses was reduced to 29 nm and that of the signal after the feedback fibre was narrowed by a factor of 10 down to 35 nm. The maximum available signal and idler pulse energies external to the cavity were 2.85 μJ and 1.05 μJ with slope efficiencies of 37.8% and 14.1%, respectively. The pulse energies after the PPLN reached to 3.2 μJ (signal) and 1.3 μJ (idler), corresponding to an overall parametric conversion efficiency of 41.7%, at the maximum pump power. Their respective slope efficiencies were 46.8% and 19.6%.

Although the demonstrated pulse energies are the highest reported so far for picosecond OPOs with both signal and idler extractable out of the cavity, it is believed that the performance was not at its optimum due to limitation on the available components at the time of the experiment. Unfortunately, further experiments could not be carried on until after the write-up of this thesis due to restricted time on the author's candidature and availability of components. Future work includes characterization of $M^2$and further optimisation of the pulse energies and spectral bandwidths with different coupling lenses, output couplers and feedback fibre. Moreover, deliberate intracavity supercontinuum generation would also be of interest, e.g. an idler-resonant fibre-feedback OPO employing a chalcogenide fibre might be very efficient for MIR generation into the fingerprint regime (7-20 μm).

Chapter 6

Gigahertz Femtosecond Fibre-Amplified VECSELs and Application to Supercontinuum Generation

6.1 Introduction

It has been seen in section 1.1.2 and section 2.4 that supercontinuum sources are of great interest to many industries and that photonic crystal fibres (PCFs) are extremely useful for supercontinuum generation due to their highly engineerable guiding properties that cannot be found in conventional fibres, such as high nonlinearity and shifted zero-dispersion wavelength (ZDW). Among the many frontiers of supercontinuum research are metrological applications, for which frequency combs with GHz pulse-repetition-rates are desirable. Generation of coherent supercontinua typically requires sub-100-fs pulses when pumping near the ZDW of a PCF [38]. On the other hand, it has been shown that supercontinuum with high coherence can also be generated with pulses of several hundred femtoseconds duration through all-normal-dispersion (ANDi) PCFs [39,40].

Mode-locked (ML) vertical-external-cavity surface-emitting lasers (VECSELs) are good candidates for generating femtosecond pulses at GHz repetition frequencies without the complexities that come with ML-Ti:Sapphire lasers as discussed in section 1.1.2. However, high-average power and sub-100-fs pulses have not yet been achieved in the same device. There is thus an interest in power scaling ML-VECSELs to produce a flexible source for coherent GHz supercontinuum generation.

The work presented in this chapter demonstrates a system in which the femtosecond pulses generated from a 3-GHz ML-VECSEL centred at 1040 nm were amplified in a Yb-doped-fibre (YDF)-MOPA configuration, and compressed through a high-throughput dielectric transmission grating. These pulses were then launched into a PCF to demonstrate coherent supercontinuum generation. Two different PCFs were investigated and compared—an ANDi PCF and a PCF with a ZDW at 1040 nm. Finally, section 6.5 presents an improved amplifier that was designed and built to replace the final-stage power amplifier that had been used for the supercontinuum experiment. With enhanced pump absorption and a better-quality tapered section, the re-built amplifier demonstrated a significant improvement in slope efficiency as well as a higher polarisation-extinction ratio (PER) at the MOPA output; thereby providing a promising source for future high-power supercontinuum generation and power-scaling of femtosecond seed sources.

This work was a collaborative project with the VECSEL group in the School of Physics and Astronomy. The VECSEL seed was prepared and operated by Dr. Robin Head. The fibre of the final-stage amplifier used during the supercontinuum experiment was cut and initially end-capped and tapered by Dr. Rohit Malik. Replacement of damaged end-cap and tapered section was done by the author. The amplifier system was built and operated by the author and the compressor was aligned by Dr. Jonathan Price. The PCFs used for the supercontinuum generation were collapsed by the author and another PhD student Mr. James Feehan. The power amplifier with improved performance was designed and built by the author, and the supercontinuum experiments were collaborative work between the author and Dr. Robin Head. This project was carried out at the early stage of the author’s doctoral programme; due to the departmental safety policy, the final-stage pump was occasionally operated by Dr. Jonathan Price when data was taken with average power of more than 50 W. The work presented in sections 6.2-6.4 in this chapter formed the basis of a journal paper published in the IEEE Photonics Technology Letters [125].

6.2 System Configuration

The schematic in Figure 6-1 illustrates the experimental set-up. It comprised a ML-VECSEL as the seed in a MOPA with three stages of YDF-amplifiers, followed by a high-throughput grating compressor and a PCF for supercontinuum generation.

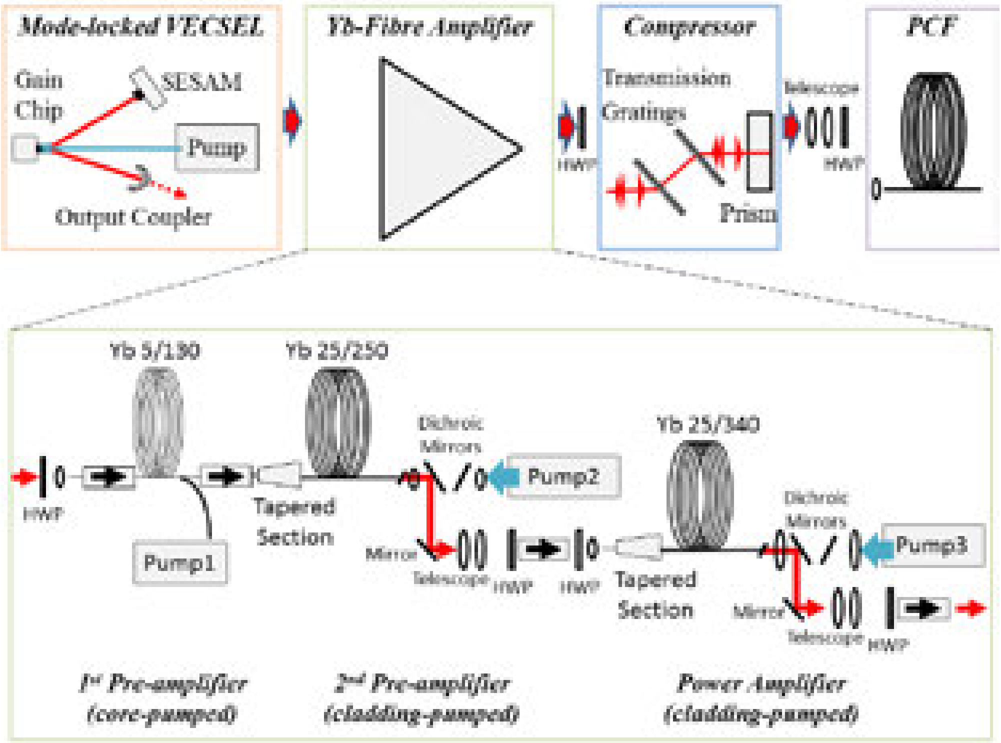

Figure 6-1 Experimental setup: a ML-VECSEL was used as the seed of the PM femtosecond Yb^{3+}- fibre MOPA system. The amplified pulses were then compressed and launched into the PCFs for supercontinuum generation. Red arrows indicate the propagation directions of the signal (λ = 1040 nm)

The ML-VECSEL consisted of a gain structure made of InGaAs quantum wells, a semiconductor saturable-absorber mirror (SESAM) with AlAs/GaAs distributed Bragg reflectors (DBRs), and a spherical output coupler with 0.3% transmission and 50-mm radius of curvature. In order to reduce misalignment due to mechanical vibration and thermal drifting, the gain chip was mounted on a water-cooled temperature-controlled copper block, and all components of the VECSEL set-up were mounted on an Invar plate. With a pump power of 1.3 W at 830 nm from a fibre-coupled diode laser, the ML-VECSEL produced 405-fs pulses (assuming a sech^2 temporal profile) at a repetition frequency of 3 GHz. The average output power was ~15 mW. Figure 6-2 shows the autocorrelation of the output pulses along with their sech^2-fit and their spectrum at 1040 nm. The 3-dB spectral bandwidth was 2.85 nm, giving a time-bandwidth product of 0.32, which was only 1.6% higher than the transform limit of a sech^2 pulse. The autocorrelation traces and spectra presented in this chapter were measured with an autocorrelator (Femtochrome Research FR-103MN) and an optical spectrum analyser (ANDO AQ6317B) respectively.

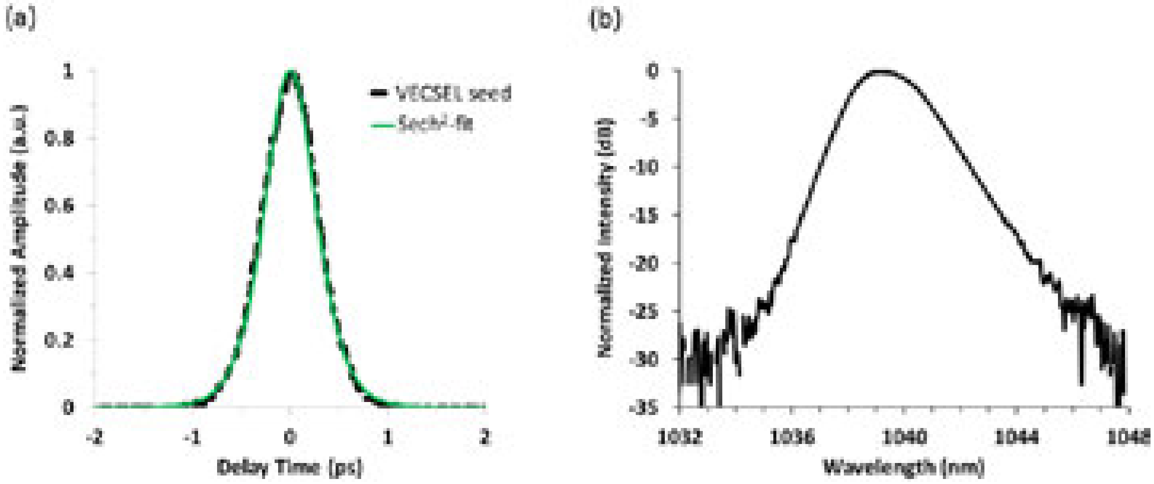

Figure 6-2 (a) Measured (black) and sech^2-fitted (green) autocorrelation trace and (b) spectrum (resolution = 0.2 nm) of the output pulse from the ML-VECSEL

The pulse generated from the ML-VECSEL was launched through free-space optics into a fiberised polarisation-maintaining (PM) optical isolator that was spliced to the first pre-amplifier of the MOPA system. Approximately 8% of the signal power at the output of the VECSEL was reflected by a beam splitter into an optical spectrometer (Ocean Optics HR4000) to monitor the spectrum of the source.

This provided real-time information on how stable the mode-locking was throughout the experiments.

Two pre-amplifiers were used to amplify the signal before extracting high power from the final-stage power amplifier. The lengths of the amplifiers were chosen to allow high pump absorption, while ensuring an efficient signal power extraction with optical signal-to-noise ratio of more than 20 dB at each stage. The first pre-amplifier consisted of a 2-m-long PM-YDF of 5-μm core diameter and 130-μm cladding diameter. It is backward core-pumped by a 975-nm single-mode fiberised laser diode to amplify the pulses to a maximum power of 75 mW. The small core diameter was chosen to maintain a single-mode operation. The signal was then passed into the second pre-amplifier, which was composed of a 2.7-m-long large-mode-area (LMA) PM-YDF (Nufern PLMA-YDF-25/250-VIII), having a core diameter of 25 μm with an NA of 0.06 and a cladding diameter of 250 μm with an NA of 0.46. A stable operating point at ~5.7-W pump power was chosen to backward pump the fibre to give a signal output power of 1.5W. The signal was then free-space launched into the final-stage power amplifier through a telescope and an optical isolator. The final-stage amplifier fibre had a 25-μm core diameter with an NA of 0.055, a 340-μm cladding diameter with an NA of 0.45, and a slightly longer length of 3 m. This fibre was initially chosen for efficient pump coupling into the fibre; however, section 6.5 will show that it was also possible to implement an efficient amplifier with a 25/250 fibre. The signal power was boosted through the final-stage amplifier with backward pumping by a 976-nm diode-stack module (Laserline LDM 200-200), which had a delivery fibre with a cladding diameter of 300 μm and an NA of 0.22. The maximum available pump power was 200 W. Backward pumping was employed to maximise the conversion efficiency. Angle-polished silica end-caps, fibre coiling and water cooling were implemented for thermal and mode management in the second pre-amplifier as well as the power amplifier for the reasons explained in chapter 3. The coiled sections of the fibres were wrapped around aluminium cylinders for passive cooling. Isolators were used to prevent backward amplified spontaneous emission (ASE) leakage between stages in the MOPA, which might otherwise cause damages to the seed and the pre-amplifiers.

The MOPA was then used as a pump source for an investigation of two different possible ways to generate coherent supercontinuum via two different PCFs. One was a 20-m-long ANDi PCF (NKT Photonics NL-1050-NEG-1) and the other had a ZDW at 1040 nm (NKT Photonics SC-5.0-1040) with a length of 1 m. Their specifications are shown in Table 6-1.

Table 6-1 Specifications of PCFs used in the supercontinuum generation experiments

NKT Photonics NL-1050-NEG-1		*NKT Photonics SC-5.0-1040*	
Material	Pure Silica	Material	Pure Silica
Cladding diameter	127 ± 5 μm	Cladding diameter	125 ± 3 μm
Coating diameter	245 ± 10 μm	Coating diameter	244 ± 10 μm
Coating material	Acrylate	Coating material	Acrylate
Core diameter	2.3 ± 0.3 μm	Core diameter	4.8 ± 0.2 μm
Dispersion @1040 nm	-10 ps/nm/km	Zero dispersion wavelength	1040 ± 10 nm
Attenuation @1000-1100 nm	< 30 dB/km	Attenuation @1040 nm	< 3 dB/km
MFD @1064 nm	2.2 ± 0.5 μm	MFD	4.0 ± 0.2 μm
NA @1064 nm	~ 0.37	NA @ 1060 nm	0.2 ± 0.05
Nonlinear coefficient @1064 nm	~ 37 $(W\cdot km)^{-1}$	Nonlinear coefficient @1060 nm	~ 11 $(W\cdot km)^{-1}$
Cut-off wavelength	< 300 nm	Cut-off wavelength	< 1000 nm

In contrast to the direct amplification scheme employed in the MOPA system presented in Chapter 3 where no pulse compression was implemented for the purpose of simplicity, here the use of a compressor after the power amplifier was necessary. As will be shown in the next section, the original 405-fs pulses generated from the VECSEL experienced significant dispersion through the MOPA; therefore, the amplified pulses needed to be re-compressed to sub-original pulse duration in order to investigate coherent supercontinuum generation.

The compressor was built with a prism and a pair of high-throughput fused silica transmission gratings (Ibsen FSTG-PCG-1250-1064) with a grating resolution of 1250 lines/mm. The groove period was chosen such that it was small enough to only allow the first-order diffraction to exist. The modelled dispersion parameters provided by Dr. Jonathan Price for the amplifier fibres with core diameters of 5 μm and 25 μm were ~-40 ps/nm/km and ~-30 ps/nm/km respectively This led to an estimated group delay dispersion of 0.262 ps^2 in the MOPA. An initial grating separation of 1.95 cm was calculated by compensating the estimated quadratic phase distortion in the amplified pulse with the corresponding spectral phase derivative for the diffraction gratings [126].

6.3 Femtosecond Fibre Amplifier

It was observed on a spectrum analyser that the wavelength of the Laserline LDM 200-200 pump-diode module drifted from 971 nm to the optimised wavelength of 976 nm in approximately 20 minutes after being turned on. Therefore it was necessary to wait for the wavelength stabilisation to be settled before characterizing the MOPA output. With the 3-m 25/340 large-mode-area (LMA) fibre in the final-stage amplifier, the highest average output power obtained from the MOPA system was 37 W, at which point the power went into saturation. This corresponded to a gain of 14.7 dB in the final stage and 34 dB throughout the entire MOPA chain. At this operating condition, a PER of 13dB and an M^2 of ≈ 1.2 were measured. Figure 6-3 shows the average output power of the MOPA system plotted against the launched pump power for the final-stage amplifier. It showed a slope efficiency of 40%, which was lower than expected for an optimised Yb-amplifier system [67,127–129]. This was thought to be caused by low pump absorption. Nonetheless, in view of the short-term availability of the VECSEL seed laser from the collaborator, the experiments with the supercontinuum generation was carried on with this MOPA. However, possible causes of low pump absorption will be discussed in section 6.5, followed by a subsequent investigation on the improvement of the power-scaling capability of the MOPA system. The re-designed and re-built power amplifier resulted in a boost of the slope efficiency by more than a factor of two.

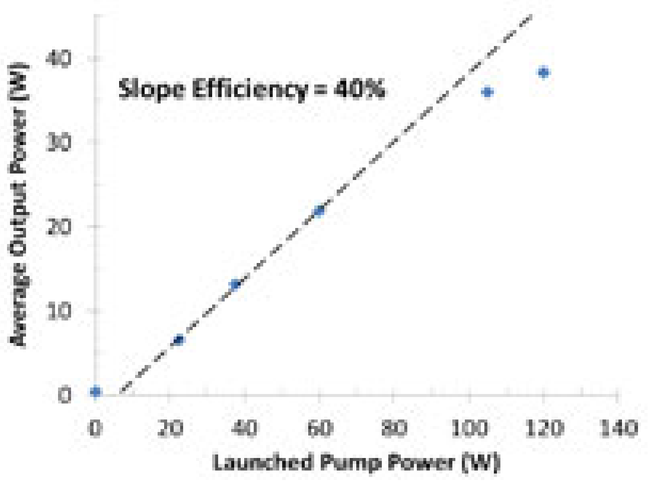

Figure 6-3 Average output power versus launched pump power of the final-stage amplifier made of the 3-m 25/340 YDF. Power started to saturate at about 35 W.

Pulse durations at different stages of the MOPA system, at maximum-power operation, were estimated based on the corresponding autocorrelation measurements (Figure 6-4 (a)) with de-convolution factors of 0.648 and 0.707 respectively for sech^2 and Gaussian pulses. The FWHM pulse width of the 405-fs pulses (sech^2-fitted) from the VECSEL was broadened to ~1.9 ps (Gaussian-fitted) after the pre-amplifiers and ~3 ps (Gaussian-fitted) at the end of the MOPA. This obvious temporal broadening was due to the group velocity dispersion in the fibres. On the other hand, the pulses did not acquire a lot of spectral broadening as can be seen in Figure 6-4 (b). The 3-dB bandwidth was broadened from 2.85 nm at the

VECSEL output to only 3 nm after the pre-amplifiers and 4 nm at the MOPA output. Assuming that the nonlinear refractive index coefficient n_2 is ~2.6 x 10^{-20} $m^2 W^{-1}$, the nonlinear length defined in equation (2.10) was estimated to be ~24 m and ~6.6 m for the second pre-amplifier and power amplifier respectively. Therefore it is believed that the nonlinear interaction was not strong enough to generate significant spectral broadening within the lengths of fibres used in our amplifier stages. A more detailed analysis could be implemented by modelling the pulse propagation along the fibre amplifiers utilizing the nonlinear Schrödinger equation described in section 2.2.3.

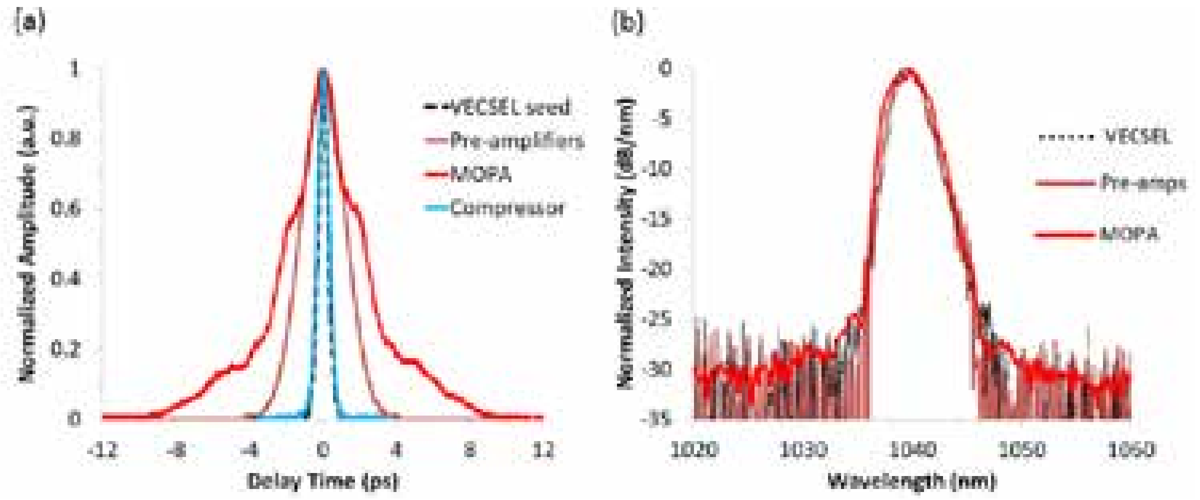

Figure 6-4 (a) Autocorrelation profiles and (b) spectra (resolution = 0.2 nm) at different stages of the MOPA system used for the supercontinuum experiment. Measurements were performed at maximum-power operation. Autocorrelation profile of the re-compressed pulse (blue) is shown in (a) to compare with the seed pulse.

The amplified and chirped pulses were then re-compressed by the high-throughput compressor with a measured efficiency of as high as 70%, resulting in an average power of 21 W after the compressor. From Figure 6-4 (a), it can be seen that the autocorrelation profile of the compressed pulses almost perfectly overlaps with that of the seed pulses. The compressed pulse duration was

~430 fs (sech^2-fitted). A more efficient pulse compression by the grating pairs to even shorter pulse duration could be realised if further power scaling were available from the MOPA to increase the spectral broadening and reach to the parabolic amplification regime [51].

6.4 Supercontinuum Generation via PCFs

Application of the VECSEL-seeded MOPA system for coherent supercontinuum generation was then explored by launching the amplified and compressed pulses into the two different PCFs in turn. A half-wave plate was placed in front of the coupling lens at the PCF input to enable optimisation on the supercontinuum generation. The highest measured transmission efficiency for both PCFs was ~50%.

6.4.1 All-Normal-Dispersion Photonic Crystal Fibres

The supercontinuum spectra generated via the ANDi PCF as a function of the average output power are shown in Figure 6-5. The maximum power obtained was 3.9 W, at which the supercontinuum spanned a 10-dB bandwidth of 195 nm and a 20-dB bandwidth of ~205 nm. The profile was relatively symmetric and had flatness of better than ±1.5 dB over a span of 150 nm. The spectral broadening was predominantly due to self-phase modulation (SPM) since the pulses were propagating in the normal-dispersion regime in the PCF and no soliton-related dynamics were involved. A high degree of coherence was therefore expected to exist in the pulses resulting from this intrinsically low-noise process [40]. At maximum-power operation, the supercontinuum spectrum carried ~20,000 modes with a spectral power density of ~20 mW/nm. The output power was limited mainly by the thermal loading at the input of the PCF. This corresponded to an operating power of ~18 W out of the power amplifier. Damage to the input end of the PCF was observed when the system was operated above this power level.

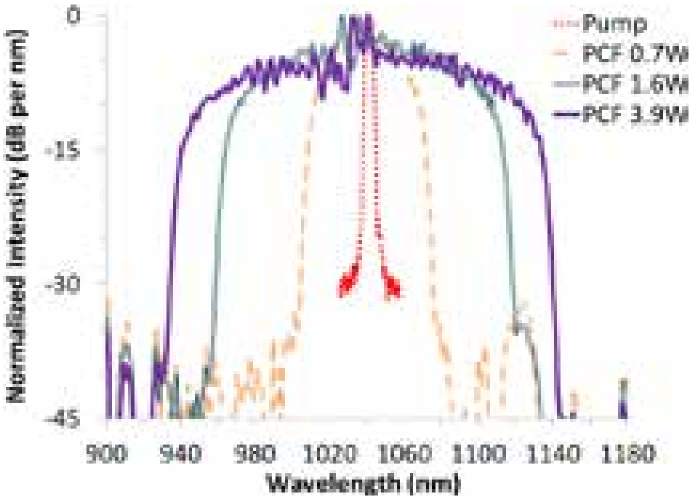

Figure 6-5 Spectra (resolution = 0.5 nm) of supercontinuum generation at different output power of the ANDi PCF.

6.4.2 1040nm-Zero-Dispersion-Wavelength Photonic Crystal Fibres

Broader supercontinuum spectra can be generated when pumping close to the ZDW of a PCF [38]. Therefore it is also interesting to explore the use of the MOPA system to pump a PCF with ZDW at 1040nm. At the maximum non-damaging operating power, the supercontinuum spectra generated by the 1040-nm-ZDW PCF covered spectral components from 750 nm to 1300 nm, as shown in Figure 6-6. The 20-dB bandwidth consisted of a 100-nm span at the lower-wavelength regime and a 280-nm span at the longer-wavelength regime. The average power measured at the PCF output was 2.6 W, corresponding to an average spectral power density of ~5 mW/nm with ~50,000 modes contained in the spectrum.

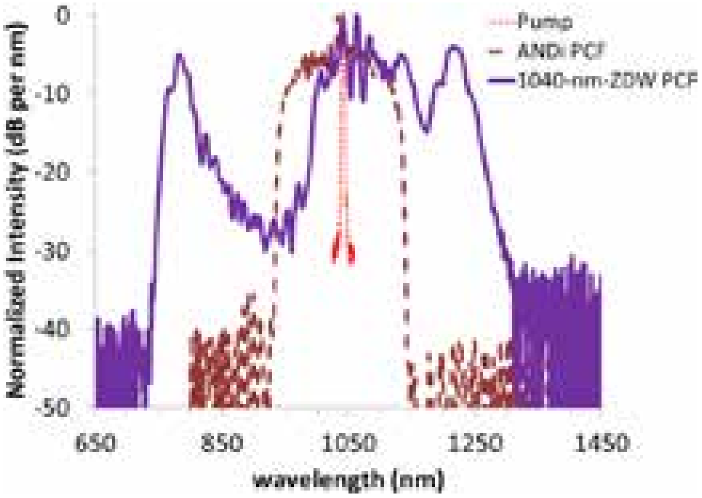

Figure 6-6 Supercontinuum spectrum (resolution = 0.5 nm) generated with 1-m-long 1040-nm-ZDW PCF and 20-m-long ANDi PCF

The process of continuum generation in the 1040-nm-ZDW PCF did not only involve SPM, but also a sequence of soliton-related dynamics as a result of soliton fissions. Consequently, as illustrated in Figure 6-6 , the supercontinuum contained wider spectral bandwidth and larger intensity variation across the bandwidth compared to the spectrum obtained with the ANDi PCF. The generated pulses were believed to be temporally incoherent since the pump pulse duration was ~400 fs, which was significantly wider than the sub-100-fs duration that is usually required to generate coherent pulses when pumping near the ZDW in the anomalous dispersion regime of a fibre [38].

6.5 Power Amplifier Optimisation

In section 6.3, the 3-m-long 25/340 YDF used in the power amplifier provided an average output power up to 37 W, with a slope efficiency of only 40%. Clearly, there was room for improvement in the power-scaling capability of the MOPA. This would generate pulses with higher peak power for pumping the PCFs to get broader supercontinuum spectra. Furthermore, reaching to the parabolic regime would allow for pulse compression to even shorter pulses [51] and possibly enable coherent supercontinuum generation via the 1040-nm-ZDW PCF.

As mentioned before, the fitted slope efficiency was lower than expected and that was thought to be caused by low pump absorption at the final-stage amplifier. This might have been due to a combination of factors. Firstly, pump launch was optimised at low power for obvious safety reason, but there could have been a drift in the coupling of the high-power pump beam into the fibre during the measurement. Secondly, the length of the fibre was too short in combination with the low core-to-cladding ratio. Finally, an unexpected drift of the pump wavelength might have occurred during the experiment.

To enhance the pump absorption and power-scaling capability, the power amplifier was redesigned and rebuilt with a 25/250 YDF with a longer length of ~5 m. The length was determined by optimizing the amplified signal power and ensuring an efficient pump absorption in the numerical modelling of a backward-pumped fibre amplifier based on the coupled rate equations as described in section 2.2.3. Figure 6-7 illustrates the simulation result of launching 140-W pump power into a 4.7-m-long 25/250 YDF. The pump absorption was more than 30 dB and the signal acquired more than 20 dB of gain, reaching an average output power of 131 W. A new tapered section and end cap were then made for this LMA fibre.

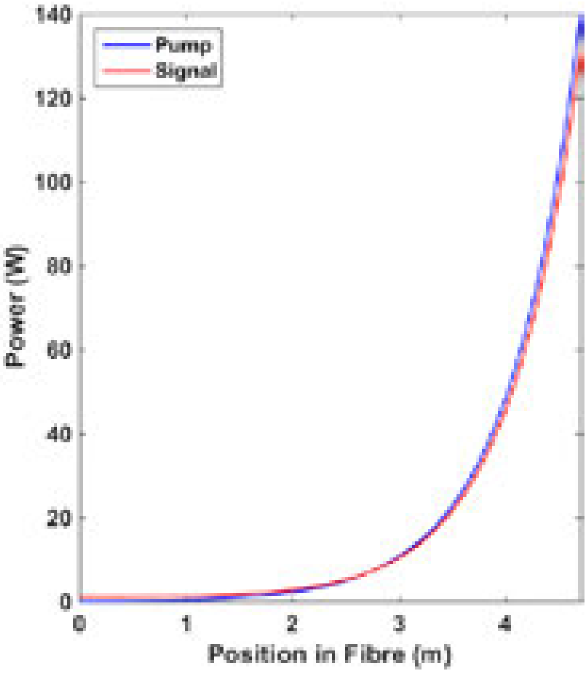

Figure 6-7 Numerical simulation of the redesigned power amplifier when backward-pumped with an average power of 140 W.

Characterisation of the MOPA with this new power amplifier showed a significant improvement on the power-scaling capability over the power amplifier used in the supercontinuum experiment. As illustrated in Figure 6-8, a boost in the slope efficiency of more than 2.2 times, increasing from 40% to 90%, was achieved. This was a highly efficient amplifier given that the theoretical limit was 93.85%. Moreover, the PER of the signal at 29-W average output power was measured to be ~18 dB, which was a 5-dB improvement. The M^2 of the output beam at this operating power was measured to be ≈ 1.17, which was as good as the previous amplifier.

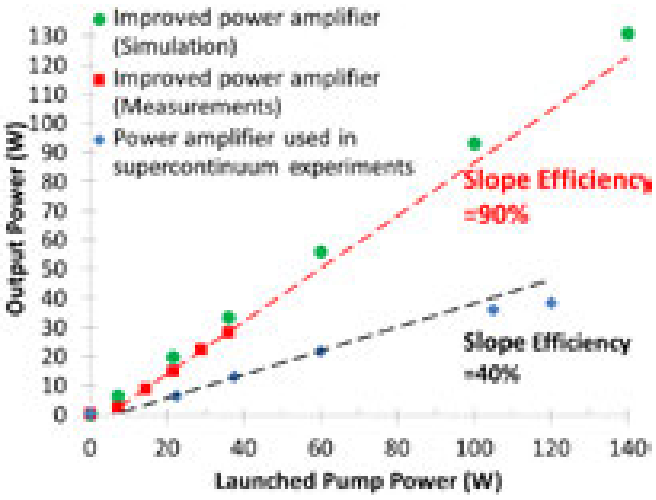

Figure 6-8 Average output power versus launched pump power of the re-designed power amplifier with a 4.7-m-long 25/250 YDF LMA, showing significant improvement on slope efficiency

In Figure 6-8, data at higher power was not experimentally measured with the new power amplifier by the author in compliance with the laser safety policy at the time of the experiment. However, the projection of the slope efficiency (red dashed line) is included in the graph to provide a guide to the expectation of the average output power at higher-power operation. Also included in the figure is the calculated output power (green points) at various pump levels, showing the agreement between the experimental and simulated power-scaling performance. Furthermore, since a launched pump power of more than 120 W had been used with the previous power amplifier without any damage to the fibre, it is believed that the improved power amplifier can also be operated at pump power of at least 120 W without damaging the system. It is therefore expected that the pulses could attain an average power of more than 100W with this improved power amplifier.

Combining with the VECSEL seed, the improved MOPA is a promising pump source for generating broader supercontinua via the PCFs. However, experiments on pumping the PCFs with this new power amplifier could not be completed due to an instability issue with the VECSEL seed. The mode-locking state could not be sustained for more than ~3-5 minutes; after which it went to CW emission and required to be aligned again before experiments could be continued. After the new power amplifier was tested and characterised, the VECSEL source failed to work in a reliable condition—it was only able to stay mode-locking for less than ~10 seconds. In view of this, further experiments on supercontinuum based on this VECSEL-MOPA could not be carried on.

6.6 Summary

This chapter has demonstrated that the combination of ML-VECSEL and YDF-amplifiers could form a high-power-MOPA pump source for generating supercontinuum with multi-watt average power at multi-GHz repetition rates. The VECSEL-MOPA provided an average power up to 37 W at 3-GHz repetition frequency. The amplified pulses were then re-compressed to 430-fs duration by a high-throughput transmission-grating compressor with an efficiency of as high as 70%. Supercontinuum was generated by launching the compressed pulses into two different PCFs with different properties. Firstly, supercontinuum with a flatness of better than ±1.5 dB over a span of 150 nm was generated via an ANDi PCF. It had a 200-nm 10-dB bandwidth and an average power of 3.9 W. Secondly, a 1040-nm-ZDW PCF was employed to generate supercontinuum with spectral components covering a wavelength range from 750 nm through to 1300 nm at an average power of 2.6 W, but with much higher spectral intensity variations. Spectral power density of ~20 mW/nm and ~5 mW/nm were generated in the ANDi and 1040-nm-ZDW PCFs, respectively.

Furthermore, an improved power amplifier was designed and built to boost the slope efficiency by more than two-fold to 90% and better the PER by 5 dB to a value of 18 dB. Unfortunately the VECSEL seed failed to sustain mode-locking for practical durations after the new power amplifier had been tested. As a result, further experiment on supercontinuum generation with the VECSEL-MOPA based on the new power amplifier could not be continued. However, the new amplifier showed promising power-scaling capability along with good PER and M^2. In addition to generating potentially much wider supercontinuum spectra, shorter re-compressed pulses could possibly be realised and thus enhancing the coherence of the supercontinuum generation via the 1040-nm-ZDW PCF. Moreover, it is believed that this highly efficient amplifier can be applied to power-scale femtosecond GHz seed lasers, such as a waveguide oscillator, to more than 100 W of average power. Potential applications include high-power GHz self-referencing frequency comb generation.

Chapter 7

Conclusions

7.1 Summary and Main Achievements

This thesis has presented the development of novel, high-power and high-energy ultrashort-pulse sources that shared a common high-level system architecture, namely nonlinear frequency conversion of Yb^{3+}-doped-fibre (YDF)-amplified compact semiconductor lasers. The block diagram of such approach is shown again in Figure 7-1 for reference.

Figure 7-1 Block diagram of the ultrashort-pulse systems presented in this thesis

The review on the essential mathematics, physics and technologies that are directly relevant to the understanding of the discussion in the thesis has been provided in Chapter 2, covering the building blocks of the presented systems. These include gain-switched diode lasers (GSDLs), mode-locked vertical-external-cavity surface-emitting lasers (ML-VECSELs), YDF-amplifiers and master-oscillator power amplifiers, periodically-poled-MgO:LiNbO3 (PPLN)-based optical parametric generators, amplifiers and oscillators (OPGs, OPAs, and OPOs), as well as photonic crystal fibres (PCFs) for supercontinuum generation. It has been shown that MOPA configurations along with cladding-pumping technology and large-mode-area YDFs provide a route to compact and efficient pulsed fibre laser systems with high output beam qualities while projecting the pulse properties from the master oscillators to the high-power output. In addition, optical parametric devices and PCFs open the pathway to highly customisable nonlinear frequency conversion.

Thanks to a uniquely designed flexible 1-μm GSD-seeded YDF-MOPA system (Chapter 3), which demonstrated the highest reported pulse energies from such MOPA systems, high-pulse-energy MIR (and NIR) picosecond pulses were successfully generated via an OPG, an OPA, a harmonic-cavity OPO and a fibre-feedback OPO (Chapter 4 through Chapter 5). The highest reported MIR and NIR pulse energies from a picosecond OPO were produced through the harmonic-cavity OPO and the fibre-feedback OPO, respectively. Furthermore, the fibre-feedback OPO also showed the highest reported MIR pulse energies from a picosecond OPO that has both signal and idler outputs. In addition, the first reported use of a fibre-amplified ML-VECSEL as a pump source for supercontinuum generation were demonstrated (Chapter 6) with YDF and PCF technologies. The main results obtained from these systems are put together below for completeness of this section.

Chapter 3 presented a stable, compact, robust and flexible GSD-seeded MOPA system capable of generating high-energy, high-peak-power and high-average-power picosecond pulses with narrow spectral linewidth in a diffraction-limited and single-polarisation output beam. It employed simple direct amplification via commercial conventional YDFs with core diameters of ≤ 25 μm and a total length of 6.6 m, in a nearly all-fiberised configuration with a minimum of free-space optics in the final-stage power amplifier.

In the mode-locking regime of the oscillator, pulses with duration of as short as 18.7 ps were demonstrated and power-scaled to an average power of 23.8 W, corresponding to a pulse energy of 3.2 μJ at a repetition rate of 7.53 MHz. The peak power achieved was ~170 kW, at which point stimulated Raman scattering (SRS) became significant and the 3-dB spectral bandwidth was broadened to 2.7 nm. Further energy scaling was primarily limited by SRS. When detuning towards the gain-switching regime, 120-ps pulses were generated from the seed and an overall energy gain of 66.7 dB was acquired through the YDF-amplifier cascade, achieving pulse energies of 17.7 μJ at 5.47-MHz repetition frequency. This corresponded to an average output power of 97 W. A maximum peak power of 197 kW was demonstrated. The measured 3-dB spectral bandwidth of 0.87 nm contained 13.8-μJ pulse energy, making this MOPA an attractive high-energy source for bandwidth-dependent applications. The PER and M^2 were measured to be > 14 dB and ≈ 1.07 respectively at the maximum operating condition. Power fluctuated only by ~1% over 30 minutes of continuous operation at the maximum output power, with no change in the spectral and temporal domains. This compact, stable and robust picosecond source should be attractive to diverse sectors for a variety of applications, especially in high-throughput material processing and for nonlinear frequency conversion to generate high-energy pulses in other spectral regions. In particular, when operating at 1-MHz repetition frequency, it became a promising pump source for optical parametric devices to generate MIR pulses with energies and average powers that had been shown adequate for RIR-PLD and RIR-PLA applications.

Chapter 4 discussed the work on demonstrating microjoule MIR picosecond pulses at 1-MHz repetition rate through various optical parametric processes pumped by the YDF-MOPA presented in Chapter 3. Pulse properties from three different but relatively simple parametric configurations were compared.

The OPG had a simple single-pass configuration and provided a tunability of 1479-1787 nm (signal) and 2455-3445 nm (idler). The generated signal and idler pulse energies increased with slope efficiencies of 38% and 17.5%, reaching 2.7 μJ and 1.2 μJ, respectively, at which point the overall parametric conversion efficiency was 32%. The time-bandwidth products (TBPs) were 77.1 (signal) and 107 (idler) as a result of the very broad 3-dB spectral bandwidths of 5.6 nm (signal) and 38 nm (idler). In addition, the M^2 were measured to be ≈ 3.2 and ≈ 4.4 for the signal and idler, respectively.

When injecting a seeding signal with a 3-dB spectral bandwidth of 0.03 nm to realise an OPA, the 3-dB spectral bandwidths of the signal and idler were significantly narrowed to 0.06 nm and 6.7 nm, respectively. In addition, the TBP of the signal was improved to only twice of the transform limit of a Gaussian pulse, and the TBP of the idler was estimated to be a factor of ~5 better compared to the OPG. Also, the M^2 of the signal was improved to be ≈ 2.1. Unfortunately, idler M^2 was not measured due to lack of a suitable camera at the time, but the M^2 can be expected to be greater than that of the signal. Effective gain of as high as 80 dB was observed from the OPA. However, possibly due to self-focusing, the crystal was damaged when the energies reached to 3.2 μJ (signal) and 1.3 μJ (idler). Seeding the OPA with a broader 3-dB spectral bandwidth of 0.3 nm increased the maximum extractable pulse energies to 3.8 μJ (signal) and 1.7 μJ (idler) without damaging the crystal at maximum available pump power, corresponding to an overall conversion efficiency of 45.6%. Slope efficiencies of 40.5% and 18% were observed for the signal and idler, respectively.With a broader seeding bandwidth, the 3-dB spectral bandwidths increased to 0.33 nm (signal) and 8.6 nm (idler), but they are still significantly narrower than those from the OPG.

The harmonic-cavity OPO employed a cavity length of 192 times shorter than that required for a conventional synchronously pumped OPO (SPOPO) at 1-MHz pump repetition rate. External to the cavity, the slope efficiency of the idler generation was 17.3%, reaching a maximum idler pulse energy of 1.5 μJ. Inside the cavity, the idler power scaled up at a slope efficiency of 22.6%; pulse energy of 1.8 μJ was generated at the maximum pump power, corresponding to a conversion efficiency of 16.6% for the idler. An overall parametric conversion efficiency of 51.2% from pump to signal and idler was achieved. The spectral bandwidth of the idler pulses was 6.5 nm, which was in the same order as that from the OPA. Moreover, the idler M^2 was measured to be ~2, which was equivalent to that found for the signal in the OPA and was consequently assumed to be better than that for the OPA idler. Tuning of idler wavelengths from 2276 nm to 3504 nm was demonstrated by accessing different gratings of the crystal at various temperatures.

Cavity-length detuning was also explored and a shift of 3 nm in the signal wavelength was observed with the detuning before oscillation ceased.

In terms of the suitability as a MIR source for RIR-PLD/ RIR-PLA of materials such as polyethylene glycol (PEG) and polystyrene (PS), the OPG provided an adequate idler spectral bandwidth and tunability, but the relatively poor M^2 would limit the focused spot sizes achievable in a PLD chamber and hence cause practical difficulties for implementation. On the other hand, the OPA provided better M^2 and narrower spectral bandwidths, but the tunability was limited by that of the seed source, complicating any proposed application. Finally, the harmonic-cavity OPO, although more complex, generated idler pulses with suitable spectral bandwidth, M^2 and tunability. However, a major intrinsic disadvantage of this configuration was that the whole range of parametrically generated signal output could not be extracted. While this is not an impediment to application in RIR-PLD/ RIR-PLA, the lack of a signal output would limit some potential applications.

Chapter 5 presented the exploration of a solution to this problem. A fibre-feedback OPO was set up by employing a SMF-28e fibre in the cavity to construct a compact singly-resonant SPOPO at 1-MHz repetition rate to provide multi-microjoule signal and microjoule idler pulses that were utilisable outside the cavity.

With a 75%-transmission output coupler, pulse energies as high as 3.0 μJ (signal) and 1.1 μJ (idler) could be extracted out of the cavity. The 3-dB spectral bandwidths of the signal and idler were 7.8 nm and 50.5 nm, respectively. The maximum pulse energies generated inside the cavity were 4.0 μJ (signal) and 1.4 μJ (idler), corresponding to an overall parametric conversion efficiency of 50%. The slope efficiencies were 53.6% (signal) and 17.8% (idler) within the cavity while those external to the cavity were 36% (signal) and 13.2% (idler). The generated idler pulse energies and spectral bandwidths were adequate for RIR-PLD/ RIR-PLA of materials such as PEG and PS, whilst the multi-microjoule signal pulses could also be utilised outside the cavity. Moreover, an interesting phenomenon of intracavity supercontinuum covering components from 1510 nm through 1970 nm was generated via the feedback fibre. The output signal attained a peak power of 36.1 kW with a FWHM pulse width of 112 ps. The TBP was 113, i.e. more than 250 times of a transform-limited Gaussian pulse. When increasing the output coupling transmissivity to 90%, the 3-dB spectral bandwidth of the idler pulses was reduced to 29 nm and that of the signal after the feedback fibre was narrowed by a factor of 10 down to 35 nm. The maximum available signal and idler pulse energies external to the cavity were 2.85 μJ and 1.05 μJ with slope efficiencies of 37.8% and 14.1%, respectively. The pulse energies after the PPLN reached to 3.2 μJ (signal) and 1.3 μJ (idler), corresponding to an overall parametric conversion efficiency of 41%, at the maximum pump power. Their respective slope efficiencies were 46.8% and 19.6%. It should be noted that the performance of the fibre-feedback OPO was not fully optimised yet due to limitation on the available components at the time of the experiment. Unfortunately, further experiments could not be carried on until after the write-up of this thesis due to restricted time on the author's candidature and availability of components.

Chapter 6 devoted to the demonstration of exploiting an YDF-amplified ML-VECSEL as a high-power pump source for generating supercontinua with multi-watt average powers at multi-GHz repetition rates. The MOPA provided an average power up to 37 W at 3-GHz repetition frequency. The amplified pulses were then re-compressed to 430-fs duration by a high-throughput transmission-grating compressor with an efficiency of as high as 70%. Supercontinua were generated by launching the compressed pulses into two different PCFs with different properties. Firstly, supercontinuum with a flatness of better than ±1.5 dB over a span of 150 nm was generated via an ANDi PCF. The10-dB bandwidth was 200 nm and the average power was measured to be 3.9 W. Secondly, a 1040-nm-ZDW PCF was employed to generate supercontinuum with spectral components covering a wavelength range from 750 nm through to 1300 nm at an average power of 2.6 W, but with much higher spectral intensity variations. Spectral power density of ~20 mW/nm and ~5 mW/nm were generated in the ANDi and 1040-nm-ZDW PCFs, respectively.

Furthermore, an improved power amplifier was designed and built to boost the slope efficiency by more than two-fold to 90% and better the PER by 5 dB to a value of 18 dB. Unfortunately, further experiments on supercontinuum generation with the MOPA based on the new power amplifier could not be continued because the VECSEL seed failed to sustain mode-locking for practical durations. However, the new amplifier showed promising power-scaling capability along with good PER and M^2. In addition to generating potentially much wider supercontinuum spectra, shorter re-compressed pulses could possibly be realised and thus enhancing the coherence of the supercontinuum generation via the 1040-nm-ZDW PCF. Moreover, it is believed that this highly efficient amplifier can be applied to power-scale femtosecond GHz seed lasers, such as a waveguide oscillator, to more than 100 W of average power. Potential applications include high-power GHz self-referencing frequency comb generation.

7.2 Future Work

Although the presented systems have achieved record-breaking results, their performances could have been further improved if certain components were available at the time of the experiments. For the picosecond YDF-MOPA system, a fibre with a larger core would boost the powers and energies of the 1-μm pulses to even higher levels, and thus the extracted powers and energies of the MIR pulses via OPGs, OPAs or OPOs. Moreover, further optimisation of the fibre-feedback OPO in terms of pulse energies and spectral bandwidths would be made possible with different coupling lenses, output couplers and a feedback fibre that could delay the onset of nonlinearity. On the other hand, deliberate intracavity supercontinuum generation would also be of interest, e.g. an idler-resonant fibre-feedback OPO employing a chalcogenide fibre might be very efficient for MIR generation into the fingerprint regime (7-20 μm). Another direction to move forward would be actually implementing RIRPLD/ RIRPLA experiments and investigating the parameter space using the presented flexible MIR sources. As for the ML-VECSEL-seeded MOPA, a femtosecond GHz laser with higher stability would obviously benefit the practicality of the system, in addition to the opportunity of exploiting the redesigned highly efficient power amplifier to realise supercontinuum with wider bandwidth, higher coherence and higher spectral power density.

7.3 Final Remarks

Nonlinear frequency conversion of fibre-amplified compact semiconductor lasers offers tremendous opportunities. This thesis has shown a set of novel ultrashort-pulse systems employing such techniques for supercontinuum and tunable MIR and NIR generation. It is believed that the development of these sources offers significant impacts across various technological areas. Innovation will continue as semiconductor lasers, fibre technologies and nonlinear frequency conversion techniques continue to be developed. There is without doubt a high demand on an extensive optical toolbox from diverse industries and scientific communities that drive the on-going research and development of advanced laser technologies. Through different sectors such as electronics, photonics, manufacturing, healthcare and defence, lasers are inseparable from our daily lives as they continue to highly impact upon the academia, industries, economy and society.

Appendix:
Publications during PhD Studies

A.1 Journals

1) L. Xu, **H.-Y. Chan**, S.U. Alam, D.J. Richardson, D.P. Shepherd, "Fiber-laser-pumped, high-energy, mid-IR, picosecond optical parametric oscillator with a high-harmonic cavity", *Optics Letters* 2015, Vol.40(14) pp.3288-3291
2) L. Xu, **H.-Y. Chan**, S. Alam, D.J. Richardson, D.P. Shepherd, "High-energy, near- and mid-IR picosecond pulses generated by a fiber-MOPA-pumped optical parametric generator and amplifier", Optics Express 2015, Vol.23(10) pp.12613-12618
3) **H.-Y. Chan**, S-U. Alam, L. Xu, J. Bateman, D.J. Richardson, D.P. Shepherd, "Compact, high-pulse-energy, high-power, picosecond master oscillator power amplifier", Optics Express 2014, Vol.22 (18) pp.21938-21943
4) C. Head, **H.-Y. Chan**, J. Feehan, D. Shepherd, S.-U. Alam, A. Tropper, J. Price and K. Wilcox, "Supercontinuum Generation with Gigahertz Repetition Rate Femtosecond-Pulse Fiber-Amplified VECSELs", IEEE Photonics Technology Letters, Vol. 25 (5) pp. 464-467

A.2 Conferences

1) L. Xu, **H.-Y. Chan**, S.U. Alam, D.J. Richardson, D.P. Shepherd**, "**High-energy, high-power, near- and mid-IR picosecond pulses generated by fiber-MOPA-pumped optical parametric generator and amplifier", *CLEO/Europe-EQEC '15*, Munich, Germany, 21-25 Jun 2015 (CD-P.17)
2) L. Xu, **H.-Y. Chan**, S.U. Alam, D.J. Richardson, D.P. Shepherd, "High-energy, mid-IR pulses generated by a compact, high-harmonic-cavity,

optical parametric oscillator", International Conference on Optical Instrument and Technology, Beijing, China, 17-19 May 2015 (OIT400-21)

3) **H.-Y. Chan,** L. Xu, J. Bateman, S.U. Alam, D.J. Richardson, D.P. Shepherd, "16-μJ pulse energy, picosecond, narrow-linewidth master oscillator power amplifier using direct amplification", *CLEO/ QELS 2014*, San Jose, California, USA, 8-13 Jun 2014
4) P. Teh, S.-U. Alam, **H.-Y. Chan**, D. Shepherd, and D. Richardson, "Generation of transform-limited picosecond pulses at 1.0 micron from a gain switched semiconductor laser diode", IEEE 4th International Conference on Photonics- ICP 2013, Melaka, Malaysia, 28-30 Oct 2013
5) P. Teh, **H.-Y. Chan**, R. Lewis, D. Shepherd, S.-U. Alam and D. Richardson, "200W Gain-Switched-Diode-Seeded, Single-Polarisation, Narrow-Linewidth, All-Fiber, Picosecond MOPA", CLEO/ QELS 2013, San Jose, California, USA, 9-14 June 2013 (CW3M.2)
6) C. Head, **H.-Y. Chan**, J. Feehan, D. Shepherd, S.-U. Alam, A. Tropper, J. Price and K. Wilcox, "Supercontinuum Generation with Femtosecond-Pulse Fibre-Amplified VECSELs", SPIE Photonics West: LASE 2013, San Francisco, California, USA, 2-7 February 2013

A.3 Conference Proceedings

1) C. Head, **H.-Y. Chan**, J. Feehan, D. Shepherd, S.-U. Alam, A. Tropper, J. Price and K. Wilcox, "Supercontinuum Generation with Femtosecond-Pulse Fibre-Amplified VECSELs", *Proc. SPIE* 8606, Vertical External Cavity Surface Emitting Lasers (VECSELs) III, 860608 (February 18, 2013)

List of References

1. T. H. Maiman, Nature **187**, 493 (1960).

2. F. Adler, P. Masłowski, A. Foltynowicz, K. C. Cossel, T. C. Briles, I. Hartl, and J. Ye, Opt. Express **18**, 21861 (2010).

3. S. Woutersen, U. Emmerichs, and H. J. Bakker, Science **278**, 658 (1997).

4. B. Pejcic, M. Myers, and A. Ross, Sensors (Basel). **9**, 6232 (2009).

5. V. Bellon-Maurel and A. McBratney, Soil Biol. Biochem. **43**, 1398 (2011).

6. D. M. Bubb, R. a. McGill, J. S. Horwitz, J. M. Fitz-Gerald, E. J. Houser, R. M. Stroud, P. W. Wu, B. R. Ringeisen, A. Piqué, and D. B. Chrisey, J. Appl. Phys. **89**, 5739 (2001).

7. M. R. Papantonakis and R. F. Haglund Jr., Appl. Phys. A **79**, 1687 (2004).

8. B. Toftmann, M. R. Papantonakis, R. C. Y. Auyeung, W. Kim, S. M. O'Malley, D. M. Bubb, J. S. Horwitz, J. Schou, P. M. Johansen, and R. F. Haglund, Thin Solid Films **453-454**, 177 (2004).

9. P. Agostini and L. F. DiMauro, Contemp. Phys. **49**, 179 (2008).

10. G. Edwards, R. Logan, M. Copeland, L. Reinisch, J. Davidson, B. Johnson, R. Maciunas, M. Mendenhall, R. Ossoff, and J. Tribble, Nature **371**, 416 (1994).

11. R. Furstenberg, C. A. Kendziora, J. Stepnowski, S. V. Stepnowski, M. Rake, M. R. Papantonakis, V. Nguyen, G. K. Hubler, and R. A. McGill, Appl. Phys. Lett. **93**, 224103 (2008).

12. R. Pate, K. R. Lantz, and A. D. Stiff-Roberts, IEEE J. Sel. Top. Quantum Electron. **14**, 1022 (2008).

13. V. Z. Kolev, M. W. Duering, B. Luther-Davies, and A. V Rode, Opt. Express **14**, 12302 (2006).

14. R. Eason, editor , *Pulsed Laser Deposition of Thin Films: Applications-Led Growth of Functional Materials* (John Wiley & Sons, Hoboken, New Jersey, 2007).

15. E. Slobodchikov and P. F. Moulton, in *CLEO/ QELS* (Baltimore, MD, USA, 2011), p. PDPA10.

16. L. R. Botha, C. Bollig, and M. J. D. Esser, Opt. Express **17**, 20615 (2009).

17. J. W. Evans, P. A. Berry, and K. L. Schepler, IEEE J. Quantum Electron. **50**, 204 (2014).

18. S. A. McDaniel, P. A. Berry, and K. L. Schepler, Proc. SPIE **8599**, 85990D (2013).

19. W. Koen, C. Jacobs, C. Bollig, H. J. Strauss, M. J. D. Esser, and L. R. Botha, Opt. Lett. **39**, 3563 (2014).

20. V. Fedorov, S. Mirov, A. Gallian, D. Badikov, M. Frolov, Y. Korostelin, V. Kozlovsky, and A. Landman, Alexander Podmar'kov, Yuri; Akimov, Vadim; Voronov, IEEE J. Quantum Electron. Electron. **42**, 907 (2006).

21. D. M. Bubb, M. R. Papantonakis, B. Toftmann, J. S. Horwitz, R. a. McGill, D. B. Chrisey, and R. F. Haglund, J. Appl. Phys. **91**, 9809 (2002).

22. D. M. Bubb, B. Toftmann, R. F. Haglund, J. S. Horwitz, M. R. Papantonakis, R. A. Mcgill, P. W. Wu, and D. B. Chrisey, Appl. Phys. A **125**, 123 (2002).

23. D. M. Bubb, S. L. Johnson, R. Belmont, K. E. Schriver, R. F. Haglund Jr., C. Antonacci, and L.-S. Yeung, Appl. Phys. A **83**, 147 (2006).

24. S. L. Johnson, K. E. Schriver, R. F. Haglund, and D. M. Bubb, J. Appl. Phys. **105**, 024901 (2009).

25. S. L. Johnson, D. M. Bubb, and R. F. Haglund, Appl. Phys. A **96**, 627 (2009).

26. B. Köhler, U. Bäder, A. Nebel, J. P. Meyn, and R. Wallenstein, Appl. Phys. B Lasers Opt. **75**, 31 (2002).

27. F. Kienle, P. S. Teh, S.-U. Alam, C. B. E. Gawith, D. C. Hanna, D. J. Richardson, and D. P. Shepherd, Opt. Lett. **35**, 3580 (2010).

28. T. P. Lamour and D. T. Reid, Opt. Express **19**, 17557 (2011).

29. T. P. Lamour, L. Kornaszewski, J. H. Sun, and D. T. Reid, Opt. Express **17**, 14229 (2009).

30. V. Gerginov, C. E. Tanner, S. A. Diddams, A. Bartels, and L. Hollberg, Opt. Lett. **30**, 1734 (2005).

31. M. Y. Sfeir, F. Wang, L. Huang, C.-C. Chuang, J. Hone, S. P. O'brien, T. F. Heinz, and L. E. Brus, Science **306**, 1540 (2004).

32. D. M. Grant, D. S. Elson, D. Schimpf, C. Dunsby, J. Requejo-Isidro, E. Auksorius, I. Munro, M. A. A. Neil, P. M. W. French, E. Nye, G. Stamp, and P. Courtney, Opt. Lett. **30**, 3353 (2005).

33. I. Hartl, X. D. Li, C. Chudoba, R. K. Ghanta, T. H. Ko, J. G. Fujimoto, J. K. Ranka, and R. S. Windeler, Opt. Lett. **26**, 608 (2001).

34. Z. Yusoff, P. Petropoulos, K. Furusawa, T. M. Monro, and D. J. Richardson, IEEE Photonics Technol. Lett. **15**, 1689 (2003).

35. P. C. Pastor, G. Giusfredi, P. De Natale, G. Hagel, C. De Mauro, and M. Inguscio, Phys. Rev. Lett. **92**, 023001 (2004).

36. S. Stark, H. Hundertmark, P. S. J. Russell, R. Probst, T. Wilken, T. W. Hänsch, T. Udem, T. Steinmetz, and R. Holzwarth, Opt. Express **19**, 15690 (2011).

37. R. R. Alfano and S. L. Shapiro, Phys. Rev. Lett. **24**, 584 (1970).

38. C. S. Dudley J.M., Genty G., Rev. Mod. Phys. **78**, 1135 (2006).

39. K. K. Chow, Y. Takushima, C. Lin, C. Shu, and A. Bjarklev, Electron. Lett. **42**, 989 (2006).

40. A. M. Heidt, J. Opt. Soc. Am. B **27**, 550 (2010).

41. S. Zhang, F. Lu, X. Dong, P. Shum, X. Yang, X. Zhou, Y. Gong, and C. Lu, Opt. Lett. **30**, 2852 (2005).

42. A. A. Lagatsky, A. Choudhary, P. Kannan, D. P. Shepherd, W. Sibbett, and C. T. A. Brown, Opt. Express **21**, 19608 (2013).

43. A. Bartels, D. Heinecke, and S. Diddams, Science **326**, 681 (2009).

44. P. W. Roth, A. J. Maclean, D. Burns, and A. J. Kemp, Opt. Lett. **36**, 304 (2011).

45. S. Sawai, A. Hosaka, H. Kawauchi, K. Hirosawa, and F. Kannari, Appl. Phys. Express **7**, 022702 (2014).

46. A. C. Tropper, A. H. Quarterman, and K. G. Wilcox, *Ultrafast Vertical-External-Cavity Surface-Emitting Semiconductor Lasers*, 1st ed. (Elsevier Inc., 2012).

47. O. D. Sieber, V. J. Wittwer, M. Mangold, M. Hoffmann, M. Golling, T. Südmeyer, and U. Keller, Opt. Express **19**, 23538 (2011).

48. K. G. Wilcox, A. H. Quarterman, H. E. Beere, D. A. Ritchie, and A. C. Tropper, Opt. Express **19**, 23453 (2011).

49. A. H. Quarterman, K. G. Wilcox, V. Apostolopoulos, Z. Mihoubi, S. P. Elsmere, I. Farrer, D. A. Ritchie, and A. Tropper, Nat. Photonics **3**, 729 (2009).

50. M. Scheller, T.-L. Wang, B. Kunert, W. Stolz, S. W. Koch, and J. V. Moloney, Electron. Lett. **48**, 588 (2012).

51. P. Dupriez, C. Finot, A. Malinowski, J. K. Sahu, J. Nilsson, D. J. Richardson, K. G. Wilcox, H. D. Foreman, and A. C. Tropper, Opt. Express **14**, 9611 (2006).

52. I. H. Ito H., Yokoyama H., Murata S., Electron. Lett. **15**, 738 (1979).

53. K. Y. Lau, Appl. Phys. Lett. **52**, 257 (1988).

54. L. P. Barry, B. C. Thomsen, J. M. Dudley, and J. D. Harvey, IEEE Photonics Technol. Lett. **10**, 935 (1998).

55. B. C. Thomsen, Y. Jeong, C. Codemard, A. F. Roelens, P. Dupriez, J. K. Sahu, J. Nilsson, and D. J. Richardson, in *CLEO/ QELS* (San Francisco, CA, USA, 2004), p. CMMA.

56. P. Dupriez, A. Piper, A. Malinowski, J. K. Sahu, M. Ibsen, B. C. Thomsen, Y. Jeong, L. M. B. Hickey, M. N. Zervas, J. Nilsson, and D. J. Richardson, IEEE Photonics Technol. Lett. **18**, 1013 (2006).

57. P. S. Teh, S. Alam, R. J. Lewis, and D. J. Richardson, Laser Phys. Lett. **11**, 85103 (2014).

58. K. T. Vu, A. Malinowski, M. a. F. Roelens, M. Ibsen, and D. J. Richardson, 2007 Quantum Electron. Laser Sci. Conf. 1 (2007).

59. P. S. Teh, S. Alam, D. P. Shepherd, and D. J. Richardson, Opt. Express **22**, 13366 (2014).

60. A. C. Tropper and S. Hoogland, Prog. Quantum Electron. **30**, 1 (2006).

61. K. G. Wilcox, Z. Mihoubi, G. J. Daniell, S. Elsmere, A. Quarterman, I. Farrer, D. A. Ritchie, and A. Tropper, Opt. Lett. **33**, 2797 (2008).

62. G. P. Agrawal, *Nonlinear Fiber Optics*, 4th Ed. (Academic Press, 2007).

63. ISO Standard 11146, *Lasers and Laser-Related Equipment – Test Methods for Laser Beam Widths, Divergence Angles and Beam Propagation Ratios* (2005).

64. E. Snitzer, Phys. Rev. Lett. **7**, 444 (1961).

65. C. J. Koester and E. Snitzer, Appl. Opt. **3**, 1182 (1964).

66. R. Mears, L. Reekie, I. Jauncey, and D. Payne, Electron. Lett. **23**, 1026 (1987).

67. Y.-C. Jeong, A. J. Boyland, J. K. Sahu, S.-H. Chung, J. Nilsson, and D. N. Payne, J. Opt. Soc. Korea **13**, 416 (2009).

68. A. Klenke, S. Hädrich, T. Eidam, J. Rothhardt, M. Kienel, S. Demmler, T. Gottschall, J. Limpert, and A. Tünnermann, Opt. Lett. **39**, 6875 (2014).

69. R. Paschotta, J. Nilsson, A. C. Tropper, and D. C. Hanna, IEEE J. Quantum Electron. **33**, 1049 (1997).

70. D. J. Richardson, J. Nilsson, and W. A. Clarkson, J. Opt. Soc. Am. B **27**, B63 (2010).

71. J. D. Kafka, US Patent 4,829,529 (1989).

72. A. B. Grudinin, P. W. Turner, M. Ibsen, M. K. Durkin, J. Nilsson, D. N. Payne, and M. N. Zervas, U.S. patent 6,826,335 (2004).

73. E. Stiles, in *Proc. 5th Int. Work. Fiber Lasers* (Dresden, Germany, 2009).

74. J. Limpert, H. Zellmer, A. Tünnermann, T. Pertsch, and L. F, in *Adv. Solid-State Lasers* (Quebec City, Canada, 2002), p. MB20.

75. J. M. Sousa and O. G. Okhotnikov, Appl. Phys. Lett. **74**, 1528 (1999).

76. D. Marcuse, J. Opt. Soc. Am. **66**, 216 (1976).

77. J. A. Alvarez-Chavez, A. B. Grudinin, J. Nilsson, P. W. Turner, and W. A. Charkson, in *CLEO/ QELS* (Baltimore, MD, USA, 1999), pp. 247–248.

78. D. Strickland and G. Mourou, Opt. Commun. **56**, 219 (1985).

79. F. Röser, T. Eidam, J. Rothhardt, O. Schmidt, D. N. Schimpf, J. Limpert, and A. Tünnermann, Opt. Lett. **32**, 3495 (2007).

80. V. I. Kruglov, A. C. Peacock, J. D. Harvey, and J. M. Dudley, J. Opt. Soc. Am. B **19**, 461 (2002).

81. A. Malinowski, A. Piper, J. H. V Price, K. Furusawa, Y. Jeong, J. Nilsson, and D. J. Richardson, Opt. Lett. **29**, 2073 (2004).

82. R. W. Boyd, *Nonlinear Optics*, 3rd Ed. (Academic Press, 2008).

83. M. M. Fejer, G. A. Magel, D. H. Jundt, and R. L. Byer, IEEE J. Quantum Electron. **28**, 2631 (1992).

84. R. L. Byer and R. L. Herbst, in *Nonlinear Infrared Gener.*, edited by Y. R. Shen (Springer, Berlin, 1977), pp. 81–137.

85. S. Guha, Appl. Phys. B Lasers Opt. **66**, 663 (1998).

86. M. J. McCarthy and D. C. Hanna, J. Opt. Soc. Am. B **10**, 2180 (1993).

87. D. C. Hanna, M. V O’Connor, M. A. Watson, and D. P. Shepherd, J. Phys. D. Appl. Phys. **34**, 2440 (2001).

88. F. Jermann, M. Simon, and E. Krätzig, J. Opt. Soc. Am. B **12**, 2066 (1995).

89. Y. Furukawa, K. Kitamura, A. Alexandrovski, R. K. Route, M. M. Fejer, and

G. Foulon, Appl. Phys. Lett. **78**, 1970 (2001).

90. H. Linnenbank and S. Linden, Opt. Express **22**, 18072 (2014).

91. T. Andres, P. Haag, S. Zelt, J.-P. Meyn, A. Borsutzky, R. Beigang, and R. Wallenstein, Appl. Phys. B Lasers Opt. **76**, 241 (2003).

92. J. Rothhardt, S. Hädrich, D. N. Schimpf, J. Limpert, and A. Tünnermann, Opt. Express **15**, 16729 (2007).

93. S. C. Kumar and E.-Z. Majid, Opt. Express **19**, 26660 (2011).

94. K. Kowalewski, J. Zembek, V. Envid, and D. C. Brown, Opt. Lett. **37**, 4633 (2012).

95. A. Ancona, S. Döring, C. Jauregui, F. Röser, J. Limpert, S. Nolte, and A. Tünnermann, Opt. Lett. **34**, 3304 (2009).

96. M. S. Trtica, B. M. Gakovic, D. Maravic, D. Batani, T. Desai, and R. Redaelli, Appl. Surf. Sci. **253**, 9315 (2007).

97. L. Rapp, A. K. Diallo, A. P. Alloncle, C. Videlot-Ackermann, F. Fages, and P. Delaporte, Appl. Phys. Lett. **95**, 10 (2009).

98. C. Fornaroli, J. Holtkamp, and A. Gillner, Phys. Procedia **41**, 603 (2013).

99. I. B. Sohn, Y. C. Noh, Y. S. Kim, D. K. Ko, J. Lee, and Y. J. Choi, J. Opt. Soc. Korea **12**, 38 (2008).

100. B. Gaković, M. Trtica, D. Batani, T. Desai, P. Panjan, and D. Vasiljević-Radović, J. Opt. A Pure Appl. Opt. **9**, S76 (2007).

101. J. M. Lackner, W. Waldhauser, R. Ebner, a. Fian, G. Jakopic, G. Leising, and T. Schöberl, Surf. Coatings Technol. **177-178**, 360 (2004).

102. M. Pervolaraki, P. Komninou, J. Kioseoglou, a. Othonos, and J. Giapintzakis, Appl. Surf. Sci. **278**, 101 (2013).

103. M. Kraus, M. A. Ahmed, A. Michalowski, A. Voss, R. Weber, and T. Graf, Opt. Express **18**, 22305 (2010).

104. Z. Zhao, B. M. Dunham, and F. W. Wise, J. Opt. Soc. Am. B **31**, 33 (2013).

105. P. S. Teh, R. J. Lewis, S. Alam, and D. J. Richardson, Opt. Express **21**, 25883 (2013).

106. P. Elahi, S. Yılmaz, Y. B. Eldeniz, and F. Ö. Ilday, Opt. Lett. **39**, 236 (2014).

107. H.-Y. Chan, S. Alam, L. Xu, J. Bateman, D. J. Richardson, and D. P. Shepherd, Opt. Express **22**, 21938 (2014).

108. F. Kienle, K. K. Chen, S.-U. Alam, C. B. E. Gawith, J. I. Mackenzie, D. C. Hanna, D. J. Richardson, and D. P. Shepherd, Opt. Express **18**, 7602 (2010).

109. G. Marchev, F. Pirzio, R. Piccoli, A. Agnesi, G. Reali, P. G. Schunemann, K. T. Zawilski, A. Tyazhev, and V. Petrov, Opt. Lett. **38**, 3344 (2013).

110. R. Piccoli, F. Pirzio, A. Agnesi, V. Badikov, B. Dmitrii, G. Marchev, V. Panyutin, and V. Petrov, Opt. Lett. **39**, 4895 (2014).

111. K. Balskus, S. M. Leitch, Z. Zhang, R. A. Mccracken, and D. T. Reid, **23**, 555 (2015).

112. O. Kimmelma, S. C. Kumar, and A. Esteban-Martin, **38**, 4550 (2013).

113. L. Xu, H.-Y. Chan, S. Alam, D. J. Richardson, and D. P. Shepherd, Opt. Express **23**, 12613 (2015).

114. L. Xu, H.-Y. Chan, S. Alam, D. J. Richardson, and D. P. Shepherd, Opt. Lett. **40**, 3288 (2015).

115. A. E. Siegman, *Lasers* (University Science Books, Palo Alto, 1986).

116. O. Gayer, Z. Sacks, E. Galun, and A. Arie, Appl. Phys. B **91**, 343 (2008).

117. A. V Okishev and J. D. Zuegel, Opt. Express **14**, 12169 (2006).

118. O. Chalus, P. G. Schunemann, K. T. Zawilski, J. Biegert, and M. Ebrahim-Zadeh, Opt. Lett. **35**, 4142 (2010).

119. J. Prawiharjo, H. S. S. Hung, D. C. Hanna, and D. P. Shepherd, J. Opt. Soc. Am. B **24**, 895 (2007).

120. B. Bourliaguet, V. Couderc, A. Barthélémy, G. W. Ross, P. G. Smith, D. C. Hanna, and C. De Angelis, Opt. Lett. **24**, 1410 (1999).

121. P. Di Trapani, A. Bramati, S. Minardi, W. Chinaglia, C. Conti, S. Trillo, J. Kilius, and G. Valiulis, Phys. Rev. Lett. **87**, 18 (2001).

122. S. French, M. Ebrahimzadeh, and A. Miller, Opt. Lett. **21**, 131 (1996).

123. E. S. Wachman, D. C. Edelstein, and C. L. Tang, Opt. Lett. **15**, 136 (1990).

124. C. Laporte, J.-B. Dherbecourt, J.-M. Melkonian, M. Raybaut, C. Drag, and A. Godard, J. Opt. Soc. Am. B **31**, 1026 (2014).

125. C. R. Head, H.-Y. Chan, J. S. Feehan, D. P. Shepherd, S. Alam, A. C. Tropper, J. H. V Price, and K. G. Wilcox, IEEE Photonics Technol. Lett. **25**, 464 (2013).

126. R. L. Fork, C. H. Cruz, P. C. Becker, and C. V Shank, Opt. Lett. **12**, 483 (1987).

127. Z. Zhao, B. M. Dunham, I. Bazarov, and F. W. Wise, Opt. Express **20**, 4850 (2012).

128. Y. Jeong, J. Sahu, D. Payne, and J. Nilsson, Opt. Express **12**, 6088 (2004).

129. K. K. Chen, J. H. V Price, S.-U. Alam, J. R. Hayes, D. Lin, A. Malinowski, and D. J. Richardson, Opt. Express **18**, 14385 (2010).